

Stellingen

behorende bij het proefschrift

On Gamma Ray Shielding and Neutron Streaming Through Ducts

1. Het argument dat Monte Carlo codes bruikbaar zijn voor ingewikkelde drie-dimensionale geometrieën, wordt teniet gedaan door het feit dat de benodigde rekentijd excessief toeneemt met de complexiteit van de gemodelleerde geometrie.
2. De benaming "importantie" in Monte Carlo theorie voor de verwachte detectorbijdrage van een deeltje dat een botsing ingaat of een botsing uitkomt, wekt verwarring en kan derhalve beter worden vermeden.
3. Bij het gebruik van Monte Carlo methoden voor afschermingsberekeningen dient de uitkomst niet alleen vergezeld te gaan van de standaarddeviatie, maar tevens van de mededeling dat de vermelde standaarddeviatie alleen ten gevolge van het Monte Carlo proces is.
4. De nauwkeurigheid van een reactorfysisch codepakket volgt uit de eindresultaten van zogenoemde "benchmark"-berekeningen. Om de kundigheid van de gebruikers van dat codepakket te beoordelen kan men beter de eerste resultaten van benchmarkberekeningen vergelijken.
5. De publieke acceptatie van kernenergie voor elektriciteitsproductie is gebaat bij een strikte scheiding van militaire en civiele kerninstallaties.

6. Met transmutatie van actiniden kan de benodigde opbergtijd van kernsplitsingsafval zodanig worden verkort dat ethische argumenten tegen de produktie van kernsplitsingsafval kunnen worden weerlegd.
Nigel Holloway, ATOM 404, June 1990
7. Wetenschappelijke ontdekkingen kunnen worden bevorderd door onderzoeksgelden meer individueel gericht te verdelen.
8. Marginale landbouwgebieden rond de Oosterschelde bieden in het kader van het Natuurbeleidsplan en plan Tureluur, goede grond voor natuurontwikkeling.
9. Omdat bij een correct genomen strafschoep de doelverdediger onmogelijk de bal uit het doel kan houden, zou men bij gelijkspel van een voetbalfinalewedstrijd beter de ploeg kunnen laten winnen die het minst aantal overtredingen heeft begaan.
10. "Een goed begin is het halve werk" geldt ook voor een promotie-onderzoek. Uit de hoeveelheid correspondentie die een promovendus ontvangt met titulatuur "Dr." en "Prof. Dr." kan worden afgeleid dat ook geldt: "Een goed begin is een halve titel".
11. De meest gebruikte kopieermachines zijn het minst bruikbaar.

J.L. Kloosterman, 23 juni 1992

547723
3172794
TR diss 2080

2076
**TR diss
2080**

On Gamma Ray Shielding and Neutron Streaming Through Ducts

J.L. Kloosterman



Interfacultair Reactor Instituut van de Technische Universiteit Delft

Cover photograph: a concrete shielding block moving into the irradiation tunnel of the research reactor of the Institute of Nuclear Technics of the Technical University of Budapest.

CIP-GEGEVENS KONINKLIJKE BIBLIOTHEEK, DEN HAAG

Kloosterman, Jan Leendert

On Gamma Ray Shielding and Neutron Streaming Through Ducts /
Jan Leendert Kloosterman. - Delft: Interfacultair

Reactor Instituut, Delft University of Technology. - Ill.

Thesis Technische Universiteit Delft. - With ref. - With
summary in Dutch.

ISBN 90-73861-07-1

NUGI 812

Subject headings: gamma ray shielding / neutron streaming.

Copyright ©1992 by J.L. Kloosterman.

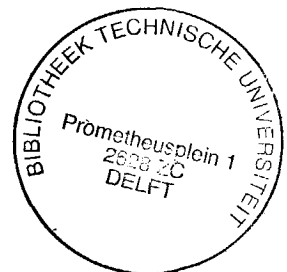
On Gamma Ray Shielding and Neutron Streaming Through Ducts

Proefschrift

ter verkrijging van de graad van doctor aan de Technische Universiteit Delft,
op gezag van de Rector Magnificus, prof. drs. P.A. Schenck, in het openbaar
te verdedigen ten overstaan van een commissie aangewezen door het College
van Dekanen op 23 juni 1992 te 10.00 uur door

Jan Leendert Kloosterman

geboren te Kapelle
ingenieur in de technische natuurkunde



Dit proefschrift is goedgekeurd door de promotor:
prof. dr. ir. H. van Dam

Toegevoegd promotor:
dr. ir. J.E. Hoogenboom

The research described in this thesis has been performed at the reactor physics department of the Interfaculty Reactor Institute of the Delft University of Technology, Mekelweg 15, 2629 JB Delft, the Netherlands.

Aan mijn ouders
Aan Helmieke

Contents

Chapter 1	
Introduction	1
1.1 History	1
1.2 Outline	3
1.3 The Transport Equation	3
Chapter 2	
MARMER, a Flexible Point-Kernel Shielding Code	15
2.1 Introduction	15
2.2 Calculational Method	17
2.3 Options in MARMER	21
2.3.1 Geometry Description	21
2.3.2 Energy Group Structure	23
2.3.3 Spectrum Definition	24
2.3.4 Spatial Source Description	25
2.3.5 Angular Source Description	26
2.3.6 Material Composition	27
2.3.7 Detector Response Functions and Buildup Factors	27
2.4 MARMER Data Libraries	30
Chapter 3	
Gamma Ray Benchmark Calculations on the TN12 Spent Fuel Shipping Cask by the Point-Kernel Shielding Code MARMER	33
3.1 Introduction	33
3.2 Benchmark Description	34
3.3 Calculations	35
3.4 Results	39
3.5 Conclusions	43
Chapter 4	
Gamma Ray Buildup Factor Calculations for Iron by the Discrete Ordinates Code XSDRNPM-S	45
4.1 Introduction	45

4.2 Cross Section Library Preparation	47
4.3 Buildup Factor Calculations	49
4.4 Calculations	50
4.5 Discussion	55
4.6 Conclusions	59
Chapter 5	
Simple Streaming Methods	61
5.1 Introduction	61
5.2 Line-of-Sight Component	62
5.3 Albedo Component and Bent Ducts	68
5.4 IRIDUCT	73
Chapter 6	
Neutron Flux Measurements in Straight and Bent Ducts	77
6.1 Introduction	77
6.2 Thermoluminescence Measurements	78
6.3 Multiple Foil Activation Measurements	85
6.4 Measurement Procedures	92
Chapter 7	
Calculations and Comparison with Measurements	93
7.1 Calculations	93
7.2 Comparison with Measurements	106
7.3 Conclusions	118
Chapter 8	
Importance Iteration in Monte Carlo Calculations	121
8.1 Introduction	121
8.2 Calculation of Point Values	122
8.3 Calculation of Importance Functions	127
8.4 Example	129
8.5 Conclusions	135
Bibliography	137

Appendix A	
Calculational Method of XSDRNPM-S	147
Appendix B	
Correlated Sampling	149
Summary	153
Samenvatting	155
Acknowledgements	157
Curriculum vitae	159

Chapter 1

Introduction

1.1 History

The increasing demand of electricity in the mid-eighties, the need for reliable electricity production plants based on different sources of energy, and the wish to decrease oil imports, lead to the idea that nuclear energy should play an important role in the Netherlands. To increase the percentage of nuclear generated electricity from 5 to 30%, approximately, several large nuclear plants should be built, which would lead to an increasing appeal to engineering and consultancy companies to design and validate parts of nuclear plants. In the field of shielding, however, it was felt that the available software should be modernized in order to meet present-day requirements. Although the optimism about new nuclear plants in the Netherlands shrank rapidly after the Chernobyl accident in 1986, it was still felt that shielding software should be modernized, because it was expected that interim storage and transportation of spent fuel assemblies and interim and final storage of highly radioactive nuclear waste, would require sophisticated shielding studies.

The history of reactor shielding can be divided into several parts [Bol87]. After the second world war, at the introduction of the first commercial nuclear plants, a large bunch of simplified, semi-empirical and empirical methods for shielding calculations was developed. By assuring that simplifications lead to overestimations of the calculated result, and by applying a safety factor of 2 or higher, conservative results were obtained. It is still rather surprising that point-kernel and removal-diffusion methods of that period gave such good results, when it is recognized that neutron fluxes are generally attenuated by 13 orders of magnitude from the reactor core up to the outer side of the biological shield (about 3 meters of concrete).

However, shielding calculational methodology in general has evolved in close correspondence with computer science. As computers became faster and cheaper, a still continuing process, shielding calculations became more

rigorous. Although the Boltzmann transport equation is now already solved rigorously by discrete ordinates and Monte Carlo codes, which make use of extensive data libraries, there is still a tendency to more geometrical possibilities, higher accuracy in cross section representation, higher accuracy in calculational methods, and a more accurate representation of the source, thus leading to more reliable and accurate results.

This leads us to the stage where we are now. Although very accurate methods exist and are being used, comparison of results of calculations carried out by different shielding groups at the one hand, and measurements at the other hand, lead to the surprising result that disagreements between mutual calculated results and between calculations and measurements go beyond the estimated errors of the calculations and measurements. Misuse of rigorous transport codes, inadequate definition of the shielding problem, cross section data inaccuracies, input errors, etc. lead to these discrepancies, which are very difficult to quantify and often severely underestimated. The tendency present-day is to improve the quality of the calculations by studying the sensitivity of the calculated results to the input parameters, cross section data and geometry of the problem. Furthermore, recognizing energy and spatial channels in the shield, and treating them differently from the bulk shielding calculations, also improves the quality of the calculations considerably.

Despite all powerful computers today, the older methods are still attractive to get an insight into the shielding problem under consideration and to get quick estimates of gamma dose rates and neutron fluxes in the shield. Using less sophisticated shielding codes is still common use today, although rigorous transport codes may be used to check some of the results. Modernizing old shielding codes may be needed because these codes are often very restrictive with respect to calculational method, data libraries and input data, which leads to relatively long input data preparation times and to restrictions on the type of problems which can be solved.

This thesis describes two ways to modernize shielding methodology. First the old gamma ray point-kernel shielding code MERCURE-IV [Dev74] is modernized with respect to geometry description, data libraries, input data and flexibility, which lead to the shielding code MARMER [Klo90a, Klo90c]. Secondly, attention has been paid to the streaming problem, which lead to experiments and calculations with two-dimensional discrete ordinates and three-dimensional Monte Carlo transport codes, thus showing how such streaming

problems can be approached and how shielding codes perform in these cases.

1.2 Outline

Section 1.3 describes the Boltzmann transport equation, which forms the basis of transport codes. A formal link between the transport equation and the point-kernel model is given, from which it is clear which assumptions lead to this simple approach. The Boltzmann transport equation also acts as a starting point for the derivation of the integral transport equation, which is solved in Monte Carlo codes, to show the similarity and differences between the point-kernel and Monte Carlo methods.

Chapter 2 describes the calculational method, input options and data libraries of the point-kernel shielding code MARMER. A part of the validation of this code is described in Chapter 3, where calculated dose rates around a TN12 spent fuel shipping cask are compared with measurements described in literature. Buildup factor calculations are carried out and described in Chapter 4. Especially the difficulties when using discrete ordinates transport codes for high energy deep penetration gamma ray shielding problems will be set out.

A short outline of the streaming problem will be given in Chapter 5, together with some simple methods from literature to tackle such problems. The simple streaming program IRIDUCT, based on such a method will be described shortly. Chapter 6 describes neutron flux measurements in a straight cylindrical duct and in ducts with a bend of 30, 60 and 90 degrees. These experiments are carried out in cooperation with the reactor physics group of the Institute of Nuclear Technics of the Technical University of Budapest. Chapter 7 describes discrete ordinates and Monte Carlo calculations from which the results are compared with the measurements described in Chapter 6. A method to improve Monte Carlo calculations is described in Chapter 8.

1.3 The Transport Equation

Transport of uncharged particles (e.g. gamma rays and neutrons), can be described by the Boltzmann transport equation. As time dependence can often be neglected in shielding problems, the transport equation for a non-

multiplying medium reads [Dud76]:

$$\begin{aligned} \Omega \cdot \nabla \phi(\mathbf{r}, E, \Omega) + \Sigma_t(\mathbf{r}, E)\phi(\mathbf{r}, E, \Omega) = S(\mathbf{r}, E, \Omega) + \\ + \int_{4\pi} \int_0^\infty \Sigma_s(\mathbf{r}, E' \rightarrow E, \Omega' \rightarrow \Omega)\phi(\mathbf{r}, E', \Omega')dE'd\Omega' \end{aligned} \quad (1.1)$$

where \mathbf{r} is the spatial coordinate, E is the energy, Ω is the direction, $\phi(\mathbf{r}, E, \Omega)$ is the flux per unit energy and per unit solid angle, $\Sigma_t(\mathbf{r}, E)$ is the total cross section, $\Sigma_s(\mathbf{r}, E' \rightarrow E, \Omega' \rightarrow \Omega)dE'd\Omega'$ is the scattering cross section for scattering from energy E' to dE around E and from direction Ω' to solid angle $d\Omega$ around Ω , and $S(\mathbf{r}, E, \Omega)$ is the fixed source density per unit energy and per unit solid angle.

This integro-differential transport equation can be solved numerically in several ways. Treating the energy dependence in groups, discretizing the spatial and angular coordinates, approximating derivatives by finite differences and integrals by numerical quadratures, one arrives at a discrete ordinates method. The solution method of the one-dimensional discrete ordinates code XSDRNPM-S [Gre83] in spherical geometry is given in Appendix A. Furthermore, the integro-differential transport equation serves as a starting point for the derivation of the point-kernel shielding model, which is used in simple gamma ray shielding codes, and for the derivation of the integral form of the transport equation, which is solved in Monte Carlo codes.

The point-kernel model can be derived from Eq. (1.1) by assuming that the in-scattering source term is zero. Eq. (1.1) then simplifies to:

$$\Omega \cdot \nabla \phi(\mathbf{r}', E, \Omega) + \Sigma_t(\mathbf{r}', E)\phi(\mathbf{r}', E, \Omega) = S(\mathbf{r}', E, \Omega) \quad (1.2)$$

Here, an arbitrary coordinate \mathbf{r}' is introduced which is related to \mathbf{r} via $\mathbf{r}' = \mathbf{r} - R\Omega$, where R is the distance between \mathbf{r} and \mathbf{r}' . The first term on the left hand side (LHS) of Eq. (1.2) is equal to $-\frac{\partial \phi(\mathbf{r}', E, \Omega)}{\partial R}$. An integrating factor $\exp\left(-\int_0^R \Sigma_t(\mathbf{r} - s\Omega, E)ds\right)$ is used to write Eq. (1.2) as:

$$\frac{\partial \left(\phi(\mathbf{r}', E, \Omega) \exp\left(-\int_0^R \Sigma_t(\mathbf{r} - s\Omega, E)ds\right) \right)}{\partial R} =$$

$$= S(\mathbf{r}', E, \Omega) \exp \left(- \int_0^R \Sigma_t(\mathbf{r} - s\Omega, E) ds \right) \quad (1.3)$$

Integrating both sides for R from 0 to ∞ , applying the boundary condition $\phi(\infty, E, \Omega) \exp \left(- \int_0^{\infty} \Sigma_t(\mathbf{r} - s\Omega, E) ds \right) = 0$, and integrating both sides over Ω gives:

$$\phi(\mathbf{r}, E) = \int_{4\pi} \int_0^{\infty} S(\mathbf{r}', E, \Omega) \exp \left(- \int_0^R \Sigma_t(\mathbf{r} - s\Omega) ds \right) dR d\Omega \quad (1.4)$$

Using that an elementary volume in spherical coordinates can be written as $R^2 dR d\Omega$ and introducing an isotropic source density, Eq. (1.4) becomes:

$$\phi(\mathbf{r}, E) = \int_{all V} \frac{S(\mathbf{r}', E) \exp \left(- \int_0^R \Sigma_t(\mathbf{r} - s\Omega, E) ds \right)}{4\pi R^2} dV' \quad (1.5)$$

The argument of the exponential function is the optical thickness of the shield between coordinates \mathbf{r}' and \mathbf{r} . Two factors can be recognized in this expression for the uncollided flux: the exponential term which accounts for the attenuation due to the shielding material between \mathbf{r}' and \mathbf{r} , and the $1/R^2$ term which accounts for the geometrical attenuation.

To calculate the requested detector response $D(\mathbf{r})$, the flux is multiplied with the proper detector response function $R(E)$, which is usually of the point isotropic type, and integrated over energy:

$$D(\mathbf{r}) = \int_0^{\infty} \int_{all V} \frac{R(E) S(\mathbf{r}', E) \exp \left(- \int_0^R \Sigma_t(\mathbf{r} - s\Omega, E) ds \right)}{4\pi R^2} dV' dE \quad (1.6)$$

Neglecting the scattering source as was done to derive Eq. (1.6) for the detector response, is of course not very realistic. Therefore, a buildup factor is introduced, which is defined as the ratio of the total detector response (due to both collided and uncollided fluxes) and the detector response due to the uncollided flux only. Because the total cross section for gamma rays is only

smoothly dependent on energy and atomic number, the buildup factor for a specific detector response function is a smooth function of energy, atomic number and shield thickness. Moreover, the buildup factor is dependent on the detector response function used. The buildup factor has to be calculated beforehand by use of transport codes, which do include the inscattering source term in the solution of the transport equation.

Eq. (1.1) can also be used to derive the integral form of the transport equation which forms the basis for Monte Carlo codes [Spa69, Dub86]. The same integrating factor as was used to derive Eq. (1.3) can be used to get [Wes81a]:

$$\begin{aligned} & \frac{\partial \left(\phi(\mathbf{r}', E, \Omega) \exp \left(- \int_0^R \Sigma_t(\mathbf{r} - s\Omega, E) ds \right) \right)}{\partial R} = \\ & = S(\mathbf{r}', E, \Omega) \exp \left(- \int_0^R \Sigma_t(\mathbf{r} - s\Omega, E) ds \right) + \\ & \int_{4\pi} \int_0^\infty \Sigma_s(\mathbf{r}', E' \rightarrow E, \Omega' \rightarrow \Omega) \phi(\mathbf{r}', E', \Omega') dE' d\Omega' \exp \left(- \int_0^R \Sigma_t(\mathbf{r} - s\Omega, E) ds \right) \end{aligned} \quad (1.7)$$

Integrating all terms for R from 0 to ∞ , and applying the boundary condition $\phi(\infty, E, \Omega) \exp \left(- \int_0^\infty \Sigma_t(\mathbf{r} - s\Omega, E) ds \right) = 0$, gives:

$$\begin{aligned} \phi(\mathbf{r}, E, \Omega) &= \int_0^\infty S(\mathbf{r}', E, \Omega) \exp \left(- \int_0^R \Sigma_t(\mathbf{r} - s\Omega, E) ds \right) dR + \\ &+ \int_0^\infty \int_{4\pi} \int_0^\infty \phi(\mathbf{r}', E', \Omega') \Sigma_s(\mathbf{r}', E' \rightarrow E, \Omega' \rightarrow \Omega) \cdot \\ &\quad \cdot \exp \left(- \int_0^R \Sigma_t(\mathbf{r} - s\Omega, E) ds \right) dE' d\Omega' dR \end{aligned} \quad (1.8)$$

If each term is multiplied with $\Sigma_t(\mathbf{r}, E)$, one gets for the collision density $\psi(\mathbf{r}, E, \Omega)$, the particle density entering a collision per unit energy and per

unit solid angle around (\mathbf{r}, E, Ω) :

$$\begin{aligned} \psi(\mathbf{r}, E, \Omega) = & \int_0^\infty S(\mathbf{r}', E, \Omega) \Sigma_t(\mathbf{r}, E) \exp\left(-\int_0^R \Sigma_t(\mathbf{r} - s\Omega, E) ds\right) dR + \\ & + \int_0^\infty \int_{4\pi} \int_0^\infty \psi(\mathbf{r}', E', \Omega') \frac{\Sigma_s(\mathbf{r}', E' \rightarrow E, \Omega' \rightarrow \Omega)}{\Sigma_t(\mathbf{r}', E')} \\ & \cdot \Sigma_t(\mathbf{r}, E) \exp\left(-\int_0^R \Sigma_t(\mathbf{r} - s\Omega, E) ds\right) dE' d\Omega' dR \end{aligned} \quad (1.9)$$

Introducing the collision kernel:

$$C(\mathbf{r}', E' \rightarrow E, \Omega' \rightarrow \Omega) = \frac{\Sigma_s(\mathbf{r}', E' \rightarrow E, \Omega' \rightarrow \Omega)}{\Sigma_t(\mathbf{r}', E')} \quad (1.10)$$

which describes the probability that a particle entering a collision at \mathbf{r}' scatters from energy E' to dE around E and from direction Ω' to solid angle $d\Omega$ around Ω , and the transport kernel:

$$T(\mathbf{r}' \rightarrow \mathbf{r}, E) = \Sigma_t(\mathbf{r}, E) \exp\left(-\int_0^R \Sigma_t(\mathbf{r} - s\Omega, E) ds\right) \quad (1.11)$$

which is the properly normalised probability density function (PDF) for particle transport from \mathbf{r}' to \mathbf{r} at energy E per unit path length, this equation can be simplified to:

$$\begin{aligned} \psi(\mathbf{r}, E, \Omega) = & \int_0^\infty S(\mathbf{r}', E, \Omega) T(\mathbf{r}' \rightarrow \mathbf{r}, E) dR + \\ & + \int_0^\infty \int_{4\pi} \int_0^\infty \psi(\mathbf{r}', E', \Omega') C(\mathbf{r}', E' \rightarrow E, \Omega' \rightarrow \Omega) T(\mathbf{r}' \rightarrow \mathbf{r}, E) dE' d\Omega' dR \end{aligned} \quad (1.12)$$

The normalisation factor for the collision kernel of a non-multiplying medium is $\Sigma_s(\mathbf{r}', E')/\Sigma_t(\mathbf{r}', E')$, which is usually called the non-absorption probability. Fission, (n,2n), (n,3n) reactions etc., can be easily included in the collision

kernel, by adding these cross sections with the proper multiplication to the scattering cross section. The transport kernel is usually written as the probability for transport from \mathbf{r}' to \mathbf{r} per unit volume instead of per unit path length. A delta function is introduced, therefore, to guarantee that only particles travelling from \mathbf{r}' to \mathbf{r} contribute to the collision density at \mathbf{r} :

$$T(\mathbf{r}' \rightarrow \mathbf{r}, E, \Omega) = \frac{T(\mathbf{r}' \rightarrow \mathbf{r}, E)}{|\mathbf{r}' - \mathbf{r}|^2} \delta\left(\Omega - \frac{\mathbf{r} - \mathbf{r}'}{|\mathbf{r} - \mathbf{r}'|}\right) \quad (1.13)$$

Note that this transport kernel has an extra argument Ω to distinguish it from the transport kernel per unit path length, although this latter kernel also depends on Ω .

The expression for the particle density emerging from collisions or the source per unit energy and per unit solid angle as a function of the collision density, reads:

$$\chi(\mathbf{r}, E, \Omega) = S(\mathbf{r}, E, \Omega) + \int_{4\pi} \int_0^\infty \psi(\mathbf{r}, E', \Omega') C(\mathbf{r}, E' \rightarrow E, \Omega' \rightarrow \Omega) dE' d\Omega' \quad (1.14)$$

Likewise, the expression for the collision density as a function of the emergent particle density reads:

$$\psi(\mathbf{r}, E, \Omega) = \int_{allV} \chi(\mathbf{r}', E, \Omega) T(\mathbf{r}' \rightarrow \mathbf{r}, E, \Omega) dV' \quad (1.15)$$

Eqs. (1.14) and (1.15) can be combined to form an integral equation for the emergent particle density:

$$\begin{aligned} \chi(\mathbf{r}, E, \Omega) = & S(\mathbf{r}, E, \Omega) + \\ & + \int_{allV} \int_{4\pi} \int_0^\infty \chi(\mathbf{r}', E', \Omega') T(\mathbf{r}' \rightarrow \mathbf{r}, E', \Omega') C(\mathbf{r}, E' \rightarrow E, \Omega' \rightarrow \Omega) dE' d\Omega' dV' \end{aligned} \quad (1.16)$$

Both the emergent particle density and the collision density are calculated in a Monte Carlo code. First the coordinates, energy group and direction cosines of a particle are sampled from the source density $S(\mathbf{r}, E, \Omega)$, then the next collision point is determined by sampling from the transport kernel $T(\mathbf{r} \rightarrow \mathbf{r}', E)$.

If the particle survives the collision with probability $\Sigma_s(\mathbf{r}', E)/\Sigma_t(\mathbf{r}', E)$, the new energy group and direction cosines are determined from the normalised scattering kernel. The transport kernel and the scattering kernel are used to follow the particle through the system until the particle is absorbed or escaped. Usually, the particle history is not allowed to terminate by absorption, and a weight is assigned to the particle, which is reduced by the non-absorption probability at each collision point. Other means to terminate the particle history must be used in this case, which is explained in Section 7.1.

The quantity of interest D in a Monte Carlo calculation can often be represented as an inner product (integration over whole phase space) of the flux and a detector response function $f(\mathbf{r}, E, \Omega)$:

$$D = \int_{\text{all } V} \int_{4\pi} \int_0^{\infty} f(\mathbf{r}, E, \Omega) \phi(\mathbf{r}, E, \Omega) dE d\Omega dV \quad (1.17)$$

This quantity can easily be converted to an inner product over the collision density or the emergent particle density:

$$D = \int_{\text{all } V} \int_{4\pi} \int_0^{\infty} g(\mathbf{r}, E, \Omega) \psi(\mathbf{r}, E, \Omega) dE d\Omega dV \quad (1.18)$$

and:

$$D = \int_{\text{all } V} \int_{4\pi} \int_0^{\infty} h(\mathbf{r}, E, \Omega) \chi(\mathbf{r}, E, \Omega) dE d\Omega dV \quad (1.19)$$

where detector response functions $f(\mathbf{r}, E, \Omega)$, $g(\mathbf{r}, E, \Omega)$ and $h(\mathbf{r}, E, \Omega)$ are related to each other via:

$$g(\mathbf{r}, E, \Omega) = \frac{f(\mathbf{r}, E, \Omega)}{\Sigma_t(\mathbf{r}, E)} \quad (1.20)$$

and:

$$h(\mathbf{r}, E, \Omega) = \int_{\text{all } V} T(\mathbf{r} \rightarrow \mathbf{r}', E, \Omega) g(\mathbf{r}', E, \Omega) dV' \quad (1.21)$$

Several estimators can be used to extract information from the particle histories. The simplest estimator to be used is probably the collision estimator, which gives a contribution to the detector response at each collision point.

The total number of particles entering a collision in a specific volume and energy range per unit time, is equal to the collision rate in that volume and energy range, and the response function $g(\mathbf{r}, E, \Omega)$ can be used to convert this collision rate to other detector responses.

Sometimes it is more convenient, however, to extract information from the neutron path itself. Two estimators can be used for this purpose: the track length estimator and the boundary crossing estimator. The first one gives a detector contribution equal to the product of the particle weight and the track length of the particle in a zone specified beforehand. The total detector response is thus equal to the total distance travelled by all particles in that zone, which is by definition equal to the particle flux integrated over that zone. The boundary crossing estimator just counts the weights of particles crossing a boundary specified beforehand, and the total detector response is thus equal to the integrated particle current through that surface. One can also count the particle weights divided by the absolute value of the cosine of the particle direction and the normal to the surface, which gives the particle flux integrated over the surface. It is noted that both the track length estimator and the boundary crossing estimator can be deduced from the collision estimator [Dub86]. The response function $f(\mathbf{r}, E, \Omega)$ can be used to convert the flux, calculated by the track length estimator or boundary crossing estimator, to other detector responses.

If the detector response is to be calculated at a point, use can be made of point estimators, which calculate at each collision point the probability that the outgoing direction of the particle is directed to the detector point, and that the particle collides at the detector point (per unit volume). These estimators are usually available in Monte Carlo codes, and because they mostly give an estimate of the flux at the detector point, the function $f(\mathbf{r}, E, \Omega)$ can be used to calculate other detector responses.

Introducing the kernels:

$$L(\mathbf{P}' \rightarrow \mathbf{P}) = T(\mathbf{r}' \rightarrow \mathbf{r}, E', \Omega')C(\mathbf{r}, E' \rightarrow E, \Omega' \rightarrow \Omega) \quad (1.22)$$

and:

$$K(\mathbf{P}' \rightarrow \mathbf{P}) = C(\mathbf{r}', E' \rightarrow E, \Omega' \rightarrow \Omega)T(\mathbf{r}' \rightarrow \mathbf{r}, E, \Omega) \quad (1.23)$$

where \mathbf{P}' and \mathbf{P} are the six-dimensional scalar coordinates of the particle, one can write the integral transport equations for the collision density and the

emergent particle density as (see Eqs. (1.12) and (1.16)):

$$\psi(\mathbf{P}) = Q(\mathbf{P}) + \int_{\Gamma} \psi(\mathbf{P}')K(\mathbf{P}' \rightarrow \mathbf{P})d\mathbf{P}' \quad (1.24)$$

with Q being the first collision density, and:

$$\chi(\mathbf{P}) = S(\mathbf{P}) + \int_{\Gamma} \chi(\mathbf{P}')L(\mathbf{P}' \rightarrow \mathbf{P})d\mathbf{P}' \quad (1.25)$$

The equations, mathematically adjoint to Eqs. (1.24) and (1.25), can be written as:

$$\psi^*(\mathbf{P}) = Q^*(\mathbf{P}) + \int_{\Gamma} \psi^*(\mathbf{P}')K(\mathbf{P} \rightarrow \mathbf{P}')d\mathbf{P}' \quad (1.26)$$

and:

$$\chi^*(\mathbf{P}) = S^*(\mathbf{P}) + \int_{\Gamma} \chi^*(\mathbf{P}')L(\mathbf{P} \rightarrow \mathbf{P}')d\mathbf{P}' \quad (1.27)$$

where Q^* and S^* are still arbitrary source functions yet, and ψ^* and χ^* are the solutions of the adjoint transport equations, with a physical meaning dependent on the source functions. The adjoint functions become of use if appropriate source functions are chosen. As can be shown, the following definitions make sense:

$$Q^*(\mathbf{P}) = g(\mathbf{P}) \quad (1.28)$$

and:

$$S^*(\mathbf{P}) = \int_{allV} T(\mathbf{r} \rightarrow \mathbf{r}', E, \Omega)g(\mathbf{r}', E, \Omega)dV' = h(\mathbf{r}, E, \Omega) \quad (1.29)$$

Multiplying Eq. (1.24) with $\psi^*(\mathbf{P})$ and Eq. (1.26) with $\psi(\mathbf{P})$, integrating both equations for \mathbf{P} over whole phase space, and subtracting one equation from the other, one obtains for D :

$$D = \int_{\Gamma} g(\mathbf{P})\psi(\mathbf{P})d\mathbf{P} = \int_{\Gamma} Q(\mathbf{P})\psi^*(\mathbf{P})d\mathbf{P} \quad (1.30)$$

In the same way for χ and χ^* , one gets for D :

$$D = \int_{\Gamma} h(\mathbf{P})\chi(\mathbf{P})d\mathbf{P} = \int_{\Gamma} S(\mathbf{P})\chi^*(\mathbf{P})d\mathbf{P} \quad (1.31)$$

To distinguish between $\psi^*(\mathbf{P})$ and $\chi^*(\mathbf{P})$, the notation from literature will be used [Tan77, Wes81a]. The event value $\psi^*(\mathbf{P})$ then has the meaning of the expected detector response per particle entering a collision at \mathbf{P} , while the point value $\chi^*(\mathbf{P})$ has the meaning of the expected detector response per particle emerging from a collision or emitted by the source at \mathbf{P} .

It will now be shown that the solution of the adjoint integro-differential transport equation ϕ^* , with detector response function $f(\mathbf{r}, E, \Omega)$ as source function, is equal to the point value as defined by Eqs. (1.27) and (1.29). The adjoint form of Eq. (1.1) writes:

$$-\Omega \cdot \nabla \phi^*(\mathbf{r}, E, \Omega) + \Sigma_t(\mathbf{r}, E) \phi^*(\mathbf{r}, E, \Omega) = f(\mathbf{r}, E, \Omega) + \int_{-4\pi}^{\infty} \int_0^{\infty} \Sigma_s(\mathbf{r}, E \rightarrow E', \Omega \rightarrow \Omega') \phi^*(\mathbf{r}, E', \Omega') dE' d\Omega' \quad (1.32)$$

Multiplying Eq. (1.1) with $\phi^*(\mathbf{r}, E, \Omega)$ and integrating over whole phase space, multiplying Eq. (1.32) with $\phi(\mathbf{r}, E, \Omega)$ and also integrating over whole phase space, and subtracting one equation from the other, gives:

$$D = \int_{\Gamma} f(\mathbf{P}) \phi(\mathbf{P}) dP = \int_{\Gamma} S(\mathbf{P}) \phi^*(\mathbf{P}) dP = \int_{\Gamma} S(\mathbf{P}) \chi^*(\mathbf{P}) dP \quad (1.33)$$

The latter equality is valid by Eq. (1.31). The function ϕ^* is thus equal to the point value χ^* .

The physical meaning of the point value was already given in Eq. (1.31). In particular it will now be shown that the response of an isotropic point source with unit source strength at (\mathbf{r}_0, E_0) can be expressed in terms of the point value at the same coordinates. From Eq. (1.31) follows:

$$\begin{aligned} D_p &= \int_{\Gamma} S(\mathbf{P}) \chi^*(\mathbf{P}) dP = \int_{allV} \int_{-4\pi}^{\infty} \int_0^{\infty} S(\mathbf{r}, E, \Omega) \chi^*(\mathbf{r}, E, \Omega) dE d\Omega dV = \\ &= \int_{allV} \int_{-4\pi}^{\infty} \int_0^{\infty} \frac{1}{4\pi} \delta(\mathbf{r} - \mathbf{r}_0) \delta(E - E_0) \chi^*(\mathbf{r}, E, \Omega) dE d\Omega dV = \\ &= \frac{1}{4\pi} \int_{-4\pi}^{\infty} \chi^*(\mathbf{r}_0, E_0, \Omega) d\Omega = \frac{1}{4\pi} \chi^*(\mathbf{r}_0, E_0) \end{aligned} \quad (1.34)$$

The point value used here is the solution of Eq. (1.32), with the angular dependent detector response function $f(\mathbf{r}, E, \boldsymbol{\Omega})$ as source. The response of an isotropic point source is thus seen to be equal to the point value at the same coordinates, averaged over the angular space 4π . If the detector response function is isotropic, $f(\mathbf{r}, E) = 4\pi f(\mathbf{r}, E, \boldsymbol{\Omega})$ is often used as a source function in the adjoint equation, and the angular integrated point value then obtained is exactly equal to the detector response of an isotropic point source.

Knowledge of the value functions in a given shield configuration can be used to enhance the efficiency of Monte Carlo calculations. In fact, exact knowledge of the value functions makes a Monte Carlo calculation redundant, because the detector response can be calculated from Eq. (1.30). Rough knowledge of the value functions throughout the shield and over the energy range of interest, enables one to spend more CPU time in a Monte Carlo calculation on the important parts of the shield and energy region, thereby increasing the efficiency of the calculation.

Chapter 2

MARMER, a Flexible Gamma Ray Point-Kernel Shielding Code¹

2.1 Introduction

Point-kernel codes for gamma ray shielding exist for quite a long time. In these codes, an exponential attenuation kernel is used to calculate the detector response due to unscattered radiation, while the scattered radiation is accounted for by use of a buildup factor. The simplicity of the method leads to low CPU times, compared with more advanced methods like Monte Carlo and discrete ordinates methods. Furthermore, the input preparation for point-kernel shielding codes is much easier than for the advanced methods mentioned above. Nevertheless do point-kernel codes give good results for many gamma ray shielding problems, even for very detailed geometries. The method is, however, not in general usable for neutron shielding problems because of the very irregular neutron cross section as a function of energy and shielding material. Furthermore, no gamma spectrum information can be obtained by this method, nor does it give reliable results for oblique incident radiation, although a correction to the buildup factor can be made in this case, as is done in the code RANKERN [Mil83].

Many of the point-kernel shielding codes available are rather aged and have restrictions with respect to geometry input, source description, etc. In many cases, for example in the QAD [Cai77] and ISOSHLD [Eng66] codes, volume sources are divided into volume elements to perform a numerical integration of the attenuation kernel over the source volumes. This restricts the geometry of the source and can lead to errors or large CPU times dependent on how many volume elements are chosen. In PATH [Su83], a check on source points is made, which enables one to use more complicatedly shaped source volumes.

¹This chapter is an adapted version of [Klo88, Klo90c]

Some other codes, RANKERN and MERCURE-IV [Dev74] for example, avoid this problem by performing a stochastic integration over the source volume.

Some fitting functions to buildup factor data introduce errors for low Z materials and low energies, for example Taylor's formula [Chi84] utilized in ISOSHL. Therefore, it is recommended that the geometric progression formula [Tru88] should be used (QAD) or tabulated buildup factors which are interpolated for atomic number, energy and shield thickness (MERCURE-IV). QAD uses a single-material buildup factor for multilayered shields. This can lead to errors if the energy spectrum at the calculation point is determined by more than one shield layer. Other methods, like the methods of Kitazume and Broder (see Section 2.3.7) give better results in these cases. Furthermore, data libraries are not always up-to-date. Some codes still use buildup factor data compiled by Goldstein and Wilkins in 1954 [Gol54], while recently compiled buildup factors are available [Tru88].

Geometry input is preferably done by use of some kind of combinatorial geometry, rather than defining (quadratic) surfaces. In combinatorial geometry, simple geometrical bodies are combined to complex zones of homogeneous composition by use of operators. This is utilized in QAD, RANKERN and PATH, for example. To perform more rigorous calculations, it is desirable that part of the input for a point-kernel code can be used by a Monte Carlo code (for example, some input of RANKERN can be used in conjunction with McBEND [Mil83]).

Some codes, like ISOSHL and QAD, can handle only isotropic sources. Sometimes it is required, however, to model a surface source due to contamination or leakage currents (in streaming problems) with a "cosine to the power p " boundary source. This option is available in RANKERN. To calculate the source spectrum, a very useful option to calculate the gamma source spectrum due to irradiated fuel by use of a built-in fission product inventory code (RIBD) is present in ISOSHL.

The above considerations show that each shielding code has one or more useful options, but also some weaknesses. To have available a user friendly, general purpose gamma ray shielding code with many useful options, it was decided to develop a new code. This code is entitled MARMER, and it is based on the MARS [Wes84] geometry package, which is also used by the MORSE-SGC/S Monte Carlo code [Wes81a], and the MERCURE-IV shielding code. MARMER can be used for gamma ray shielding design of nuclear power

plants, storage facilities and spent fuel transport casks. Several useful options (of which some are also available in other codes) are added to make it usable for many purposes.

2.2 Calculational Method

In point-kernel shielding codes, an exponential attenuation kernel is used to calculate the unscattered particle flux at a point due to a point source, while the contribution of the scattered particles is accounted for by use of a buildup factor. If another quantity is to be calculated, e.g. energy flux, dose-equivalent rate or energy absorption rate, a detector response function is used which relates the particle flux to the requested detector response. The detector response $D(\mathbf{r}_d)$ at point \mathbf{r}_d due to a mono-energetic isotropic point source at point \mathbf{r}_s with energy E and source strength S_p becomes, according to the point-kernel approach:

$$D(\mathbf{r}_d) = B(Z, \Sigma_t r, E) R(E) S_p(\mathbf{r}_s, E) \frac{\exp(-\Sigma_t r)}{4\pi r^2} \quad (2.1)$$

where B is the buildup factor, R the detector response function, Z and Σ_t the atomic number and total cross section of the shield, respectively, and r the shield thickness along the ray from \mathbf{r}_s and \mathbf{r}_d .

Eq. (2.1) can be generalized to multilayered shields and volume sources with source volume density $S_v(\mathbf{r}_s, E, \Omega)$ and volume V_s :

$$D(\mathbf{r}_d) = \int_{V_s} \int_0^\infty B(\eta, E) R(E) S_v(\mathbf{r}_s, E, \Omega) \frac{\exp(-\eta)}{(\sum_i r_i)^2} dE dV \quad (2.2)$$

where r_i is the thickness of shield layer i along the ray from \mathbf{r}_s to \mathbf{r}_d , and η is the total optical shield thickness along that ray. The buildup factor is an effective one, such that the effect of the multilayered shield is accounted for (see Section 2.3.7).

The integrations over the source volume and energy range in Eq. (2.2) are done by a Monte Carlo integration method known as importance sampling. This method is extensively described in literature [Dev74, Klo90a], but will be outlined here. The base of the method is that the source zone (a zone is a part of geometry with homogeneous composition) and energy range are sampled

according to a probability density function (PDF) calculated beforehand. The contributions to the detector response of all samples are averaged to obtain the final value of the integral. If the PDF is properly chosen and the number of samples is sufficiently large, the variance of the answer can be acceptably small or (theoretically) even zero. The advantage of this method in comparison with numerical integration, is that the source zone can be arbitrarily shaped and that it is rather fast because those parts of the source zone and energy range, which are not contributing to the detector response, are scarcely sampled.

Source systems are defined to describe the spatial description of the source. A source system is a coordinate system in either cartesian, cylindrical or spherical coordinates. The outer boundaries of the source system are chosen such that it encompasses the source zone entirely. The source system is now divided into volume elements and these volume elements are used to describe the spatial source strength and to calculate the PDF for the integration over the source volume. It must be emphasized that the volume elements are defined independently of the source zone and that subsequently the source zone can be arbitrarily shaped. Furthermore, the volume elements can be crude ones and the CPU time does not depend very much on the number of volume elements chosen. Several source systems may be defined and each source system may contain several source zones. The source description is complete if for each source system, it is made clear which zone in the source system is a source zone, the energy spectrum of each source zone is known and the spatial source strength description is given as a function of the volume elements of the source system.

To sample particles in the source zone, volume elements of each source system are subdivided into source and non-source volume elements. Particles are only sampled from source volume elements. A volume element will be treated as a non-source volume element if its centre is not in a source zone, otherwise it will be treated as a source volume element. Because the boundaries of the source zones do not have to coincide with source system boundaries (volume element boundaries) non-source volume elements can partly belong to a source zone. An option in the program is available to search for such volume elements and, if found, to treat them as source volume elements.

To integrate over energy, the energy range is divided into energy groups. This is done in MARMER by small energy groups which can be collapsed to broad ones (see Section 2.3.2). The source volume density in multigroup

notation in MARMER is then written as:

$$S_v(\mathbf{r}_s, g, \Omega) = S_s(j, \mathbf{r}_s) S_e(j, m, g) S_a(j, \Omega) \quad (2.3)$$

where j , m and g are the indices of the source system, source zone and energy group, respectively. The first factor on the RHS of Eq. (2.3) is the unnormalised spatial source description, given in the input for each source system j . The second term is the normalised spectrum of source zone m in source system j . If unnormalised spectra are given in the input, the spectrum is normalised by MARMER and the source strength of zone m in system j is multiplied with the total integral of the unnormalised spectrum. The third term is the normalised angular distribution. If an unnormalised distribution is given in the input, a normalisation is performed and the spatial source strength of each zone m in source system j is again multiplied with the total integral of the unnormalised angular distribution.

The integral, which has to be calculated in MARMER, can then be written as:

$$D(\mathbf{r}_d) = \int_{V_s} \sum_g S_s(j, \mathbf{r}_s) S_e(j, m, g) S_a(j, \Omega) G_R(|\mathbf{r}_s - \mathbf{r}_d|, g) dV \quad (2.4)$$

where G_R is the response kernel including the buildup factor, detector response function and attenuation kernel. To evaluate this integral two importance functions are calculated. The energetic importance function $I_e(m, g)$ and the spatial importance function $I_s(k)$. The first one is defined for each source zone m and is a measure of the relative detector contribution of energy group g averaged over source zone m . The second one is calculated for each volume element k and is a measure of the detector contribution of each volume element per unit source strength.

To perform the Monte Carlo integration in MARMER, a source volume element is selected according to a PDF calculated beforehand:

$$P_s(k) = A S_s(j, \mathbf{r}_k) \Delta V_k I_s(k) \sum_{g=1}^G S_e(j, m, g) I_e(m, g) \quad (2.5)$$

where \mathbf{r}_k and ΔV_k are the centre coordinates and volume of volume element k . A is merely a constant to normalize the PDF to one. Subsequently, a point

in that volume element is sampled uniformly:

$$P_k(r_s) = \frac{1}{\Delta V_k} \quad (2.6)$$

and an energy group is selected according to the PDF:

$$P_e(j, m, g) = \frac{S_e(j, m, g)I_e(m, g)}{\sum_{g'=1}^G S_e(j, m, g')I_e(m, g')} \quad (2.7)$$

The coordinates of point r_s and the energy group sampled, constitute a hypothetical particle and the detector response contribution of this particle is calculated. The quantity to be evaluated (called X), is equal to this detector response contribution divided by the three probability density functions given by Eqs. (2.5), (2.6) and (2.7). The proces of sampling the coordinates and energy group of a hypothetical particle and calculating X , is repeated many times in order to achieve reasonable statistics. The process described above, becomes slightly more complicated, if the fact that source volume elements can partly belong to non-source zones, is taken into account. This can give zero contributions to the detector response. The variance can be shown to be partly due to these zero contributions and partly due to the variance of the non-zero contributions.

The total number of particles sampled, is divided into L batches each containing M particles in order to calculate the variance. This is done twofold. The first method is called the "batch" method. The mean value of the detector response J_ℓ of all particles in batch ℓ is calculated and the mean value of the total detector response then becomes:

$$\bar{J} = \frac{1}{L} \sum_{\ell=1}^L J_\ell \quad (2.8)$$

An unbiased estimator for the variance of \bar{J} is:

$$S_{\bar{J}}^2 = \frac{1}{L(L-1)} \sum_{\ell=1}^L (J_\ell - \bar{J})^2 \quad (2.9)$$

The second way to calculate the variance is called the "one-particle" method, because it is based on the variance of the particle contributions itself. An

estimator for the variance of the contributions in batch ℓ is:

$$(S_X^2)_\ell = \frac{1}{M} \left(\sum_i X_i^2 - MJ_\ell^2 \right) \quad (2.10)$$

where the summation is over all particles of batch ℓ . The variance of the mean detector response J_ℓ of batch l then becomes:

$$S_{J_\ell}^2 = \frac{1}{M} (S_X^2)_\ell \quad (2.11)$$

and, by Eq. (2.8), the variance of the mean detector response of all batches becomes:

$$S_J^2 = \frac{1}{L^2} \sum_{\ell=1}^L (S_{J_\ell}^2) \quad (2.12)$$

Theoretically, the variance of S_J^2 according to Eq. (2.9) is larger than the variance of S_J^2 according to Eq. (2.12) [Dub79]. This can be understood intuitively, because the information of the individual detector contributions of the particles in a particular batch, is not used in Eq. (2.9). The batch method has the advantage, however, that a large number of particles contribute to J_ℓ . Therefore, J_ℓ is normally distributed by the central limit theorem and the interpretation of the variance of the batch method in terms of confidence intervals and corresponding levels of confidence, is easier.

The calculation is stopped if the relative standard deviation, calculated from the maximum of the variances according to Eqs. (2.9) and (2.12), divided by the mean value of the detector response according to Eq. (2.8), is less than a level given beforehand in the input or if the maximum number of batches given in the input is reached.

2.3 Options in MARMER

2.3.1 Geometry Description

Geometry input is described by use of the MARS geometry package which makes use of combinatorial geometry combined with an array repeating system. This package is also used by the MORSE-SGC/S Monte carlo code. It allows the user to define parts of geometry only once and to repeat them throughout the geometry.

In combinatorial geometry, physical structures are described by nine basic bodies:

1. RPP - Rectangular Parallelepiped
2. SPH - Sphere
3. RCC - Right Circular Cylinder
4. REC - Right Elliptic Cylinder
5. TRC - Truncated Right Angle Cone
6. ELL - Ellipsoid
7. WED or RAW - Right Angle Wedge
8. BOX - Box
9. ARB - Arbitrary Polyhedron

All the bodies may be arbitrarily oriented in space, except for the RPP which must have its sides parallel to the coordinate axes. These bodies may be combined to code zones by use of the "AND" or "NOT" operator. The AND operator means that the code zone being described is wholly contained inside the body, while the NOT operator means that the code zone being described is wholly contained outside the body. Several code zones may be combined to an input zone (zone of homogeneous composition) by use of the "OR" operator, which takes the union of the code zones.

Parts of geometry may be repeated throughout the geometry by use of "arrays" and "universes". An array is a rectangular body in geometry which can be subdivided in cells along both X and Y and Z axes. Subsequently, a local universe is defined, which fits exactly in one such a cell and where the contents of one cell is described in detail. Each array cell may now be filled by the contents of the local universe and in this way the contents of the local universe are repeated throughout the geometry. The number of arrays is unlimited and each array may be divided in as many array cells as needed to describe the problem. Furthermore, an unlimited number of local universes may be defined and each array cell may be filled with any arbitrary local universe, provided that it fits exactly in the array cell. Arrays may even be

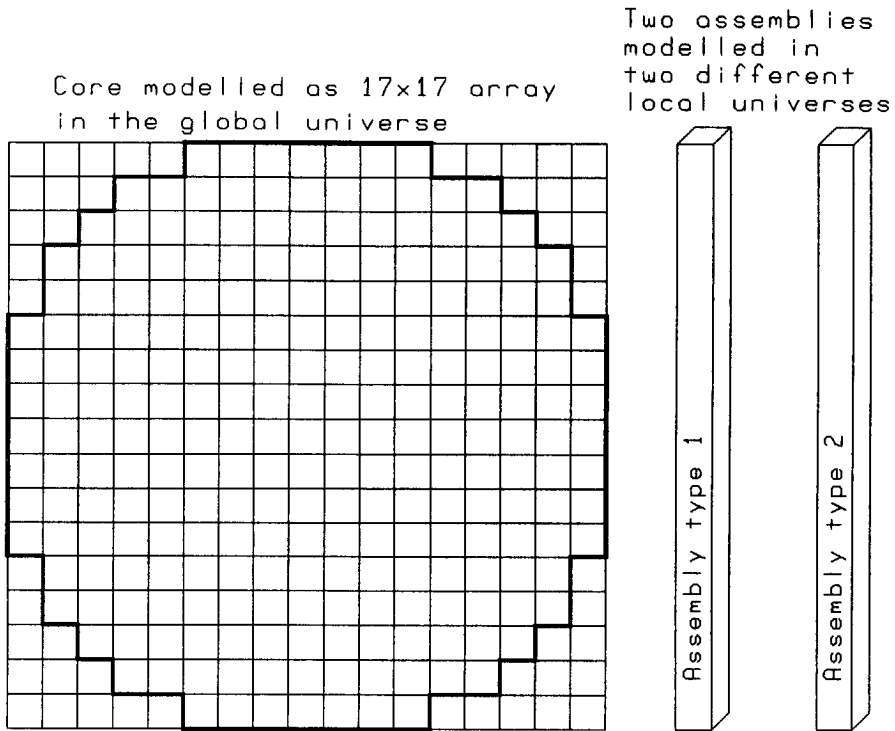


Figure 2.1: Sketch of the use of an array to model a PWR core with two different types of fuel assemblies.

nested, which means that an array can be defined in a cell of another array or that an array can be defined in a local universe.

The use of arrays is illustrated in Fig. 2.1, where a horizontal cross section of a PWR reactor core is drawn (in bold). An array with 17x17 cells is modelled containing the core. Furthermore, two different types of fuel assemblies are modelled, each in a different local universe. Each type of fuel assemblies may now be placed at any arbitrary array cell in the core. The array cells outside the core can be defined vacant.

2.3.2 Energy Group Structure

In MARMER the energy group structure is defined each time the input is prepared. Therefore, the gamma data library contains microscopic cross sections

for 36 fine energy groups ranging from 0.010 to 14.0 MeV in the VITAMIN-C structure [Rou79]. These fine group cross sections may be collapsed to broad ones with the energy width of each group taken as a weight:

$$\sigma_G = \frac{\sum_{g=g'}^{g''} \sigma_g \Delta E_g}{\sum_{g=g'}^{g''} \Delta E_g} \quad (2.13)$$

Here, σ_G is the microscopic cross section of broad group G containing fine groups g' up to and including g'' . ΔE_g is the width of energy group g .

2.3.3 Spectrum Definition

A spectrum in MARMER is defined as the number of particles originating in each energy group per unit source volume, per unit time ($\text{cm}^{-3} \text{s}^{-1}$). It can be defined in four different ways:

1. The integrated spectrum ($\text{cm}^{-3} \cdot \text{s}^{-1}$) in each energy group may be given.
2. A pointwise spectrum may be defined by giving a number of arbitrary energy points (MeV) and corresponding spectrum values ($\text{cm}^{-3} \cdot \text{s}^{-1} \cdot \text{MeV}^{-1}$). This point spectrum is converted to a group spectrum described above, by integrating over each energy group linear in lethargy.
3. The spectrum may be calculated by MARMER by reading a binary file containing nuclide concentrations calculated by the fuel depletion code ORIGEN-S [Her84]. These concentrations are converted to a group spectrum by use of the MARMER nuclide library containing gamma decay energies, yields and half life times for over 1000 nuclides. To facilitate the use of ORIGEN-S, a preprocessor was written for simple irradiation and decay problems.
4. This option is very similar to the previous one, except for the nuclide concentrations, which are now given in the input rather than read from a binary file. The nuclide identification is given in the input together with the activity of that nuclide and a delay time. Decay of the nuclide during that time is accounted for in MARMER.

2.3.4 Spatial Source Description

As stated in Section 2.2, the spatial source description is done by source systems divided into volume elements. Source systems may be defined in cartesian (X, Y, Z) , cylindrical (R, Φ, Z) or spherical coordinates (R, Θ, Φ) . The three coordinates will be referred to as the (U, V, W) coordinates. The spatial source description may be done separately for each coordinate:

$$S(U, V, W) = F_1(U) F_2(V) F_3(W) \quad (2.14)$$

or separately for one coordinate and the other two:

$$S(U, V, W) = F(U) G(V, W) \quad (2.15)$$

$$S(U, V, W) = F(V) G(U, W) \quad (2.16)$$

$$S(U, V, W) = F(W) G(U, V) \quad (2.17)$$

or as a combined function of all three coordinates. Here S is the spatial source description and F and G are functions which are described hereafter.

Function F can have the following forms:

1. F can be a constant given in the input.
2. F can be cosine distributed:

$$F(U) = A \cos \left(\frac{\pi(U - U_o)}{B} \right) \quad (2.18)$$

where the constants A , B and U_o are given in the input.

3. F can be exponentially distributed:

$$F(U) = A \exp(B(U - U_o)) \quad (2.19)$$

where the constants A , B and U_o are again given in the input.

4. F can be defined at the boundaries of each interval in direction of U . The source strength is linearly interpolated between two adjacent points.
5. F can be defined at the centre of each interval in direction of U . The source strength is supposed constant in this direction for the whole volume element.

6. F can be defined at points in direction of U independent of the boundaries of the volume elements in direction of U . Again the source strength is linearly interpolated between two adjacent points.

The function G of two coordinates can be defined by giving the value of G at each nodal point of the area elements in the (U, V) plane (thus at the crossing point between four neighbouring area elements) or at the centre of each area element in the (U, V) plane. The function S of three coordinates can be given at the centre of each volume element.

2.3.5 Angular Source Description

The angular source description $S_a(j, \Omega)$ for each source system j (see Eq. (2.3)) is supposed to be azimuthally symmetric around a predefined axis, which is given in the input and which is defined for each source system separately:

$$S_a(j, \Omega) = \frac{1}{2\pi} f(\mu) \quad (2.20)$$

where $f(\mu)$ gives the angular dependence on the cosine of the polar angle μ , which must be given in the input and which can have one of the following forms:

1. $f(\mu)$ can be isotropic between two angles defined by their cosines μ_1 and μ_2 which must be given in the input:

$$f(\mu) = \frac{1}{\mu_2 - \mu_1} \quad (2.21)$$

and zero outside that range.

2. $f(\mu)$ can have a "cosine to the power p " distribution between two angles defined by their cosines μ_1 and μ_2 :

$$f(\mu) = \frac{(p+1) |\mu|^p}{|\mu_2|^{p+1} \pm |\mu_1|^{p+1}} \quad (2.22)$$

where the $+$ sign in the denominator is used if μ_2 and μ_1 have unequal sign, meaning that one direction is pointing in the positive hemisphere and the other in the negative one, and the $-$ sign is used if both cosines have positive sign, meaning that the two directions are pointing in the

positive hemisphere. This option is especially useful for calculating the line-of-sight flux in ducts, where the source at the entrance of the duct can be represented by a current.

3. $f(\mu)$ can be given for several discrete angles, whose values must also be given in the input. The total integral of the distribution is calculated by linearly interpolating between these values and the spatial source distribution is multiplied with this integral value (see Eq. (2.3)).

2.3.6 Material Composition

To calculate the interaction coefficients and buildup factors of each shield material, the composition of each material must be defined. This can be done in two ways:

1. The number of elements and the atomic number and atomic concentration (10^{-24} cm^{-3}) of each element in each shield material can be given.
2. The number of elements and the atomic number and occurrence (e.g. number of atoms in a molecule) of each element in each shield material can be given, together with the density (g.cm^{-3}) of the shield material.

Furthermore, for each shield material has to be defined whether a buildup factor (dose-equivalent, energy absorption or both) has to be calculated or not. If this is the case and the shield material consists of a mixture of elements, an effective atomic number is obtained by calculating the interaction coefficient per electron of the shield material for each energy group and interpolating in a library containing interaction coefficients of elements. The atomic number of the element with the same interaction coefficient per electron as the shield material is taken as the effective atomic number of that material. This number may differ slightly from one energy group to another. After the atomic number of the shield material is calculated, the buildup factor of that material is obtained by interpolating in the buildup factor library for the atomic number calculated and the mean energy of each energy group.

2.3.7 Detector Response Functions and Buildup Factors

Besides the cartesian coordinates of each calculation point detector, it must be specified for each point which detector response function and which buildup

factor is used. The detector response function relates the unscattered gamma ray flux to dose-equivalent rate, energy absorption rate or gamma energy flux. The buildup factor takes into account the contribution of the scattered radiation. This factor is therefore dependent on the detector response function used.

Several response functions are used in literature [Chi84]. Kerma is an acronym for Kinetic Energy of Radiation produced per unit MA_{ss} in matter, and the kerma response function gives the relation between the interacting gamma rays and the kinetic energy transferred to secondary particles (usual electrons) in the material. Air kerma is equal to the energy absorbed in air, and material kerma is equal to the energy absorbed in material, if electronic equilibrium is valid and bremsstrahlung production is negligible. Exposure is another response function, which is a measure of the ionization of air per unit mass. Because the electrons produced by the gamma rays will ionize the air, and because the ionization energy of air is almost independent of electron energy (33.85 eV per ion pair), exposure is a measure of energy absorption in air if electronic equilibrium is valid. If bremsstrahlung production is negligible, exposure will be a measure of air kerma too.

The dose-equivalent response function is by definition different from the air kerma and exposure response functions mentioned above. Dose-equivalent is a measure of biological damage created in tissue, which is especially determined by the linear energy transfer (LET) of the secondary particles produced. This is done by defining a quality factor which depends on the LET in water of these particles. Because gamma rays in tissue mainly produce electrons and because the quality factor of electrons is independent of electron energy, dose-equivalent will be proportional to energy absorption in tissue. If electronic equilibrium is valid and bremsstrahlung is negligible, dose-equivalent will be a measure of tissue kerma too.

Because the relation between exposure and energy absorption in tissue is almost independent of energy, dose-equivalent buildup factors, air kerma buildup factors and exposure buildup factors are used interchangeably, although these three buildup factors are not equal to each other by definition. Also the flux to dose-equivalent, flux to air kerma and flux to exposure response functions are used interchangeably. Similarly, the material kerma buildup factors and energy absorption buildup factors for the same material are used interchangeably. It is interesting to note that generally kerma is easy to calculate, while energy

absorption is easy to measure.

In the buildup factor library, only air kerma and material kerma buildup factors are available. The first one may be used as an approximation to exposure buildup factors or dose-equivalent buildup factors, while the second one may be used as an approximation to energy absorption buildup factors. Several approximate methods to calculate buildup factors for layered shields are available in MARMER:

1. The buildup factor of one specific shield layer (usually the last one) with adapted shield thickness equal to the total shield thickness measured in mean free paths, can be used. This method gives good results if the energy spectrum is dominated by that shield layer.
2. The method of Kitazume [Pon74, Klo90a] can be used. This method is the most advanced one. It tends to approximate the buildup factor of the last shield layer if this layer is thick enough:

$$B(\eta_1) = B_1(\eta_1) \quad (2.23)$$

$$B(\eta_n) = B_n(\eta_n) + (B(\eta_{n-1}) - B_n(\eta_{n-1}))Z_n \quad (2.24)$$

where $B(\eta_n)$ is the Kitazume buildup factor of the shield up to and including shield layer n , B_n is the buildup factor of shield layer n and η_n is the optical shield thickness along the ray from source point to calculation point up to and including shield layer n . Z_n is a factor calculated from Kitazume's coefficients α and β :

$$Z_n = (1 - \beta_{n,n-1}) \exp(-\alpha_{n,n-1} \eta_n) + \beta_{n,n-1} \quad (2.25)$$

Both α and β are tabulated in the buildup factor library for different energies and atomic numbers.

3. The method of Broder [Pon74, Klo90a] can be used. This method is very much like Kitazume's method given above, except for the Z_n factor which equals 1.0 in Broder's method. Effectively, the contribution of each shield layer to the buildup factor is summed to obtain the buildup factor of the total shield.

2.4 MARMER Data Libraries

The MARMER gamma data library contains microscopic cross sections, energy absorption response functions, dose-equivalent response functions and energy flux response functions. All data is given for 36 energy groups in the VITAMIN-C [Rou79] energy group structure for (almost) all elements with atomic number ranging from 1 to 94.

The microscopic cross sections are based on the JEF1.1 library [JEF85], and are taken as the sum of the cross sections for the photoelectric effect, Compton scattering and pair production:

$$\sigma_{g,tot} = \sigma_{g,ph} + \sigma_{g,C} + \sigma_{g,pp} \quad (2.26)$$

Each cross section in Eq. (2.26) is a group averaged one:

$$\sigma_g = \frac{\int_{E_{\epsilon g}} \sigma(E)\phi(E)dE}{\int_{E_{\epsilon g}} \phi(E)dE} \quad (2.27)$$

where the gamma flux $\phi(E)$ is used as a weighting function. Because the flux is generally unknown, a flat flux approximation is used.

To calculate the energy absorption response functions, it is necessary to calculate the energy absorption cross sections. This is done by assuming that both Compton scattering and pair production are partially absorbing, while the photoelectric effect is assumed to be totally absorbing. The energy absorption cross section at energy E therefore becomes:

$$\sigma_a(E) = \sigma_{ph}(E) + f_C(E)\sigma_C(E) + f_{pp}(E)\sigma_{pp}(E) \quad (2.28)$$

where $f_C(E)$ and $f_{pp}(E)$ are the mean energy fractions absorbed in a Compton scattering and pair production, respectively. The second term on the RHS of Eq. (2.28) is calculated by use of the Klein-Nishina formula for Compton scattering [Chi84]:

$$f_C(E) = 1 - \frac{Z\pi r_e^2}{\sigma_C(E)} \left(\frac{\ln(1+2\epsilon)}{\epsilon^3} + \frac{2(1+\epsilon)(2\epsilon^2-2\epsilon-1)}{\epsilon^2(1+2\epsilon)^2} + \frac{8\epsilon^2}{3(1+2\epsilon)^3} \right) \quad (2.29)$$

where Z is the atomic number of the nuclide under consideration, r_e is the classical radius of the electron ($2.818 \cdot 10^{-13}$ cm) and ϵ is the photon energy

expressed in rest mass units, i.e. $\epsilon = E/0.511$ (E in MeV). The third term on the RHS of Eq. (2.28) is calculated easily if it is assumed that two annihilation photons are produced immediately at the same position where the pair production occurs:

$$f_{pp}(E) = 1 - \frac{2}{\epsilon} \quad (2.30)$$

The energy absorption response functions are obtained by multiplying the energy absorption cross sections by energy (MeV) and a conversion factor $k = 1.602 \cdot 10^{-13} \text{ J.MeV}^{-1}$. Subsequently, this function is averaged over energy according to Eq. (2.27) with a constant flux, to obtain a group averaged energy absorption response function. This response function is thus given in J.cm^{-1} and the energy absorption rate calculated by MARMER is given in W.cm^{-3} .

The gamma flux to dose-equivalent conversion factor is obtained by the DOSE code [Kni78]. The gamma flux to energy flux conversion factor is equal to the mean energy of each energy group.

The buildup factor library contains buildup factors taken from the QAD-CGGP point-kernel shielding code [Tru88]. They are tabulated for 15 shield thicknesses with optical thicknesses varying from 0.50 till 50 mfp, for 19 elements with atomic number ranging from 4 till 92 and for 23 energies ranging from 0.03 till 15.0 MeV. Both air kerma and material kerma buildup factors are given.

The nuclide data library contains half life times, decay energies and gamma yields for over 1000 nuclides. All data is taken from the JEF1.1 data file [JEF85].

Chapter 3

Gamma Ray Benchmark Calculations on the TN12 Spent Fuel Shipping Cask by the Point-Kernel Shielding Code MARMER¹

3.1 Introduction

Despite extensive checks and calculations, it is hardly possible to remove all errors from large computer codes. Especially not if many input options can be used together with many other ones. Therefore, the oldest codes used already for many years by different people for all kind of purposes, are generally the most reliable ones in this respect. Unfortunately, they are generally not very user friendly and they lack useful input options.

It is very useful, therefore, to check new programs by so-called benchmark exercises. These exercises are calculations by the code to be checked, from which the results can be compared with results from other codes or with experimental values. It is not to be expected, however, that one benchmark exercise is sufficient to remove all errors from a new code like MARMER [Klo90a, Klo90c]. Many options were checked, therefore, with simple (sometimes unrealistic) problems. Nevertheless, participating in a shielding benchmark is very useful to find systematic deviations of absolute dose rates. In view of this, it was decided to participate in the TN12 shielding benchmark [Dio89, Klo90b], which was organized by the NEACRP Working Group on Fuel Flask Shielding, to check the MARMER code. The benchmark is described and the calculated results are compared with measurements, given in the benchmark.

¹This chapter is an adapted version of [Klo90b]

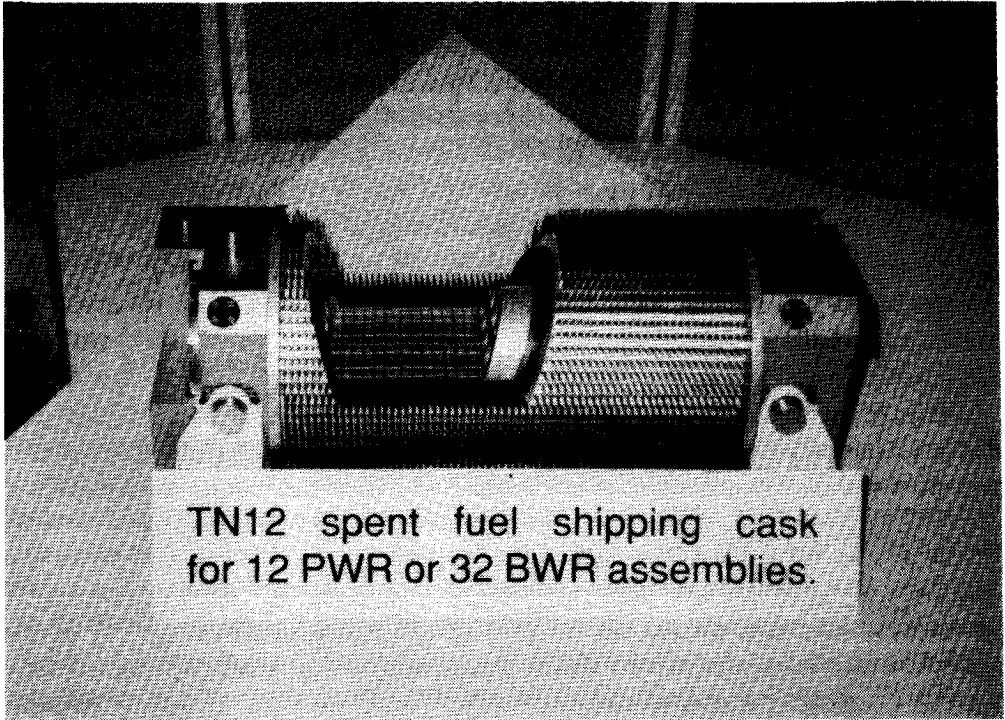


Figure 3.1: Model of a TN12 spent fuel shipping cask.

3.2 Benchmark Description

The TN12 spent fuel shipping cask consists of a steel annulus with inner diameter of 1220 mm and thickness varying from 262 to 302 mm. Areas of the annulus likely to be contaminated during normal operation are covered with stainless steel. Inside the annulus, an aluminium alloy basket containing 12 recesses covered with boron carbide plates, is filled with 12 fuel assemblies. Each assembly is composed of 264 fuel pins, 24 guide tubes and 1 instrumentation guide tube, but in the shielding calculations they are homogenised in six axial zones. The outer side of the annulus is covered with over 3000 copper cooling fins and resin, which are also homogenised in the calculations. The thicknesses of both top and bottom of the cask are 334 and 387 mm, respectively. The total outer diameter of the cask is 2500 mm, while the length, excluding the

wood filled shock absorbers, which were not present during the measurements, is 5345 mm.

The gamma source consists mainly of gamma rays originating in the fissile part of each fuel assembly due to fission and activation products and gamma rays originating in zones above and below the fissile part due to activation products of which ^{60}Co appeared to be the most important one. The fuel assemblies could be subdivided into two groups: one consisting of assemblies 1 to 7 and the other consisting of assemblies 8 to 12. The irradiation and decay times and the axial burnup distribution are the same for the assemblies of each group and are given in the benchmark description. The thermal neutron flux profile above and below the fissile part of the assemblies during irradiation use in the reactor, needed to calculate the ^{60}Co activation at these heights, is the same for both groups of assemblies and is once again given in the benchmark description.

3.3 Calculations

The fission products source and the ^{60}Co activation source in the fissile part of the fuel assemblies are calculated by the fuel depletion code ORIGEN-S [Her84]. This code needs six data libraries containing decay data, photon yields, fission yields, cross sections, etc. The cross section data is given in three energy groups: a thermal group below 0.5 eV, an epithermal group between 0.5 eV and 1.0 MeV and a fast group above 1.0 MeV. In ORIGEN-S, these cross sections are collapsed to one-group values by use of three spectral input parameters. These parameters are called THERM, which is used to adjust the thermal cross sections to thermally averaged ones, RES, which is used to weight the epithermal cross sections relative to the thermal cross sections, and FAST, which is used for threshold reactions with energies above 1.0 MeV. If the thermal spectrum is Maxwellian distributed, THERM can be calculated according to:

$$\text{THERM} = \sqrt{\frac{\pi T_0}{4 T}} \quad (3.1)$$

where T is the Maxwellian spectrum temperature and T_0 is 293 K. THERM can also be calculated from the neutron spectrum if this is not Maxwellian

distributed:

$$\text{THERM} = \frac{\sum_{g=1}^n \phi_g / \sqrt{E_g}}{\sum_{g=1}^n \phi_g / \sqrt{E_{th}}} \quad (3.2)$$

where E_{th} is the thermal energy (0.025 eV), ϕ_g the neutron flux for energy group g and E_g the mean energy of that group (eV). The summations in both nominator and denominator are carried out over all thermal energy groups. The parameters RES and FAST can also be determined from the neutron spectrum, where RES is the ratio of the epithermal flux per unit lethargy and the thermal flux, and FAST is 1.45 times the ratio of the fast and thermal fluxes (the factor 1.45 is the reciprocal of the fraction of the neutron fission spectrum above 1.0 MeV).

Cell calculations are performed to determine the three spectral parameters. A 219-groups AMPX master library containing group cross sections averaged with a fission- $1/E$ -Maxwellian ($T=300$ K) spectrum is used [Cuc87], except for ^{59}Co , which was retrieved from the JEF1.1 library [JEF85] and processed by the NJOY87 code [Mac87]. Resonance shielding calculations for ^{235}U and ^{238}U are done by NITAWL-S [Wes81b] by application of the Nordheim integral method for a fuel temperature of 600 K (the mean moderator temperature, because resonance absorption takes mainly place in the outer region of the fuel lump). The cross sections of all other nuclides are infinitely diluted, which slightly overestimates resonance absorption in the cell. The cylindrical cell consisted of the fuel lumped into the central region, surrounded by the clad, moderator and construction materials like tubes and grids. The nuclide concentrations and cell volumes could be extracted from the benchmark description. Four cell calculations are performed by XSDRNPM-S [Gre83] in P_3S_8 mode and the values of THERM, RES and FAST are determined from the cell averaged fluxes. The parameters and results of each calculation are given in Table 3.1. The effective buckling height of 190 cm is found by setting the axial buckling with the effective height equal to the sum of the axial and radial buckling with the actual height and radius of the core. This means that the leakage with the effective height is equal to the leakage of a bare core with the actual height and radius.

The values of TERM, RES and FAST given in Table 3.1 for cell 1 to cell 3, are in disagreement with typical literature values for 33,000 MWd/tU

Table 3.1: Parameters and results of the three cell calculations. In cell 3, the effective height is decreased to reach criticality, while in cell 4 this is achieved by adding ^{10}B to the moderator.

	Cell 1	Cell 2	Cell 3	Cell 4
Eff. Height (cm)	190	190	33	190
Water Dens. ($\text{g}\cdot\text{cm}^{-3}$)	1.0	0.73	0.73	0.73
^{10}B present	no	no	no	yes
k_{eff}	1.32	1.30	1.00	1.00
THERM	0.96	0.90	0.90	0.83
RES	0.17	0.23	0.25	0.30
FAST	1.35	1.67	1.89	2.17

PWR fuel of 0.63, 0.33 and 2.00, respectively [Her84]. Although the values calculated here are "begin of cycle" values and not cycle averaged ones, these large discrepancies cannot be caused by the difference in burnup values only, because a value of THERM of 0.90 corresponds with a Maxwellian flux temperature of about 284 K (see Eq. (3.1)), which is in disagreement with the actual moderator temperature of about 580 K. The calculated spectrum is not Maxwellian distributed. The flux in the lowest energy group, extending from 10^{-5} to 10^{-2} eV, is higher than the corresponding Maxwellian flux of that group and the logarithmic mean energy of that group is very low, which gives a large contribution to THERM according to Eq. (3.2). If the upper boundary of the last group (10^{-2} eV) is taken for the characteristic energy of that group, a value of 0.67 is obtained for THERM (cell 3). A reason for the discrepancies found, might be that no $1/v$ absorber (e.g. ^{10}B) was present in the cell calculations to achieve criticality, which usually is present in a PWR core. Instead of such an absorber, the effective height was decreased in cell 3 to enfaavour leakage. However, the effect of leakage on the neutron spectrum is quite different from the effect of a $1/v$ absorber. Cell 2 (which has correct leakage) with ^{10}B added to the moderator such that criticality is achieved, gives a much harder spectrum. Values of THERM, RES and FAST are given for this case in Table 3.1 for cell 4. Again the last group gives a large contribution to THERM and if 10^{-2} eV is taken as the characteristic energy of that

group, a value of 0.64 is obtained.

Maybe better would be to use $1/\sqrt{E}$ values averaged with a Maxwellian spectrum ($T=580$ K) for all thermal groups instead of logarithmic mean energies. This leads to values for THERM of 0.68 (cell 3) and 0.65 (cell 4). This latter value is in good agreement with the actual moderator temperature, which would give a value of 0.63 for THERM (see Eq. 3.1).

In the ORIGEN-S calculations, a value of 0.63 is used for THERM. Because the values of the second till the fourth cell calculations were not available in time, the values of RES and FAST of the first cell calculation were used, despite the facts that the disagreements between these values and the literature values are rather large and that the spectrum of the fourth cell calculation seems to be more correct. Fortunately, the influence of these parameters on the nuclide concentrations calculated by ORIGEN-S is rather small.

The ^{59}Co concentration and the profile of the thermal neutron flux in zones above and below the fissile part of the fuel assemblies, both given in the benchmark description, could be used to calculate the ^{60}Co activation source in these zones. The dose rate contributions due to activation of ^{54}Fe and ^{58}Ni via (n,p) reactions turned out to be negligible compared with the above described ^{59}Co activation.

The shielding calculations are performed by the point-kernel shielding code MARMER. Geometry input for this problem is done by 116 bodies, which are combined to 36 input zones (zones of homogeneous composition). In total 21 different materials are defined: 6 for the fuel and 15 for the shield. The spatial dependence of the volumetric source density is given by 72 source systems. The axial dependence of the activation sources in zones above and below the fissile parts of the fuel assemblies, is taken proportional to the fast or thermal neutron fluxes in these zones (dependent on which activation reaction is taken into account). The axial dependence of the fission and activation sources in the fissile parts of the fuel assemblies, is equal to the burnup profile of the assemblies. Nuclide concentrations of fission products etc. are calculated by the ORIGEN-S code and written to a binary file. This file is subsequently read by MARMER and the nuclide concentrations are converted to source spectra by use of the MARMER nuclide library, containing half life times, decay energies and gamma yields for over 1000 nuclides. Both the Kitazume and Broder buildup factor formulae for multilayered shields were used (see Section 2.3), but the difference between these two methods appeared to be

very small. Because the gamma ray shielding of the transport cask is mainly determined by the 30 cm thick steel shield of the cask, different methods to account for multilayered shields are expected to give almost similar results.

3.4 Results

First, the influence of the values of THERM, RES and FAST on the source spectra in the shielding calculations is investigated by varying THERM from 0.63 to 0.96, RES from 0.17 to 0.34 and FAST from 1.35 to 2.70. The source spectrum changes no more than 25%, and for most energy groups, the change is far less than 10%. This is especially true for the source strength in energy group 3 (2.0 to 2.5 MeV), which is the main contributor to the dose rate along the cask, as will be shown, and which changes no more than 2%.

Calculated dose rates are shown in Fig. 3.2 for several distances from the outer side of the cask and for one azimuthal angle (in cylindrical coordinates with the axis of the cylinder equal to the axis of the cask). It is seen that at 7 cm from the outer side of the cask, the dose rate profile is rather peaked, which is mainly due to the smaller cask thickness at the top and bottom. With increasing distance from the outer side of the cask, the dose rate profile becomes flatter and at 200 cm from the cask, it is nearly flat along the cask.

Measured and calculated dose rates are compared with each other in Table 3.2 at several heights and distances from the cask. It is seen that the calculated dose rates agree with the measured ones within 20% at 7 cm from the cask, while at 100 and 200 cm from the cask, this agreement is even better. The dose rates shown in Table 3.2 are determined by energy group 3, extending from 2.0 to 2.5 MeV, for 75%, approximately. The source strength in this energy group is due to the nuclide ^{144}Pr with decay energy of 2.1857 MeV, for 93%, so this nuclide contributes to the dose rates shown in Table 3.2 for 70%, approximately. From this it is concluded that source spectrum calculations should be based on energy conservation instead of particle conservation, to decrease the influence of the decay of some dominating nuclides. The number of gamma rays with a particular energy is then changed to an effective number of gamma rays with energy equal to the mean energy of the energy group, such that the total energy emitted is conserved.

Calculated dose rates with and without the contribution of ^{59}Co activation in zones below (zone E) and above (zones A and C) the fissile part of the fuel

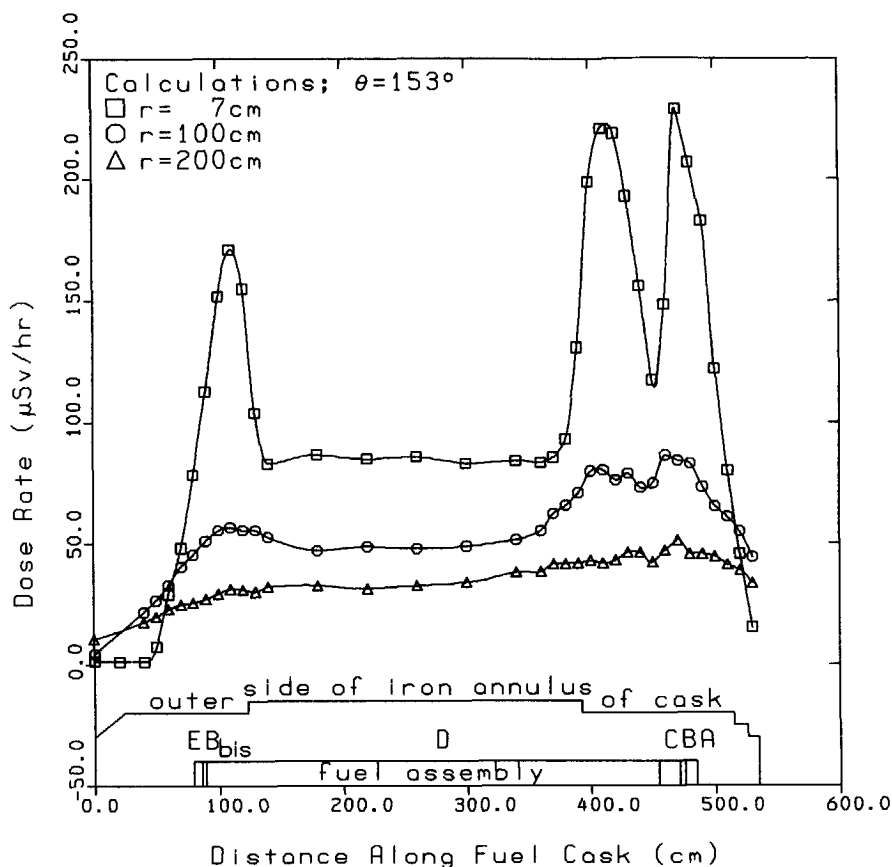


Figure 3.2: Calculated dose rates along the cask for several distances from the outer side of the cask.

assemblies, along the axial direction of the cask at a distance of 7 cm from the cask, are shown in Fig. 3.3. Here, it is seen that the calculated dose rates agree with the measured ones for heights up to 450 cm within 20%, and that the dose rate peaks at the top and bottom of the cask, at heights of 110 and 410 cm, are due to the smaller thickness of the cask at these heights. For heights above 450 cm the calculated dose rates overestimate the measured ones by a factor of 4, approximately. This is due to an overestimation of the ^{60}Co activation source in zones A and C, which can be seen from the fact that the calculated dose rates without this activation underestimate the measured ones for heights above 450 cm. This overestimation is due to three reasons:

Table 3.2: Measured and calculated dose rates for several heights along the cask (z) and several distances from the outer side of the cask (r). The standard deviations of the calculations due to the Monte Carlo process only are 5%, those of the measurements 8%.

r (cm)	z (cm)	Measured Dose Rates ($\mu\text{Sv/hr}$)	Calculated Dose Rates ($\mu\text{Sv/hr}$)	Contribution Group 3 (%)
7	118	162	164	71
100	108	54	59	67
7	272	97	84	82
100	272	49	48	81
200	272	33	33	76
7	416	248	226	71
100	402	80	81	69
200	405	42	40	75

- The ^{59}Co concentration given in the benchmark description is highly overestimated for two types of inconel and one steel grade [Blu82]. This gives an overestimation of the ^{60}Co activity in zone A by a factor of two and in zone C by a factor of three. The dose rate in point B in Fig. 3.3 is reduced to point B' if the correct ^{59}Co concentrations are used.
- The thermal value of the ^{59}Co absorption cross section is used to calculate the activation rate of ^{59}Co . It would have been better, however, to take a Maxwellian averaged cross section with a "neutron temperature" equal to the moderator temperature (≈ 600 K). The ^{59}Co absorption cross section is then reduced from 37 to 23 barn (see Eq. (3.1)), which gives a further reduction of the dose rate in point B from B' to B".
- The thermal neutron flux given in the benchmark description is overestimated because control rods and boron capture are not taken into account. This gives a further reduction of the dose rate in point B, which reduction is difficult to quantify, however.

The ^{60}Co activation source of zone E is rather small, so the difference between dose rates with and without activation at the bottom of the assemblies

(point A in Fig. 3.3) is also small. This difference is in fact even smaller if the concentration and cross section of ^{59}Co are also corrected in zone E.

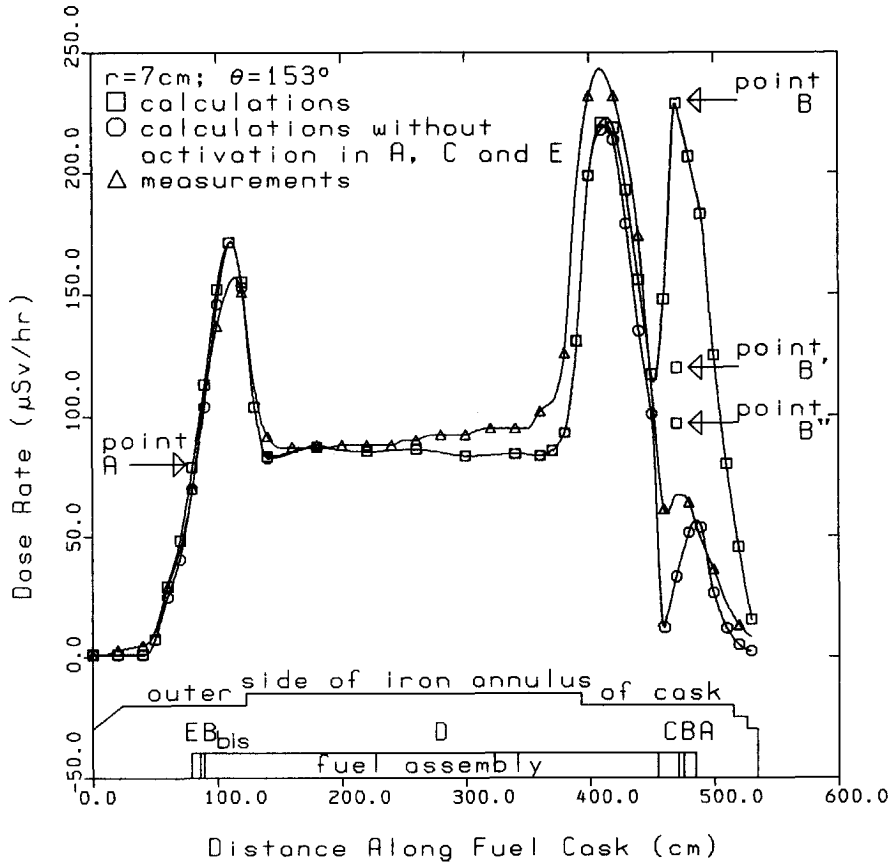


Figure 3.3: Measured and calculated dose rates along the cask at 7 cm from the outer side of the cask. The meaning of points A, B, B' and B'' is given in the text.

3.5 Conclusions

The source spectra used in the shielding calculations do not depend very much on the neutron spectrum during the irradiation of the fuel assemblies. This can be concluded from the fact that the source spectra are rather insensitive to the spectral input parameters of ORIGEN-S, named THERM, RES and FAST.

The calculated dose rates agree very well with the measured ones. At 7 cm from the outer side of the cask, agreement is within 20%, while at larger distances, the agreement is even better. The dose rate along the cask is determined by the fission products source for the major part, while the contribution of the ^{60}Co activation source is only important in the zones above the fissile part of the fuel assemblies. The contribution of the ^{60}Co activation source was highly overestimated in the calculations due to reasons given in Section 3.4.

In general it can be concluded that the fuel depletion code ORIGEN-S and the point-kernel shielding code MARMER are very well suited to this kind of shielding problems.

Chapter 4

Gamma Ray Buildup Factor Calculations for Iron by the Discrete Ordinates Code XSDRNPM-S¹

4.1 Introduction

Buildup factors are used by point-kernel shielding codes to account for the scattered radiation in the medium. Until a few years ago, data compiled in 1954 by Goldstein et al. [Gol54] was used. This data served as a reference for all calculations performed since then. The need for more accurate buildup factors, extended in both energy and shield thickness, lead to a new compilation of buildup factors [Tru88]. Air kerma and medium kerma buildup factors were calculated for several materials by Chilton et al. [Chi80] by use of a moments method code, while air kerma buildup factors for several materials were calculated by Takeuchi et al. [Tak85] by the discrete ordinates direct integration code PALLAS. Takeuchi compared buildup factors including bremsstrahlung with those without that contribution. Although both Chilton and Takeuchi used the same data library, the difference between the two results is 19% at a shield thickness of 40 mfp and energy of 0.5 MeV. In Fig. 4.1, the air kerma buildup factors for iron are given together with the results of Goldstein.

Both Chilton and Takeuchi calculated air kerma buildup factors, which are not equal to dose-equivalent buildup factors due to a slightly different detector response function. As explained in Section 2.3.7, air kerma is a measure of the photon energy transferred to kinetic energy of secondary particles in air, while dose-equivalent is a measure of the biological damage created in tissue by the incident radiation [Chi84]. Shure [Shu79] compared air kerma buildup factors with dose-equivalent buildup factors. The discrete ordinates code ANISN was

¹This chapter is an adapted version of [Klo92]

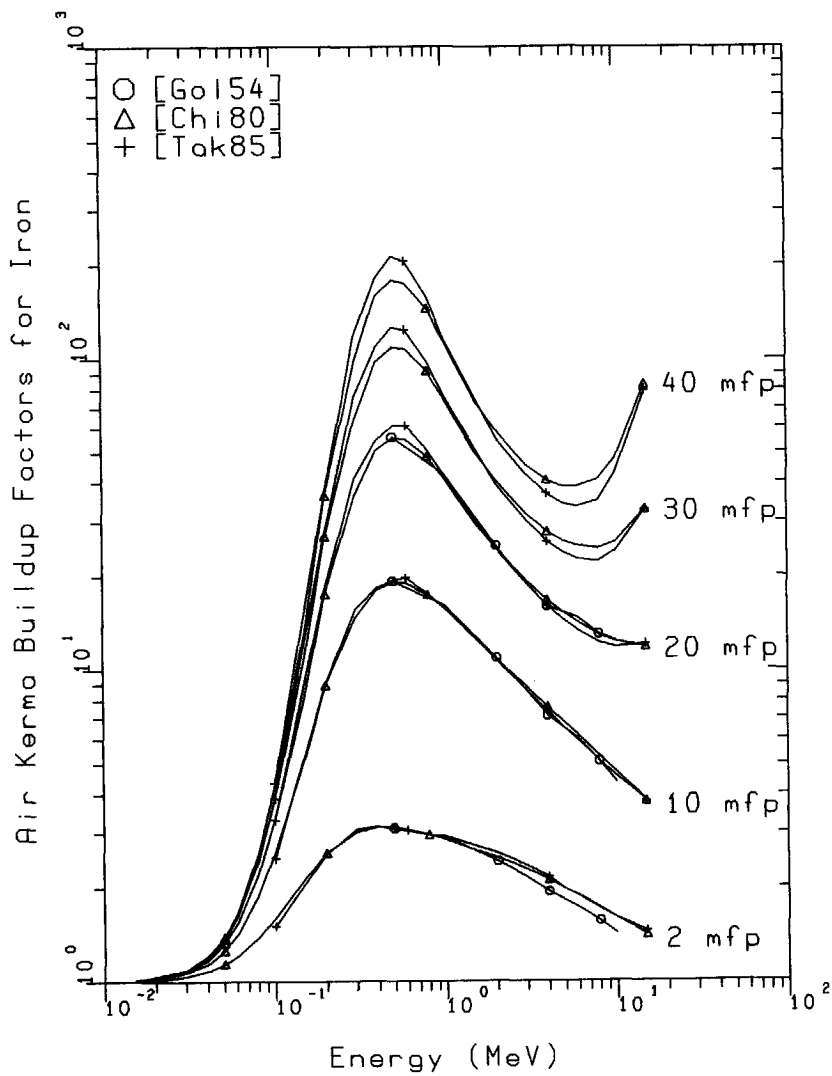


Figure 4.1: Air kerma buildup factors for iron from literature.

used for this purpose with 57 energy groups, P_3 cross section representation and a P_{19} angular quadrature set (this set is probably a Gauss Legendre quadrature set of order 19, thus having 20 angular cones [Alc86]). The dose-equivalent buildup factors for iron were found to be larger than air kerma buildup factors for a wide range of energies. However, the difference was less than 13%, while the difference between the air kerma buildup factors for iron and the Goldstein compilation reached nearly 30% at a shield thickness of only 20 mfp.

Although not mentioned by Shure, the use of discrete ordinates codes for gamma ray buildup factor calculations gives rise to serious problems, which can appear in other gamma ray deep penetration calculations as well. The aim of this study is to calculate air kerma buildup factors for iron by the discrete ordinates code XSDRNPM-S [Gre83] and to compare the results with literature values. Special attention will be drawn to difficulties, which appear when using discrete ordinates codes for gamma ray deep penetration calculations.

4.2 Cross Section Library Preparation

The VITAMIN-C library [Rou79] together with customized libraries are used. The latter ones are based on the JEF1.1 file [JEF85], while the Compton scattering cross section is based on the Klein-Nishina equation [Chi84]. The angle dependence of the scattering cross sections is developed into a Legendre series:

$$\Sigma_s(\varepsilon, \varepsilon', \mu_s) = \frac{1}{2} \sum_{\ell=0}^L \Sigma_{s\ell}(\varepsilon, \varepsilon') P_{\ell}(\mu_s) \quad (4.1)$$

where $\Sigma_{s\ell}(\varepsilon, \varepsilon')$ is the Legendre expansion coefficient of order ℓ for scattering from "rest mass energy" $\varepsilon = E(\text{MeV})/0.511$ to $\varepsilon' = E'(\text{MeV})/0.511$ and μ_s is the cosine of the scattering angle. The scattering cross section can be written according to the Klein-Nishina equation:

$$\begin{aligned} \Sigma_s(\varepsilon, \varepsilon', \mu_s) = \\ = ZN\pi r_e^2 \left(\frac{1}{\varepsilon}\right)^2 \left(\frac{\varepsilon'}{\varepsilon} + \frac{\varepsilon}{\varepsilon'} + \left(\frac{1}{\varepsilon'} - \frac{1}{\varepsilon}\right)\left(\frac{1}{\varepsilon'} - \frac{1}{\varepsilon} - 2\right)\right) \delta\left(1 + \frac{1}{\varepsilon} - \frac{1}{\varepsilon'} - \mu_s\right) \end{aligned} \quad (4.2)$$

where Z and N are the atomic number and atomic density of the nuclide under consideration, respectively, and r_e is the classical radius of the electron

($2.818 \cdot 10^{-13}$ cm). The Legendre expansion coefficients are integrated over energy for groups g and g' to obtain Legendre coefficients for the scattering matrix:

$$\begin{aligned} \Sigma_{st}^{g \rightarrow g'} &= \frac{\int_{\epsilon \in g} \phi(\epsilon) \int_{\epsilon' \in g'} \Sigma_{st}(\epsilon, \epsilon') d\epsilon' d\epsilon}{\int_{\epsilon \in g} \phi(\epsilon) d\epsilon} = \\ &= \frac{\int_{\epsilon \in g} \phi(\epsilon) \int_{\epsilon' \in g' - 1}^1 (2\ell + 1) \Sigma_s(\epsilon, \epsilon', \mu_s) P_\ell(\mu_s) d\mu_s d\epsilon' d\epsilon}{\int_{\epsilon \in g} \phi(\epsilon) d\epsilon} \end{aligned} \quad (4.3)$$

The flux $\phi(\epsilon)$ is used as a weighting function here, but because it is generally unknown, a flat flux approximation is used. The integration over energy group g' is performed analytically, over g numerically. However, the numerical integration over group g for high Legendre orders ($\ell \geq 8$) fails for low energies. Substituting Eq. (4.2) in Eq. (4.3) and performing the integrations over μ_s and ϵ' leads to a polynomial in $1/\epsilon'$ and $1/\epsilon$ of maximum orders $\ell + 1$ and $\ell + 4$, respectively. This polynomial is to be numerically integrated over ϵ , where the limits of ϵ' depend for some groups on ϵ because of the limited energy decrement per collision. For low energies both ϵ and ϵ' are small and the integration fails because the argument of the ϵ integral is the difference of two very large numbers (for $\ell = 8$ and $E \leq 0.05$ MeV of the order of 10^{14} , while the difference is less than 10^{-2}), which becomes meaningless because of limited computer accuracy. Fortunately, the higher order Legendre terms for low energies are unimportant and can be set to zero, to solve this problem. A similar problem is expected to appear for very high energies and very high Legendre orders, where the argument of the ϵ integral is the difference of two small numbers. However, for the maximum Legendre order ($\ell=9$) and maximum energy (15 MeV) used by the author, no problems arose.

The total scattering matrix is the sum of the Compton scattering matrix and the pair production cross section multiplied by 2 (because of two annihilation photons). The cross sections are integrated over energy to obtain group averaged cross sections. The total cross section of a group consists of the sum of the photoelectric, Compton scattering and pair production cross section, where the Compton cross section is calculated according to the Klein-Nishina equation to make the total scattering cross section consistent with the scattering matrix.

Two assumption are made in the customized libraries as described above. Flat weighting is performed for the cross section data. Except the fact that the introduced error becomes less for smaller energy groups, one can hardly predict what and how great the influence on the calculated spectrum will be. Furthermore, it is assumed that the Klein-Nishina equation adequately describes the Compton scattering process. This is certainly true for high gamma energies where the electrons in the iron can be considered as free. For low energies, the Klein-Nishina equation gives an overestimation of the Compton scattering cross section because of the neglect of electron binding effects. The influence of this is probably very small for two reasons. If electron binding effects are taken into account, the coherent scattering cross section should be included as well, which tend to cancel the electron binding effects and, as these effects become important, the photoelectric cross section will usually be larger than the Compton scattering cross section by several orders of magnitude.

4.3 Buildup Factor Calculations

Buildup factors for an isotropic point source in an infinite medium are calculated from flux spectra calculated by the one-dimensional discrete ordinates code XSDRNPM-S in spherical geometry. The calculational method of the XSDRNPM-S code in spherical geometry is outlined in Appendix A. The buildup factors are defined as the ratio of the detector response due to both scattered and unscattered radiation, and the detector response due to unscattered radiation only:

$$B(r, E_0) = \frac{\int_0^{\infty} \phi(r, E)R(E)dE}{\phi_0(r)R(E_0)} \quad (4.4)$$

where ϕ_0 is the unscattered flux, and B is the buildup factor for detector response R , energy E_0 and shield thickness r .

Because the spectrum is calculated in groups, the numerator of Eq. (4.4) can be approximated by:

$$\int_0^{\infty} \phi(r, E)R(E)dE = \sum_{g=1}^{G_{max}} \phi_g(r)R_g \quad (4.5)$$

where ϕ_g and R_g are the group flux and the group averaged detector response for group g , respectively, and G_{max} is the highest energy group number corresponding with lowest energy.

The denominator of Eq. (4.4) can be calculated in two different ways. The first method is similar to the point-kernel approach for unscattered radiation:

$$\phi_0(r)R(E_0) = \frac{1}{4\pi r^2} \exp(-\Sigma_t^G r) S_G R_G \quad (4.6)$$

where S_G is the source strength and Σ_t^G is the group averaged interaction coefficient of the medium for the source energy group G . The second method is similar to Eq. (4.5):

$$\phi_0(r)R(E_0) = \phi_G(r)R_G \quad (4.7)$$

The unscattered response here is overestimated because of the inclusion of in-group scattering in the source energy group. For small energy groups and a well converged calculation, the two methods are expected to give the same results, because both methods converge to a point energy calculation. The second method can therefore be seen as a check on the convergence of the calculation.

The air kerma response function is calculated by assuming that a pair production and Compton scattering are partially absorbing, while the photoelectric effect is totally absorbing. The fraction of the photon energy absorbed in a Compton scattering is calculated according to Eq. (2.29), while the fraction of the photon energy absorbed in a pair production is calculated according to Eq. (2.30). The detector response function thus obtained is very much like the one obtained when using energy absorption cross sections from [Tru88]. The air kerma response function is often used to calculate exposure rates. This is only correct, however, if bremsstrahlung production is negligible (see Section 2.3.7). For high energies ($E \geq 5$ MeV) and high Z numbers, this assumption is poor, and the exposure buildup factors are underestimated by the air kerma buildup factors [Tak85].

4.4 Calculations

Calculations were done by the discrete ordinates code XSDRNPM-S, by using the default angular quadrature based on a Gauss double Legendre set. An

S_N calculation then has N different directions with non-zero weights and one backwardly directed angle with zero weight (needed for angular redistribution, see Appendix A).

P_5S_{48} calculations in 36 energy groups using the VITAMIN-C library were performed. The source with a thickness of 0.01 mfp of the source energy group, is divided into 3 intervals, while the shield from 0.05 up to 35.05 mfp is divided into 350 intervals. Buildup factors were calculated up to 30 mfp, which means that an extra shield layer of 5.05 mfp is used to simulate an infinite medium. This is sufficient because the flux at 3 mfp from the outer boundary of the sphere is changed by less than 0.4% if that boundary condition is changed from vacuum to reflected. Results for the air kerma buildup factors for methods 1 and 2 (Eqs. (4.6) and (4.7), respectively) are given in Fig. 4.2 for 2 and 30 mfp, and for over 30 source energy groups. It is seen that the discrepancies between calculated buildup factors and literature results are very large.

A customized library in the VITAMIN-C energy group structure was produced according to Eqs. (4.1), (4.2) and (4.3) with a P_7 Legendre series expansion. Calculations in P_7S_{48} mode were performed to calculate the buildup factors with this library. The results for both methods are very similar to Fig. 4.2. Again large discrepancies are found between the calculated results and literature results.

A library with 214 energy groups and P_7 Legendre order expansion is made according to Eqs. (4.1), (4.2) and (4.3). The energy group structure is as follows: 0.4 MeV intervals between 14.8 and 6.0 MeV, 0.2 MeV between 6.0 and 1.0 MeV, 0.02 MeV between 1.0 and 0.2 MeV, 0.01 between 0.2 and 0.1 MeV, 0.001 MeV between 0.1 and 0.01 MeV. In addition 25 source energy groups are chosen with very small widths (e.g. 0.002 MeV at 15 MeV), so that the Σ_t^G values in Eq. (4.6) are equal to the point energy values. The shield is divided into 450 intervals from 0.05 to 45.05 mfp and the buildup factors were calculated up to 40 mfp. The air kerma buildup factors are given in Fig. 4.3 for methods 1 and 2, and for 25 source energy groups. As can be seen, method 1 gives a slight underestimation compared with literature values, while method 2 gives a slight overestimation. In general, the results are much better than in the previous case with only 36 energy groups, but the discrepancies at the high energy tail ($E \geq 5$ MeV) are still rather large for shield depths of 20 mfp and up.

To find the reason for the discrepancies at the high energy tail, a 214 groups

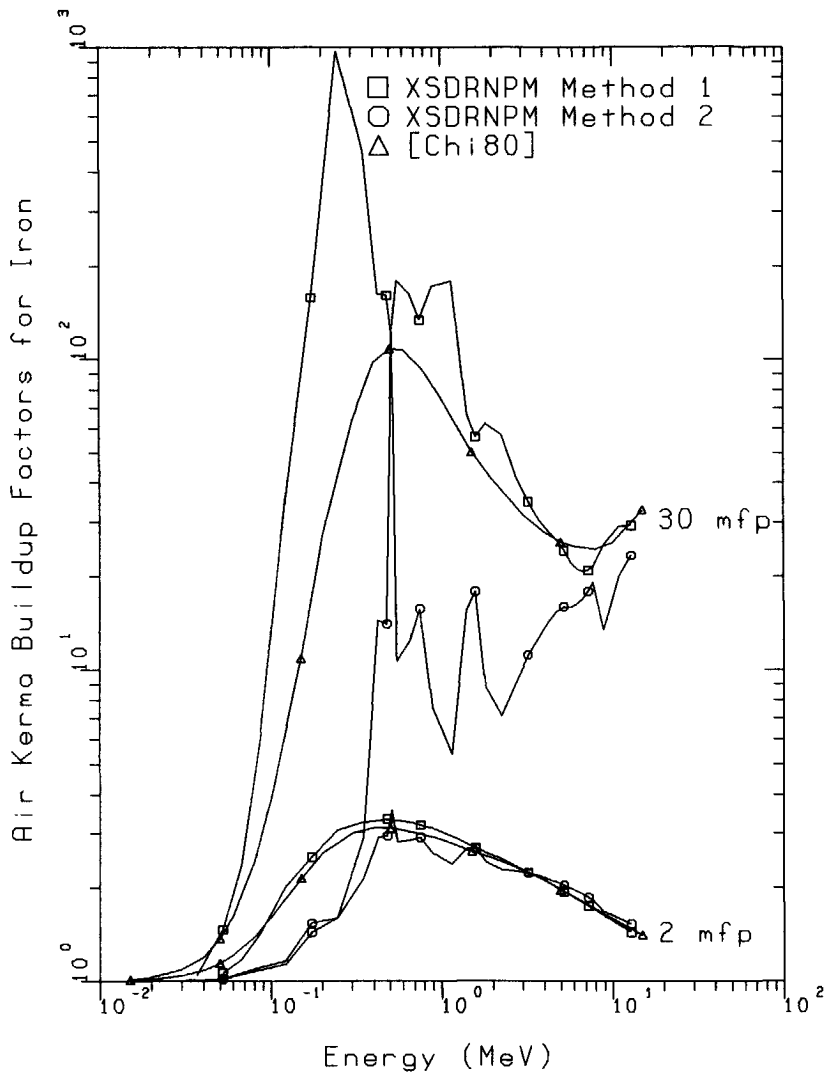


Figure 4.2: Air kerma buildup factors for iron calculated according to methods 1 and 2 in P5S48 mode using the VITAMIN-C library, compared with literature.

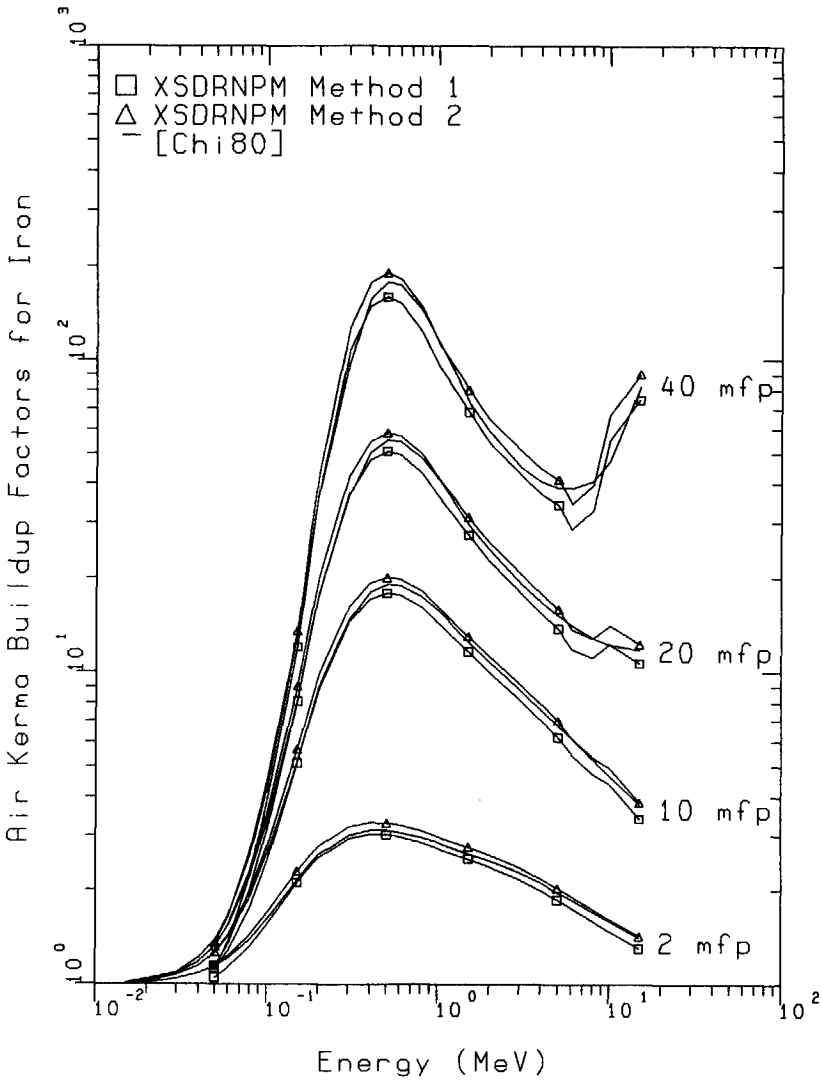


Figure 4.3: Air kerma buildup factors for iron calculated according to methods 1 and 2 in P7S48 mode using a 214 groups library, compared with literature.

P_9 library was made, with the same energy structure as the previous library, but with the Legendre expansion order increased from 7 to 9. It turned out, however, that this change has only a very minor effect: the air kerma buildup factor at 10.0 MeV and 40.0 mfp (method 1) changed only from 55.6 to 57.5.

A 211 groups P_7 library with a finer energy structure in the high energy region was made to check whether the discrepancies are still due to a too coarse energy mesh. The energy mesh intervals are 0.2 MeV between 15.0 and 4.0 MeV, 0.1 MeV between 4.0 and 1.5 MeV, 0.025 MeV between 1.5 and 0.4 MeV, 0.01 MeV between 0.4 and 0.15 MeV and 0.0025 MeV between 0.15 and 0.04 MeV. Because the lower energy boundary (0.04 MeV) is higher than that in the 214 groups library (0.01 MeV), the number of energy groups is somewhat reduced, despite the finer energy mesh. This was necessary because of the limited disk scratch space (60 Mbyte), which restricted the number of space and angular mesh intervals and energy groups. The influence on the buildup factors turned out to be negligible, however. The air kerma buildup factor at 10.0 MeV and at 40.0 mfp (method 1) changed only from 55.6 to 55.5.

Table 4.1: Air kerma buildup factors for iron for $E = 10.0$ MeV and $\mu x = 10.0$ mfp, calculated with different energy group structures and mesh intervals. The literature values are 4.69 [Chi80] and 4.54 [Tak85]. The maximum energy mesh and cutoff energy are given in MeV.

Max. ΔE	Cutoff Energy	No. of Groups	Ang. Quad.	Leg. Exp.	Mesh (mfp)	Method 1	Method 2
0.4	0.01	214	48	7	0.100	4.410	4.971
0.4	0.01	214	48	9	0.100	4.489	5.060
0.2	0.04	211	48	7	0.100	4.410	4.965
0.4	0.06	158	48	7	0.100	4.410	4.971
0.4	0.06	158	48	7	0.050	4.683	4.904
0.4	0.06	158	48	7	0.025	4.783	4.883
0.4	0.06	158	60	7	0.100	4.483	4.959
0.4	0.06	158	72	7	0.100	4.532	4.953
0.4	0.06	158	72	9	0.100	4.529	4.950
0.4	0.06	158	72	9	0.025	4.819	4.877

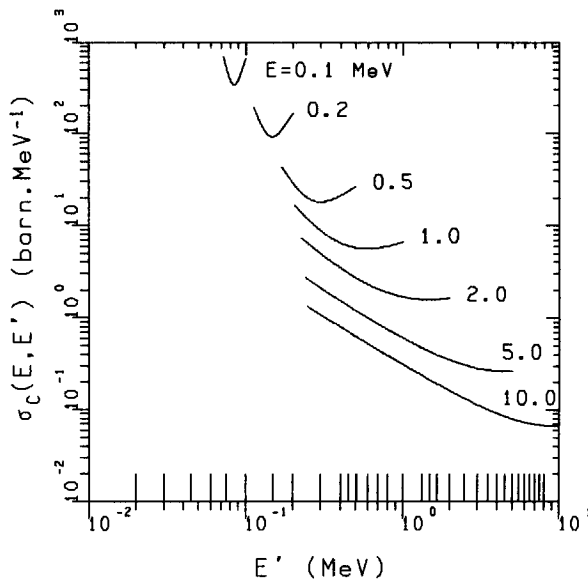


Figure 4.4: Differential angular integrated Klein-Nishina scattering cross section $\sigma_C(E, E')$ for iron as a function of outgoing energy E' for several incident energies E . The VITAMIN-C energy group structure is given along the E' axis.

Two 158 groups libraries with P_7 and P_9 Legendre order expansion are made with the same energy structure as the 214 groups library described earlier, but with a lower cutoff energy of 0.06 MeV instead of 0.01 MeV. This, together with a reduction of the shield thickness, enabled us to calculate with much smaller mesh intervals without exceeding the available disk scratch space. From the earlier calculations it was found that the contribution to buildup factors at 10.0 MeV due to the energy region below 0.06 MeV is negligible. Some results of these calculations, compared with results from previous calculations are given in Table 4.1.

4.5 Discussion

From Fig. 4.2 it is seen that the VITAMIN-C gamma data library is not very suited to buildup factor calculations (and to anisotropic gamma ray deep penetration calculations in general). Because of the broad energy group structure,

the fluxes in the source energy groups are by far not equal to the unscattered fluxes, which leads to quite large differences between methods 1 and 2. There are two reasons why the energy group structure should be much finer. Because cross section weighting is done by a flat flux approximation (see Eqs. (2.27) and (4.3)), the cross sections become more accurate as the energy group widths decrease. Secondly, because of the limited energy decrement per collision, a gamma ray upon collision can only scatter to a limited number of energy groups. To represent gamma ray downscattering accurately, the number of energy groups should be sufficiently large, thus leading to the condition that the energy group width should be much smaller than the maximum energy decrement per collision. In Fig. 4.4, the differential angular integrated Klein-Nishina scattering cross section is given for several energies, together with the VITAMIN-C energy group structure. As can be seen, the scattering cross section for low energies has only a non-zero value for a small energy range and the VITAMIN-C group structure does not fulfil above mentioned condition for energies below 0.5 MeV (at 0.45 MeV, a gamma ray can only scatter to 4 groups, at 0.2 MeV only to 2 groups and below 0.1 MeV only to 1 group). Downscattering (and thus absorption in low energy groups) is underestimated and buildup factors according to method 1 give an overestimation, while those according to method 2 give an underestimation. Both discrepancies are due to the reason that the fluxes in the source energy group and nearby groups are overestimated.

The 214 groups library does fulfil above mentioned conditions on the energy group structure. In Fig. 4.3, the buildup factors according to the two methods are shown together with literature values. This figure is only meant to see the qualitative differences between the results of the two methods. As can be seen, method 1 gives a slight underestimation, while method 2 gives a slight overestimation of buildup factors, compared with literature values. Above 5 MeV, the discrepancies become serious and neither a Legendre expansion increase from P_7 to P_9 , nor a finer energy mesh give better results.

In Fig. 4.5, a polar diagram of the angular Klein-Nishina scattering cross section $\sigma_C(E, \mu_s)$ is given. For high energies, the cross section is highly forwardly peaked, and it is unlikely that a P_7 Legendre expansion is sufficient to represent the angle dependence of the scattering cross section accurately. In fact, it is not as can be seen in Fig. 4.6, which gives the angular Klein-Nishina scattering cross section and the P_7 and P_9 expansions (Eq. (4.1) integrated

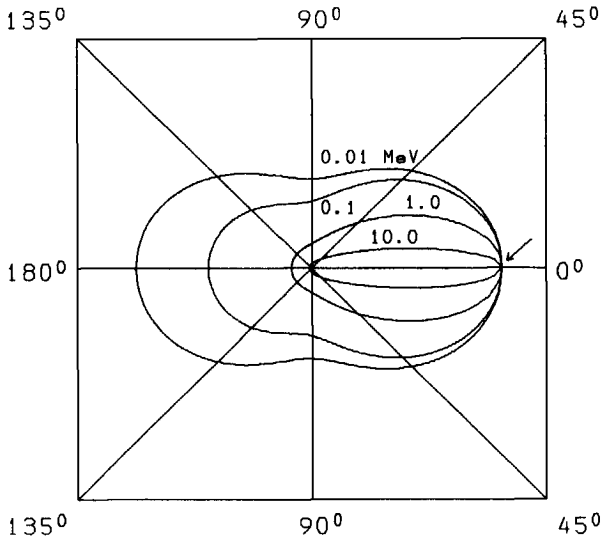


Figure 4.5: Polar diagram of the differential energy integrated Klein-Nishina scattering cross section $\sigma_C(E, \mu_s)$ for iron for several incident energies. The cross section value at 0° (the arrow in the figure) is 12.97 barn.

over ϵ') as a function of the incident energy. It can be seen that both the P_7 and P_9 cross section representations are poor for forwardly directed scattering angles ($\mu \geq 0.9$) compared with the exact Klein-Nishina cross section. Despite the fact that the P_9 representation is already much better than the P_7 , still large defects are present for scattering cosines larger than 0.95, which can lead to errors because the scattering cross section is highest at these angles.

Because the scattering angle depends on the energy decrement per collision, the angular mesh cannot be chosen independently from the energy group boundaries. Angular redistribution [Mik77] requires a fine angular mesh, dependent on the energy group widths. This means that a particle scattering from one group to another, must be able to scatter from one angle to another as well. For the 214 group structure as mentioned above, this requires an extremely fine angular mesh, which can hardly be realized in practice. In fact, even the S_{72} quadrature set does not meet these requirements.

Probably the energy widths in the high energy region can be chosen somewhat larger than in the 214 and 158 groups libraries, because the maximum energy decrement per scattering is very large above 5 MeV. The pair pro-

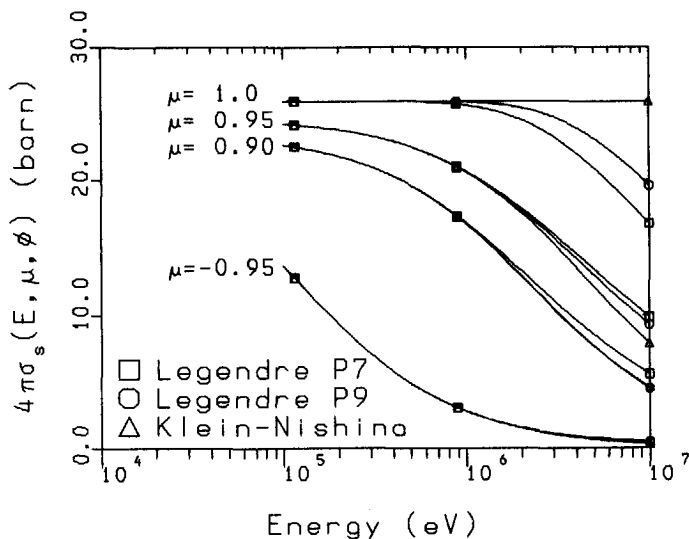


Figure 4.6: Angular scattering cross sections for iron as a function of incident energy for several scattering angles.

duction cross section, however, is highly dependent on energy in this region, which limits the width of the energy groups. Note that the use of the 211 groups library, with finer energy groups at the high energy tail, makes the angular redistribution requirement even more severe. No better results have to be expected therefore by using this library.

From Table 4.1 it is seen that a finer spatial mesh has a large influence on the calculated buildup factors. Especially near the source, the $1/r^2$ dependence requires an extremely fine mesh in order to describe this behaviour accurately. It can be seen that for a mesh width of 0.025 mfp, the buildup factors according to methods 1 and 2 are almost equal to each other, which implies that the source energy group flux is a good representation of the uncollided flux.

At this moment, it is not quite clear how the above mentioned arguments can explain the calculated buildup factor behaviour as a function of energy above 5 MeV (see Fig. 4.3), and only a tentative explanation will be given. As the energy increases above 5 MeV, the Compton cross section becomes more and more forwardly peaked, which is not correctly represented by a truncated Legendre expansion. The underestimation of the forwardly directed scattering cross section leads to an underestimation of buildup factors at high penetra-

tion depths. At 10 MeV, the Compton scattering cross section is extremely forwardly peaked, but also severely underestimated by a Legendre expansion. But due to a too coarse angular mesh, particles that do scatter are not redistributed to other angles, which probably leads to an overestimation of the flux in the most forwardly directed angle(s). Furthermore, the influence of pair production becomes important (the pair production cross section at 10 MeV is about as large as the Compton scattering cross section), whose contribution is correctly calculated, which may lead to more correct buildup factors.

It must be emphasized that all changes in the energy group structure, Legendre expansion order, angular mesh and spatial mesh have an effect on the buildup factor at 10.0 MeV and 10 mfp of 10% only. However, changes which have only a weak effect at 10 mfp, may have a large effect at deep penetration distances. Deep penetration calculations are expected to be sensitive to cross section values because of the exponential attenuation, which requires small energy groups (although buildup factors are found to be relatively insensitive to cross sections [Chi80]). A correct angular mesh, however, which meets the angular redistribution requirements, is important as well at large shield thicknesses, thus leading to the condition of broad energy groups or an extremely fine angular mesh.

A fine energy group structure and fine spatial and angular meshes not only lead to long CPU times. If computer memory is too small, cross section data, flux moments, etc. will be stored externally (e.g. on disk), which delays the execution of the program enormously because of slow communication with that external device and page swapping in memory. In fact, limitations on all calculations described in this paper are imposed by restrictions on the total disk scratch space of 60 Mbytes. The CPU time on a VAX3100 M30 workstation for a $P_{9S_{48}}$ job with 214 energy groups and 454 spatial intervals, with the source in group 15, is about 14 hours, while the elapsed time is about 90 hours.

4.6 Conclusions

Buildup factors below 5 MeV are in agreement with literature values [Chi80] within 10%, approximately. This is reasonable for such large shield thicknesses, because differences between mutual literature values are of the same size (see Fig. 4.1).

To calculate buildup factors with a discrete ordinates code like XSDRNPM-S, many energy groups and extremely fine space and angular meshes are needed, to get accurate results at large shield thicknesses and high energies. It is shown that a space mesh of 0.10 mfp and an angular quadrature of S_{48} is not sufficient. Much accuracy can be gained by reducing the space mesh intervals to values below 0.025 mfp near the source. This is even necessary for energies where the cross section is rather flat as a function of energy (e.g. at 10.0 MeV). Because it can be expected that the flux in low energy groups is much more isotropically distributed than the flux in the source energy group, improvements with respect to CPU time can possibly be achieved by using energy group dependent quadrature sets, such that the quadrature order for the source energy group and nearby groups is higher than the quadrature order for low energy groups. Another improvement may be to use biased quadrature sets for the source energy group and nearby groups [Alc86]. Furthermore, it is noted that for point, plane or line sources in an infinite medium, moments method codes, as used in literature to calculate buildup factors [Gol54, Chi80], perform better. However, such codes are not generally applicable to shielding problems because of geometrical restrictions.

Chapter 5

Simple Streaming Methods

5.1 Introduction

In the early years of shielding calculations, neutron and gamma ray streaming through ducts was simply described by the line-of-sight component of the radiation, for which formulae can be found in literature [Pri57, Sch73, Chi84]. Simple albedo concepts were introduced to account for reflections against walls of the duct for both neutrons [Sim56] and gamma rays [LeD59], for straight and multibent ducts. Unfortunately, accurate albedo data was lacking at that time.

Gamma ray streaming in two-legged ducts can also be described reasonably well (within a factor of two) by the single scattering method [Num88, Yam88], but neutron streaming cannot so easily be calculated by simple methods, and much attention has been given to find approximate formulae. Miura derived empirical formulae for the neutron flux distribution in annular [Miu83] and cylindrical ducts [Miu89]. Shin [Shi89] derived a general formula which is applicable to several geometries and sources. When applying these methods, however, the strength, spectrum and angular distribution of the source has to be known in advance, which requires sophisticated transport calculations. Furthermore, the albedo values used in simple methods are often corrected by an experimentally derived factor, which is difficult to generalize to other geometries and energy regions.

The other way to solve streaming problems is to use rigorous transport codes. Although these codes cannot be used at a first design stage because of their long CPU times, they are attractive for special streaming geometries like irradiation tubes of research reactors and cavity streaming through the annulus around the reactor pressure vessel [Tra78, Bar88]. However, the performance of transport codes in such circumstances is not straightforward. Two-dimensional discrete ordinate codes, for example, fail in annular ducts of small width [Miu81, Oka86]. Three-dimensional discrete ordinates codes

perform better, but require longer CPU times [Bar91]. For all problems holds that only a simplified or restricted geometry can be modelled.

The Monte Carlo method also requires rather long CPU times. Albedo Monte Carlo codes are generally more effective but very large data files containing differential albedo data are necessary, which are only available for a limited number of materials. It is also difficult to prepare correct albedo data because of their dependence on curvature, while albedo values for slabs are found to give an overestimation in cylindrical ducts and an underestimation in annular ducts [Shi82, Shi84]. The reemitting area must also be much smaller than the duct dimensions.

Streaming problems are usually divided into subproblems to calculate the strength, spectrum and angular distribution of the source separately from the streaming calculations. The final solution is then obtained by bootstrapping codes, e.g. using the DOT-DOMINO-MORSE [Tra78, Bar88] and DOT-DOTTOR-TORT sequence [Chi88]. In these cases, a two-dimensional discrete ordinates code (DOT) is used to calculate the angular flow rate at the outer side of a reactor vessel, for example. A conversion program (DOMINO or DOTTOR) is then used to convert these angular flow rates to a source term for the three-dimensional shielding calculations, which are done by a Monte Carlo code (MORSE) or a discrete ordinates code (TORT). To judge the capabilities of transport codes in real streaming problems (steel-walled ducts in concrete, irradiated by a typical reactor spectrum), experiments were performed, which are described in Chapter 6. In Chapter 7, rigorous calculations are described and the calculational results are compared with the measurements.

This chapter deals mainly with simple formulae to calculate the flux at the exit of a duct. Handformulae to calculate the line-of-sight component of the flux are described in Section 5.2, and the model of Shin to calculate the albedo component is exposed in Section 5.3. A program IRIDUCT is described in Section 5.4, which combines these methods to calculate the total flux at the exit of a cylindrical, rectangular or annular duct.

5.2 Line-of-Sight Component

Besides the strength of the source at the duct entrance, one has to know the angular description and the spectrum of the source as well. These qualities are of course known if transport codes are used for the source calculation,

but these codes consume too much CPU time to use at a first design stage. Simpler methods give the source strength and spectrum at the duct entrance, but no information about the angular distribution. Therefore, the angular dependence is supposed to be azimuthally symmetric around the duct axis. The dependence of the source on the polar angle is then described as a power of the cosine of this angle [Chi84, Klo89a]:

$$j_n(\mathbf{r}_s, \Omega) = (\mathbf{n} \cdot \Omega) \phi(\mathbf{r}_s, \Omega) = \frac{(p+1)\mu^p}{2\pi} j_n(\mathbf{r}_s) \quad (5.1)$$

where \mathbf{r}_s is a coordinate on the source plane, \mathbf{n} is the normal to the source plane, μ is the cosine of the polar angle with respect to this normal ($\mu = \mathbf{n} \cdot \Omega$) and $j_n(\mathbf{r}_s, \Omega)d\Omega$ is the total number of particles per unit source plane area in $d\Omega$ around Ω . The integration of the angular flow rate over the azimuthal angle from 0 to 2π and over the cosine of the polar angle from 0 to 1 gives the total flow rate $j_n(\mathbf{r}_s)$. The power p will be energy dependent since the fast flux will be more forwardly peaked than the thermal flux. Determination of p for some practical situations is discussed later.

The flux at the duct exit can be determined from the angular flow rate at the duct entrance. If no attenuating material is present in the duct, one can write for the line-of-sight flux at the duct exit:

$$\phi(\mathbf{r}_d) = \int_{A_s} \frac{j_n(\mathbf{r}_s, \Omega)}{|\mathbf{r}_s - \mathbf{r}_d|^2} dA \quad (5.2)$$

where \mathbf{r}_d is the detector coordinate at the duct exit and A_s is that part of the source plane area, visible from the duct exit. For cylindrical ducts with \mathbf{r}_d on the duct axis, Eq. (5.2) becomes:

$$\phi(\mathbf{r}_d) = \frac{p+1}{p} j_n(\mathbf{r}_s) \left(1 - \frac{1}{\left(1 + \left(\frac{a}{L}\right)^2\right)^{p/2}} \right) \approx \frac{p+1}{2} j_n(\mathbf{r}_s) \left(\frac{a}{L}\right)^2 \quad (5.3)$$

where a and L are the radius and length of the duct, respectively. The approximation is valid for $a \ll L$. For annular gaps, Eq. (5.2) becomes:

$$\phi(\mathbf{r}_d) \approx \frac{p+1}{2\pi} \frac{j_n(\mathbf{r}_s) A_s}{L^2} \quad (5.4)$$

It is assumed here that the gap length is much larger than the width of the gap, which is the difference of the outer and inner radius of the gap. This leads in general to an overestimation of the flux. For the visible area A_s , holds:

$$A_s = (a_o^2 - a_i^2) \arccos\left(\frac{a_i}{r_d}\right) + a_o^2 \arccos\left(\frac{a_i}{a_o}\right) - a_i \sqrt{a_o^2 - a_i^2} \quad (5.5)$$

where a_i is the inner radius, a_o the outer radius and r_d a position at the gap exit between a_i and a_o . It can be seen from Eq. (5.5) that the visible area increases, if r_d is moved from the inner radius to the outer radius. The mean value of A_s is exactly two times the visible area for $r_d = a_i$ and the visible area for r_d in the middle of the gap is approximately equal to this mean area. Thus to calculate the mean flux at the gap exit, one only has to calculate the flux in the middle of the gap at $r_d = (a_i + a_o)/2$. For a rectangular gap, one cannot integrate Eq. (5.2) analytically, but if the height and width of the gap are nearly equal to each other, it is very unlikely that the answer will be very different from a cylindrical duct with equal visible source area.

The above formulae for cylindrical ducts become somewhat more complicated if the duct is filled with attenuating material, but the recipe to derive these formulae is the same [Chi84, Sch73]. For annular and rectangular gaps filled with attenuating formulae, no simple equations can be derived, but a point-kernel code like MARMER [Klo90a] can be used to calculate the line-of-sight flux in such a case. Point-kernel codes can also be used to calculate the wall penetrating flux [Klo89a] at the end of the duct. In this case one has to define a disk source at the duct entrance. The source can be defined as in Eq. (5.1).

The power p of the source angular distribution in Eq. (5.1) has to be derived yet. It is difficult to derive expressions, which are generally applicable. Here, a derivation will be presented, which is valid if the duct entrance is close to the reactor core. The situation is shown in Fig. 5.1. A reactor core surrounded by a reflector acts as the source. It is supposed that the volumetric source strength of the core increases linearly with the distance in the core measured from the core-reflector boundary. This is roughly valid for the first few mean free paths for fast neutrons if the fission distribution is cosine shaped. The number of uncollided particles at P in $d\Omega_d$ around Ω is:

$$\int_0^{\infty} S_v(x, \Omega) \exp\left(-\frac{\Sigma_{tc}x + \Sigma_{tr}d}{\mu}\right) dA_s d\Omega_d dx =$$

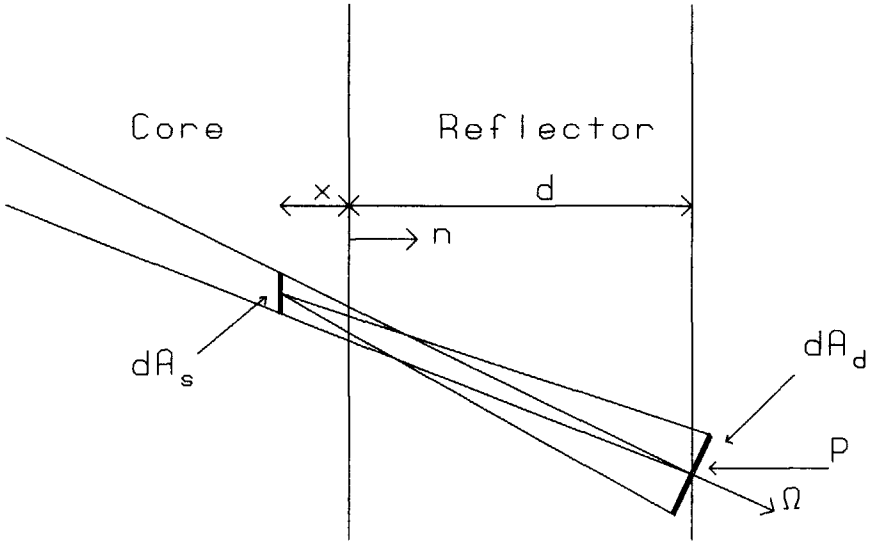


Figure 5.1: Geometry to derive the power of cosine p .

$$= \int_0^{\infty} S_v(x, \Omega) \frac{\exp\left(-\frac{(\Sigma_{tc}x + \Sigma_{tr}d)}{\mu}\right)}{\left(\frac{x+d}{\mu}\right)^2} dA_s dA_d dx \quad (5.6)$$

where x is the distance in the core, d is the reflector thickness, and Σ_{tc} and Σ_{tr} are the total cross sections of the core and reflector, respectively. S_v is the volumetric source strength of the core, which is supposed to have the form: $S_v(x, \Omega) = S_a(\Omega)x$. The number of particles at P in dA_s per unit area perpendicular to Ω is obtained by dividing the RHS of Eq. (5.6) by the detector area dA_d . This number is the contribution to the angular flux at P coming from solid angle $d\Omega_s$:

$$\phi(\Omega)d\Omega_s = \int_0^{\infty} S_a(\Omega)x \frac{\exp\left(-\frac{\Sigma_{tc}x + \Sigma_{tr}d}{\mu}\right)}{\left(\frac{x+d}{\mu}\right)^2} dA_s dx \quad (5.7)$$

Using $d\Omega_s = \mu dA_s / ((x+d)/\mu)^2$, one gets for the flow rate at P:

$$j_n(\Omega) = (\Omega \cdot \mathbf{n})\phi(\Omega) = \int_0^{\infty} S_a(\Omega)x \exp\left(-\frac{\Sigma_{tc}x + \Sigma_{tr}d}{\mu}\right) dx =$$

$$= S_a(\Omega) \frac{\mu^2}{\Sigma_{tc}^2} \exp(-\Sigma_{tr}d/\mu) \quad (5.8)$$

The exponential term can be further simplified for μ close to 1.0 to:

$$\begin{aligned} \exp(-\Sigma_{tr}d/\mu) &= \exp(-\Sigma_{tr}d) \exp\left(\Sigma_{tr}d\left(1 - \frac{1}{\mu}\right)\right) = \\ &= \exp(-\Sigma_{tr}d) \left(\exp\left(1 - \frac{1}{\mu}\right)\right)^{\Sigma_{tr}d} \approx \\ &\approx \exp(-\Sigma_{tr}d) \left(1 + 1 - \frac{1}{\mu}\right)^{\Sigma_{tr}d} \approx \exp(-\Sigma_{tr}d) \mu^{\Sigma_{tr}d} \end{aligned} \quad (5.9)$$

Substituting Eq. (5.9) in (5.8), one gets for the angular flow rate at point P:

$$j_n(\Omega) = S_a(\Omega) \left(\frac{\mu^{2+\Sigma_{tr}d}}{\Sigma_{tc}^2}\right) \exp(-\Sigma_{tr}d) \quad (5.10)$$

It can be seen that an angular flow rate distribution with $p \approx 2 + \Sigma_{tr}d$ is obtained. Above theory is valid for uncollided neutrons only, and will fail for thermal neutrons because the uncollided flux approximation is not valid in this case. Fortunately, the distribution of thermal neutrons diffusing in a finite medium can be described by a Fermi distribution [Pri57]:

$$j_n(\Omega) = \phi_{th} \frac{(\mu + \sqrt{3}\mu^2)}{\pi(1 + 2/\sqrt{3})} \approx \phi_{th} \frac{2.54}{2\pi} \mu^{1.54} \quad (5.11)$$

where ϕ_{th} is the thermal neutron flux at the outer reflector boundary. The approximation holds for μ close to 1.0, and it can be seen that $p \approx 1.5$ for forwardly directed angles for the thermal neutron flux.

The above derived rules-of-thumb have been checked by a discrete ordinates calculation. The neutron flux in a cylindrical core with reflector layers of water, carbon and aluminium with total thickness of $d \approx 25$ cm (see Figs. 5.2 and 6.1) was calculated by the DOT3.5 code [Rho73] in 25 energy groups. Details of this calculation are given in Section 7.1. The angular fluxes at the reflector boundary at core midplane (corresponding to point P in Figs. 5.1 and 5.2), were converted to a boundary source, and the dependence of this flow rate on the cosine of the emergent angle, was fitted to a distribution given by Eq.

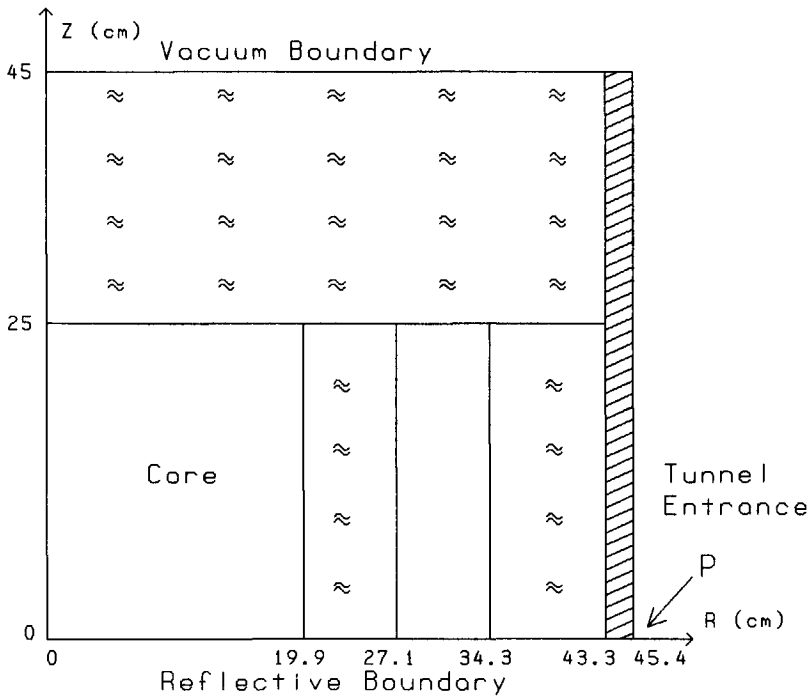


Figure 5.2: Vertical cross section of a quarter of a reactor core surrounded by a reflector. The "empty" layer is graphite, the shaded layer is aluminium and the waves denote water. Core midplane is at $z=0$ cm.

(5.1). A weighted linear least squares fit was used and only cosine values larger than 0.5 were taken into account. The weights were proportional to μ , which gives larger weights to forwardly directed angles, but the results are not very sensitive to the weighting function.

The power p of the flow rate distribution as a function of neutron energy is given in Fig. 5.3. Here it is seen that the fast flow rate has a much more forwardly peaked distribution than the flow rate with energy below 1.0 MeV. The value of p for the first energy group (highest energy) is 5.5, approximately, which corresponds very well with the rule-of-thumb value of Eq. (5.10), because the reflector thickness for that group is about 3.5 mfp. Furthermore, it is seen that the value of p decreases for lower energies to the value predicted by the Fermi distribution.

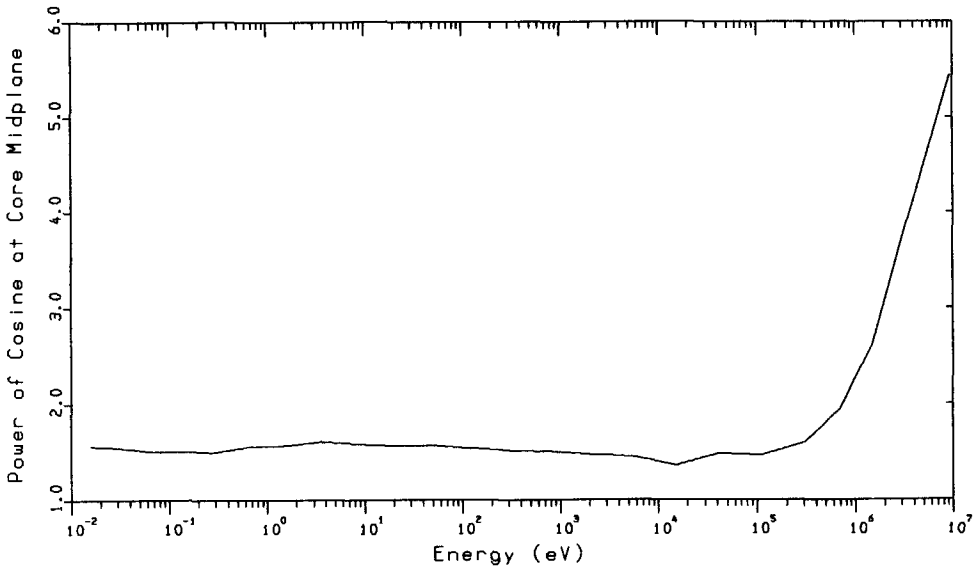


Figure 5.3: Power of cosine p at core midplane level ($z=0$) as a function of energy.

5.3 Albedo Component and Bent Ducts

The albedo component of the radiation in the duct is the flux due to particles, which have scattered in the walls of the duct. Shin [Shi89] derived a model for the calculation of this component, which will be exposed here because of its usage in the IRIDUCT program.

The flux at the duct exit is expanded in a series of one-time scattered flux, two-times scattered flux, etc:

$$\phi(\mathbf{r}_d) \approx \sum_{n=0}^{\infty} S(\mathbf{r}_s) \alpha^n \gamma^n G^{(n)}(r) \quad (5.12)$$

where S is the source strength, α the albedo, γ an empirically derived albedo correction factor and $G^{(n)}$ the n -time scattered flux at distance $r = |\mathbf{r}_s - \mathbf{r}_d|$ from the source, for the special case of unit albedo and unit source strength. Because the $G^{(n)}$ functions have to be calculated and parametrized beforehand, it is assumed that the series can be represented by only three terms: the unscattered flux, a few-times scattered flux and a multiscattered flux. The second term is approximated by the two-times scattered flux, while the third

term is approximated by the eight-times scattered flux. This gives:

$$\begin{aligned} \phi(\mathbf{r}_d) &\approx S(\mathbf{r}_s)G^{(0)}(r) + S(\mathbf{r}_s) \left(\gamma\alpha + \gamma^2\alpha^2 + \gamma^3\alpha^3 \right) G^{(2)}(r) + \\ &\quad + S(\mathbf{r}_s) \left(\gamma^4\alpha^4 + \gamma^5\alpha^5 + \dots \right) G^{(8)}(r) \approx \\ &\approx S(\mathbf{r}_s) \left(G^{(0)}(r) + \left(\alpha + \alpha^2 + \alpha^3 \right) \gamma^2 G^{(2)}(r) + \frac{\alpha^4}{1-\alpha} \gamma^8 G^{(8)}(r) \right) \quad (5.13) \end{aligned}$$

The function $G^{(0)}$ is the unscattered flux per source particle, for which the line-of-sight flux can be used. Because gamma ray albedo values are generally smaller than those for neutrons (this is very much true for the dose albedo), the multiscattered flux contribution for gamma rays (the term with the $G^{(8)}$) is neglected and $G^{(2)}$ is replaced by $G^{(1)}$. The correction factor γ depends on the albedo data, and is fixed for all calculations with the same albedo library. It is chosen such that the flux at the duct exit fits best with measurements.

The one-, two- and eight-times scattered fluxes were numerically calculated for cylindrical ducts, while they were derived by a Monte Carlo code for both rectangular ducts with different width to height ratios, and annuli with different ratios of the inner and outer radii. In general, these functions will be dependent on the source condition. Therefore, they were derived for both an isotropic point source and a flow rate at the duct entrance. The angular dependence of the flow rate distribution is described by two angular bins with respect to the duct axis: one forwardly directed bin with $0.879 \leq \mu \leq 1$ (bin 1) and one with $0 \leq \mu \leq 0.879$ (bin 2). The functions were fitted to an empirical formula. The obtained fitting parameter values can be found in literature [Shi89].

This method is also applicable to bent ducts. For 90 degrees bent ducts, a method is applied by Shin, which is very similar to methods earlier derived for fast neutrons [Sim56] and for gamma rays [LeD59]. The flow rate incident to area I in Fig. 5.4 (A_I in the left picture) is assumed to be totally absorbed. A re-emitted flow rate proportional to the product of the incident flow rate and the albedo is taken for the source in the second leg, which is supposed to have a cosine angular distribution. Furthermore, Shin adds the flow rate incident to area II to the flow rate in the second angular bin ($0 \leq \mu \leq 0.879$). An empirical factor is introduced to give the best fit of the results to measured data. This method for 90 degrees bent ducts cannot easily be applied to

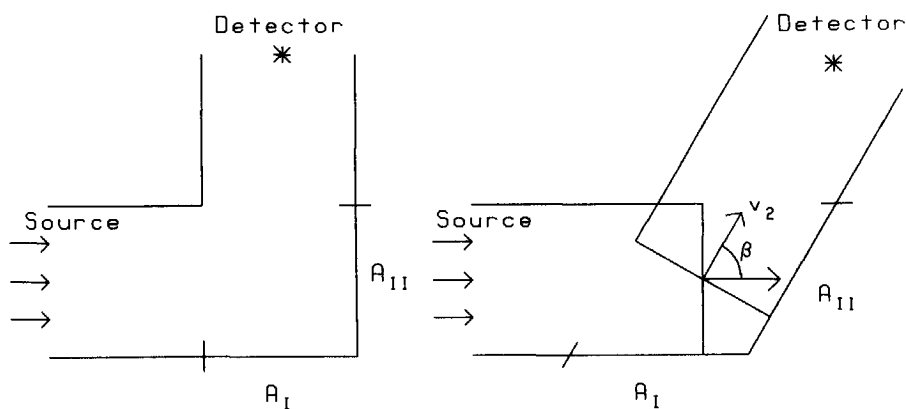


Figure 5.4: Geometry for calculating the source at the entrance of the second leg of a 90 degrees bent duct (left) and a 60 degrees bent duct (right).

general bent ducts, unless one introduces meaningless empirical correction factors. Although such factors are almost unavoidable for simple streaming methods with a very restricted data library, the use of such factors is not very satisfactory. Therefore, another method is proposed.

As the angle of a bent duct (β in Fig. 5.4) increases from 0 to 90 degrees, the flux at the entrance of the second leg is determined more and more by multiscattered particles. This leads to three effects: the flow rate at the entrance of the second leg will be less forwardly peaked, its magnitude will decrease and its spectrum will soften. These effects will be accounted for by the following method.

Up to now, the angular distribution of the albedo was assumed to be cosine shaped with respect to the normal to the wall. This is reasonable if the particles in the wall scatter isotropically or the scatterings are so numerous that the particle flux can be assumed isotropic. In the same way as Eq. (5.10) was derived, it can be found that the emergent angular flow rate has a cosine distribution if $d = 0$ and the volumetric source density $S_v(\Omega)$ is isotropic and uniform.

The angular dependence of the albedo can also be assumed, however, to be due to both single scattering and multiple scatterings in the wall. The single

scattering albedo α_s can be written as [Chi84]:

$$\alpha_s(E, \mu, E', \mu', \phi') = \frac{\Sigma_s^{LAB}(E, E', \mu_s)}{2\pi\Sigma_t(E)} \frac{1}{1 + \frac{\Sigma_t(E')}{\Sigma_t(E)} \frac{\mu}{\mu'}} \quad (5.14)$$

where E and E' are the energies of the incident and emergent particles, respectively, μ and μ' are the cosines of these particles with respect to the normal to the wall, ϕ' is the azimuthal angle with respect to this normal and μ_s is the cosine of the scattering angle in the laboratory system (LAB). It is assumed here that the volumetric source density of scattered particles in the wall decreases exponentially along the incident direction.

If the energy decrement per collision is small, the ratio of the total cross sections of the incident and emergent particles can be assumed to be unity and the energy integrated single scattering albedo writes:

$$\alpha_s(E, \mu, \mu', \phi') = \frac{\Sigma_s^{LAB}(E, \mu_s)}{2\pi\Sigma_t(E)} \frac{1}{1 + \frac{\mu}{\mu'}} \quad (5.15)$$

For neutrons, it is assumed that elastic scattering is dominant, and that the scattering is isotropic in the centre of mass system (CM). The relation between the scattering cross sections in the LAB and CM systems writes [Chi84, Dud76]:

$$\Sigma_s^{LAB}(E, \mu_s) = \Sigma_s^{CM}(E, \mu_c) \frac{(\frac{1}{A^2} + \frac{2\mu_c}{A} + 1)^{3/2}}{1 + \frac{\mu_c}{A}} \quad (5.16)$$

where μ_c is the cosine of the scattering angle in the CM system and A is the atomic mass of the scatterer. The relation between μ_c and μ_s is given by:

$$\mu_c = -\frac{1}{A}(1 - \mu_s^2) + \mu_s \left(1 - \frac{1}{A^2}(1 - \mu_s^2)\right)^{1/2} \quad (5.17)$$

For gamma rays, the Klein-Nishina equation [Chi84] can be used for the scattering cross section in Eq. (5.15). This cross section is obtained by integrating Eq. (4.2) over energy ε' .

The angular dependence of the albedo is now taken as a linear combination of a single scattering and cosine albedo:

$$\alpha(E, E', \mu', \phi') = \alpha(E, E') \left(f \frac{\alpha_s(E, \mu, \mu', \phi')}{\alpha_s(E, \mu)} + (1 - f) \frac{\mu'}{\pi} \right) \quad (5.18)$$

where f is an empirical fraction to be determined yet. By numerically integrating over all outgoing directions, the flow rates in the two angular bins at the entrance of the second leg due to emerging particles from area I, $j_{1I}^{(2)}$ and $j_{2I}^{(2)}$, can be determined:

$$j_{1I}^{(2)}(E') = \int_{0.879}^{1.0} \int_0^{2\pi} \int_0^{\infty} \alpha(E, E', \mu', \phi') j_I^{(1)}(E) \frac{d\Omega'}{d\Omega_2} dE d\phi_2 d\mu_2 \quad (5.19)$$

and:

$$j_{2I}^{(2)}(E') = \int_0^{0.879} \int_0^{2\pi} \int_0^{\infty} \alpha(E, E', \mu', \phi') j_I^{(1)}(E) \frac{d\Omega'}{d\Omega_2} dE d\phi_2 d\mu_2 \quad (5.20)$$

where μ' is the cosine of the polar angle with respect to the normal to the wall of area I (Fig. 5.4, right picture), and ϕ' the azimuthal angle. μ_2 is the cosine of the polar angle with respect to the duct axis of the second leg (vector v_2 in Fig. 5.4, right picture), and ϕ_2 the azimuthal angle. $j_I^{(1)}$ is the flow rate in the first leg incident to area I.

From the flow rates in the two angular bins, the power of the source can be determined by calculating the fraction of the flow rate directed into the second angular bin and the power of the distribution corresponding with this fraction:

$$p = \ln \left(\frac{j_{2I}^{(2)}}{j_{1I}^{(2)} + j_{2I}^{(2)}} \right) / \ln(0.879) - 1 \quad (5.21)$$

Besides scattering against area I, there will also be a contribution to the flow rate directed into the second leg from radiation emerging from areas perpendicular to areas I and II (the floor and roof of the duct in Fig. 5.4). It is assumed that one half of the flow rate of these areas is directed into the second leg. Following Shin, the flow rate incident to area II is added to the flow rate into the second angular bin. These contributions determine the flow rates at the entrance of the second leg in angular bins 1 and 2, which are used to calculate the one-, two- and eight-times scattered fluxes at the exit of the second leg. To determine the line-of-sight flux at the exit of the second leg, the total flow rate is assumed to have a distribution with power p as given by Eq. (5.21). The flow rate directed into the second leg without scattering

against any wall is added to the total flow rate. Summarizing, the flow rates in the two angular bins used to calculate the one-, two- and eight-times scattered fluxes, are:

$$\begin{aligned} j_1^{(2)}(E) &= 2j_{1I}^{(2)}(E) \\ j_2^{(2)}(E) &= 2j_{2I}^{(2)}(E) + j_{II}^{(1)}(E) \end{aligned} \quad (5.22)$$

and the total flow rate used to calculate the line-of-sight flux is:

$$j^{(2)}(E) = 2 \left(j_{1I}^{(2)}(E) + j_{2I}^{(2)}(E) \right) + \phi^{(1)}(E) \cos \beta \quad (5.23)$$

where β is the angle between the centrelines of the two legs of the duct (see Fig. 5.4), $j_{II}^{(1)}$ is the flow rate incident to area II and $\phi^{(1)}$ is the flux at the end of the first leg. The flow rate $j^{(2)}$ is assumed to have a cosine angular distribution with power p according to Eq. (5.21).

The factor f is to be determined yet. It is clear that this factor should be 1 for straight ducts and 0 for 90 degrees bent ducts. It turned out that $f = \cos \beta$ works well.

5.4 IRIDUCT

Based on the methods described above, a program was written to calculate fluxes in straight and bent ducts. The line-of-sight flux at the duct exit is calculated according to Eq. (5.3) for cylindrical ducts and Eqs. (5.4) and (5.5) for annular gaps. Eq. (5.2) is numerically integrated for rectangular ducts.

The albedo component of the flux at the duct exit is calculated according to the method of Shin [Shi89]. For rectangular ducts, the fitting parameters are given for width to height ratios of the duct of 1.5, 2.0 and 4.0. For ducts with width to height ratios between these values, a polynomial fit of second order for the one-, two- and eight-times scattered fluxes is performed to obtain these fluxes for the requested ratio. For ratios less than 1.5, the fluxes for a ratio of 1.0 are calculated by using the scattered fluxes of a cylindrical duct with the same cross sectional area and interpolating again for the fluxes. For annular gaps, the fitting parameters are given for ratios of the inner and outer radius of 0.5, 0.75, 0.87 and 0.95. For ratios between these values, a second order polynomial fit for the scattered fluxes is performed.

Both fluxes and dose-equivalent rates are calculated by the program. Dose-equivalent rates are obtained by multiplying the fluxes by dose-equivalent conversion factors, which have been calculated by the DOSE code [Kni78]. In addition, four response function can be given by the user in the albedo data file.

For multilegged ducts, the method described above is used to calculate the source at the entrance of the second leg. Maximal five legs can be specified in the input and for each bend, the atomic mass of the scatterer must be given. For mixtures, the atomic mass weighted with the scattering cross section will be energy dependent, which is not very practical, and the atomic mass of the lightest nuclide can be used, which will lead to an overestimation of the power p .

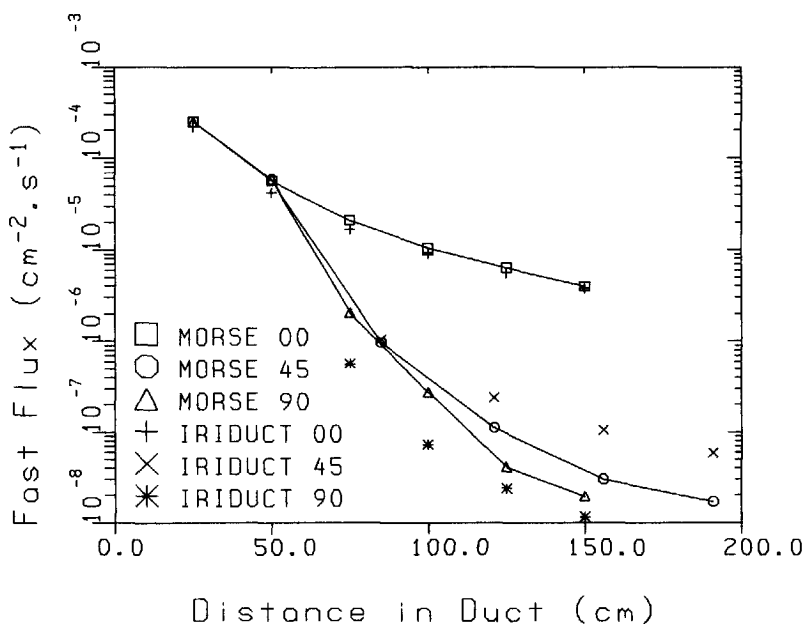


Figure 5.5: Fast flux ($E \geq 1.0$ MeV) per source neutron in a two legged cylindrical duct in concrete. The radius is 5 cm, the length of the first leg 50 cm. The percentage standard deviations of the MORSE-SGC/S results at the end of the second leg are about 25%.

To demonstrate the program, an albedo matrix is calculated in P_3S_8 mode by the one-dimensional discrete ordinates code XSDRNPM-S [Gre83] for 25

energy groups with boundaries given in Table 7.1. An incoming flow rate, homogeneously distributed in the three most oblique incident angles (the S_8 quadrature set has four incident angles with non-zero weight) was defined, and the ratio of the emergent and incident flow rates was taken for the total albedo. Note that the calculation of the total albedo this way, is quite easy compared with the calculation of differential albedo values. Because the values of the total albedo thus obtained are slightly smaller than the ones calculated by Shin, which is probably due to the fact that Shin calculated them for a more oblique incident angle, $\gamma = 1.0$ is used in Eq. (5.13) for the customized albedo library.

Results of the program are shown in Fig. 5.5, which gives the fast fluxes ($E \geq 1.0$ MeV) in a straight duct and in ducts with two legs with angles of 45 and 90 degrees. An isotropic point source is located at the duct entrance with energy in group 3 (1.0 to 2.23 MeV). It can be seen that the flux in the 90 degrees bent duct is slightly underestimated, while the flux in the 45 degrees bent duct is overestimated, compared with results from the MORSE-SGC/S Monte Carlo code [Wes81a]. This latter effect is partly due to the fact that $A = 1$ was used for the atomic mass of the scatterer, which overestimates the power p of the source distribution. A value of 16 (oxygen) is more realistic for concrete in the fast energy region, and the flux at the exit of the 45 degrees bent duct is reduced from $6 \cdot 10^{-8}$ to $3 \cdot 10^{-8}$ $\text{cm}^{-2} \text{s}^{-1}$, while the power p is reduced from 2.0 to 0.6.

Care must be taken not to abuse the IRIDUCT program. A simple method, which consumes only some tens of seconds of CPU time for a problem like Fig. 5.5, is not expected to give as good results as Monte Carlo codes, which consume about 24 hours of CPU time for such a problem. In general it can be said that fluxes, which depend highly on the material used, or on the geometry of the system, cannot be calculated accurately by IRIDUCT. Indeed the thermal flux in the problem of Fig. 5.5, which is only due to downscattering of fast neutrons, is badly represented by IRIDUCT. Just like a point-kernel shielding code, IRIDUCT can only account for the geometry and materials between the source and calculation point. Any influence of the geometry and materials behind the calculation point is not accounted for by the program.

Chapter 6

Neutron Flux Measurements in Straight and Bent Ducts

6.1 Introduction

To judge the capabilities of transport codes in real streaming problems (steel-walled ducts in concrete, irradiated with a typical reactor spectrum), experiments were carried out at the nuclear reactor of the Institute of Nuclear Technics (NTI) of the Technical University of Budapest, in cooperation with the reactor physics group of NTI. Neutron reaction rates were measured in cylindrical ducts (straight and with bends of 30, 60 and 90 degrees) by use of coupled pairs of ${}^6\text{LiF}$ and ${}^7\text{LiF}$ thermoluminescence dosimeters (TLD) and multiple foil activation methods. The research reactor at NTI has a large irradiation tunnel with length of 200 cm, with its centerline through core mid-plane. The geometry from core centre to the tunnel entrance is given in Fig. 6.1.

The concrete block containing the cylindrical steel-walled duct, could be placed in the tunnel up to 25 cm from the tunnel entrance. At the back of the large concrete block, a small block containing the second leg of the duct with a bend of 0, 30, 60 or 90 degrees, could be positioned, with the second leg upwardly directed (see Fig. 6.2). In this way four different duct geometries were created (see Fig. 6.3). Because the upper side of the block touched nearly the ceiling of the tunnel, the second leg of the 60 degrees bent duct was partly closed and that of the 90 degrees bent duct was fully closed. The backscattering from the ceiling of the tunnel is taken into account in the calculations. About 21 cm behind the last detector position in the 30 degrees duct measured along the duct axis, a shielding door filled with water was present, which was also accounted for in the calculations. This shielding door was neglected in the straight duct, because the last detector position in this duct was positioned further away from the shielding door and the thermal

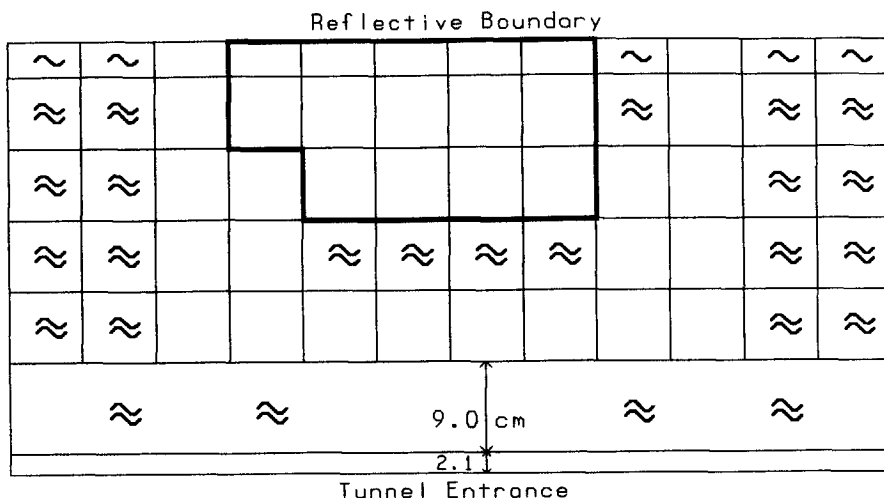


Figure 6.1: Horizontal cross section of the core and shields up to the tunnel entrance. The squares are assemblies with size of $7.2 \times 7.2 \text{ cm}^2$. The half core is in bold, the other "empty" assemblies constitute the graphite reflector, while the waves denote water. The layer with thickness 2.1 cm is made of aluminium. The active core height is 50 cm.

neutron flux was much higher in this duct due to the large contribution of the uncollided flux.

The inner and outer diameters of the steel liner of the duct were 11.8 cm and 12.7 cm, respectively. The detector holders consisted of aluminium disks with thickness of 1.5 mm, which fitted precisely in the duct and which were kept at a constant distance from each other by thin aluminium bars. The detectors could be placed on the disk at four positions on a straight line through the disk centre at distances of 2.5 and 5.0 cm from the centre. The foils were irradiated in a small aluminium capsule with thickness of 0.5 mm, or in a cadmium capsule with thickness of 1 mm. The detector positions in the ducts are given in Fig. 6.3.

6.2 Thermoluminescence Measurements

Measurements were performed by use of thermoluminescence dosimetry. This method makes use of TLD samples, made of crystallyne material dotated with

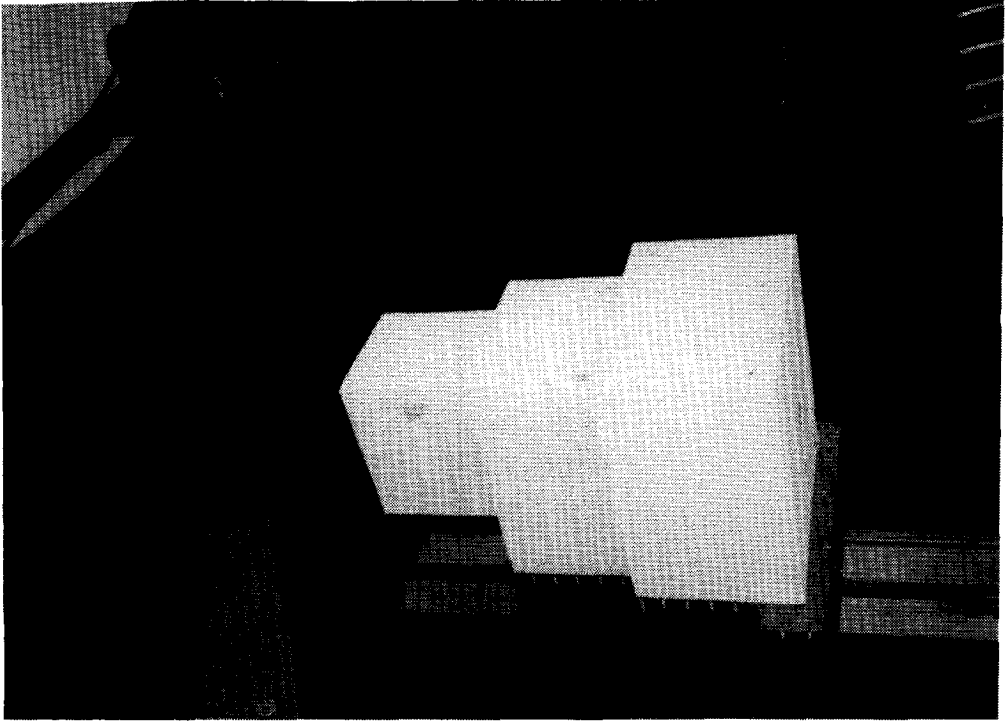


Figure 6.2: The concrete blocks containing the straight duct.

some impurities to create so-called trapping centres with energies between the valence and conduction bands. If the samples are irradiated, the absorbed ionizing radiation produces free electrons and holes, which may be trapped in the trapping centres of the material. After the irradiation, the TLD samples are heated, and the trapped electrons and holes are released. If they recombine, a photon in the visible region is produced (if the energy gap between the valence and conduction band is about 3 to 4 eV), which may be detected by a photomultiplier. In this way, a plot of the measured light intensity versus the temperature of the TLD sample is obtained, which is usually called a glowcurve. The integrated count yield of the glowcurve is proportional to the absorbed energy in the sample during the irradiation (if no saturation effects occur).

Measurements were carried out by pairs of ${}^6\text{LiF}$ (TLD600) and ${}^7\text{LiF}$ (TLD-

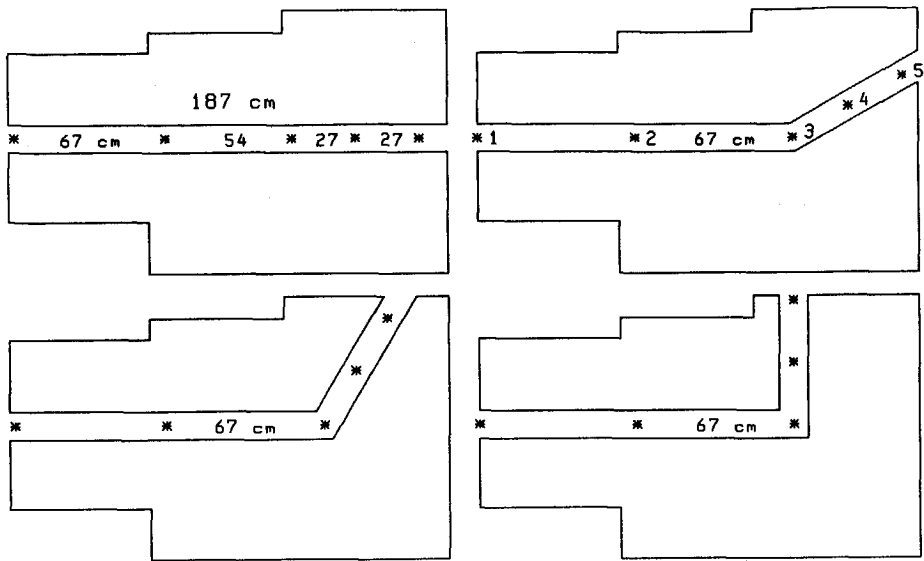


Figure 6.3: Vertical cross section of the four different duct geometries as described in the text. The detectors (marked by an asterisk) are numbered from left (core side) to right as in the 30 degrees duct. The distances between the detectors are the same for all geometries except for detectors 2 and 3.

700) TLD samples with size of $3.1 \times 3.1 \times 0.89 \text{ mm}^3$. All samples of each group of TL materials were equally sensitive to gamma rays within 3% (percentage standard deviation), while all the TLD600 samples were equally sensitive to neutrons within 5%. The gamma ray sensitivity of the TLD600 samples is about 1.7 times as large as that of the TLD700 samples. This may be caused by different impurity concentrations of the two types of materials [Bos92]. The neutron sensitivity of TLD600 samples is much higher than that of TLD700 samples by means of the $(n,\alpha) 1/v$ capture reaction in ${}^6\text{Li}$ ($\sigma_c \approx 940$ barn at 0.025 eV). Although the (n,α) cross section of ${}^7\text{Li}$ is zero, the presence of a small amount of ${}^6\text{Li}$ in TLD700 leads to a low neutron sensitivity of TLD700. The consequences of this will be described later. The TLD samples were read out twice with a heating rate of $6 \text{ K}\cdot\text{s}^{-1}$ and the counts of the second reading were subtracted from the first one to correct for zero dose counts and signal noise in the photomultiplier equipment, etc. The annealing procedure, needed to restore the trapping centres before each irradiation, was the same for all

samples: one hour at 400 °C and two hours at 100 °C.

Because the TLD samples were irradiated pair wise (two TLD600 samples at the one side of the disk and two TLD700 samples at the other side, symmetrical with respect to the centre of the disk), both the gamma dose and the neutron reaction rate could be determined. If C_6 and C_7 are the count yields of a TLD600 and TLD700 sample at the same measurement position, respectively, it is straightforward to find that:

$$C_{7\gamma} = \frac{C_6 - \beta C_7}{\alpha - \beta} \quad (6.1)$$

and:

$$C_{6n} = C_6 - \alpha C_{7\gamma} \quad (6.2)$$

where $C_{7\gamma}$ is the count yield of the TLD700 sample due to gamma rays and C_{6n} is the count yield of the TLD600 sample due to neutrons. The calibration factors α and β are defined as follows:

$$\alpha = \frac{S_{6\gamma}}{S_{7\gamma}} \text{ and } \beta = \frac{S_{6n}}{S_{7n}} \quad (6.3)$$

where $S_{6\gamma}$, $S_{7\gamma}$, S_{6n} and S_{7n} are the sensitivities of the TLD600 and TLD700 samples to the gamma ray and neutron fluxes, respectively. These sensitivities are determined by ^{60}Co and PuBe sources. The count rate due to the gamma background of the PuBe source was determined by the difference of (a) TLD700 samples enwrapped completely by TLD700 and (b) TLD700 samples enwrapped completely by TLD600. From this measurement it was found that about 90% of the TLD700 count rate at the neutron calibration was due to the gamma background. Parameter β can thus be calculated if α is known. The value of α , found from the gamma calibration, is within the range 1.6 to 1.9, while β is within 185 to 249. The variation in these numbers is due to the fact that TLD samples within one batch are selected on their sensitivity within certain limits (usually within 10%). The value of α is determined for each pair of TLD600 and TLD700 samples separately, but β is measured for only two pairs of TLD samples. The error in β may therefore be rather large. The neutron sensitivity of the TLD700 samples is very small, however, and the neutron count yields of the TLD600 samples are rather insensitive to β . This follows from Eqs. (6.1) and (6.2) for $\beta \gg \alpha$.

To avoid fading effects, which could have affected the count rate of the TLD samples, the time lag of two weeks, which was present between the measurements and analysis of the TLD samples, was also present at the calibration procedure of the TLD samples. Because the actual dose at the neutron calibration was unknown, the neutron response of each TLD600 sample is normalised with respect to the average neutron response of all TLD600 samples. To find a value for the error of this relative response, two additional neutron calibrations were performed (without a time lag of two weeks) and the neutron responses of TLD600 sample i for these two calibrations (x_i and y_i , respectively) were calculated together with the mean values of all responses (\bar{x} and \bar{y} , respectively). For the mean value of the difference then holds:

$$\bar{\Delta} = \frac{1}{N} \sum_{i=1}^N \Delta_i = \frac{1}{N} \sum_{i=1}^N \left| \frac{x_i}{\bar{x}} - \frac{y_i}{\bar{y}} \right| \quad (6.4)$$

where N is the number of TLD600 samples. The value of $\bar{\Delta}$ thus found is taken for the error of the relative neutron response of each TLD600 sample. The same procedure as described above is used for determining the relative gamma response of the TLD600 and TLD700 samples. The errors thus found are about 5% for the neutron sensitivities and slightly less than 1% for the gamma sensitivities. Implicitly, it is assumed here that both α and β are spectrum independent. This assumption is valid for α , because gamma rays only interact with the electrons in the TLD sample and no energy dependence due to different Li isotopes is to be expected. The assumption is not valid for β because of self shielding in TLD600 samples, which leads to a distortion of the $1/v$ capture cross section for low energies of these samples and thus to a spectrum dependent value for β as will be shown further on. Fortunately, this has no significant influence on the neutron results, because of the insensitivity of these results with respect to β .

The energy sensitivity of the TLD samples is obtained from an adjoint one-dimensional discrete ordinates calculation with XSDRNPM-S [Gre83]. The sample is modelled as an infinite slab of 0.89 mm thickness and the (n,α) cross section of ${}^6\text{Li}$ is taken for the source spectrum. The point value χ^* at the boundary of the TLD sample is taken for the energy sensitivity of the detector. This is equal to calculating the response of the TLD sample to an isotropic point source with unit source strength, positioned just near the TLD sample (see Section 1.3). An approximate expression for this response can be

obtained by neglecting scattering in the TLD sample. The response for energy group g in this case becomes:

$$R_g = \int_0^1 \int_0^D \int_0^{2\pi} \frac{1}{2\pi} \exp\left(-\Sigma_t^g \frac{x}{\mu}\right) \frac{\Sigma_c^g}{\mu} d\phi dx d\mu = \frac{\Sigma_c^g}{\Sigma_t^g} [1 - E_2(\Sigma_t^g D)] \quad (6.5)$$

where R_g is the response function, D is the total thickness of the TLD sample (0.89 mm), x/μ is the distance in the sample along the ray with azimuthal angle ϕ and polar angle cosine μ and Σ_t^g and Σ_c^g are the total and capture cross sections of the TLD sample, respectively. E_2 is the exponential integral function of the second order [Chi84]. The capture cross section is assumed to be only due to the (n, α) reaction in ${}^6\text{Li}$. In Eq. (6.5) scattering in the TLD sample is neglected, while this is taken into account in the adjoint XSDRNPM-S calculation.

Another possibility to calculate the energy sensitivity of a TLD sample is to calculate the response to a point source with unit source strength and cosine angular distribution. This leads to:

$$R_g = \int_0^1 \int_0^D \int_0^{2\pi} \frac{\mu}{\pi} \exp\left(-\Sigma_t^g \frac{x}{\mu}\right) \frac{\Sigma_c^g}{\mu} d\phi dx d\mu = \frac{\Sigma_c^g}{\Sigma_t^g} [1 - 2E_3(\Sigma_t^g D)] \quad (6.6)$$

where E_3 is the exponential integral function of the third order.

The energy sensitivities calculated above, can be viewed of as the probabilities that a neutron of a point source positioned just near a TLD sample (isotropic or cosine distributed) is captured in the sample by ${}^6\text{Li}$. In Fig. 6.4 the capture probabilities for TLD600 and TLD700 samples are shown, according to the adjoint XSDRNPM-S calculation and to Eqs. (6.5) and (6.6). The difference between the adjoint calculation and Eq. (6.5) is very small, but the difference between these two methods and Eq. (6.6) is rather large. The cosine distributed point source is more forwardly directed to the TLD sample, which leads to a smaller effective thickness of the sample and therefore to a smaller capture probability in the TLD700 sample and in the TLD600 sample for high energies. For low energies, the TLD600 sample is still completely black and no difference is seen between the isotropic point source and the cosine point source.

It can be seen in Fig. 6.4 that the TLD700 sample has a real $1/v$ dependence. This relation is distorted for TLD600 at low energies because of self

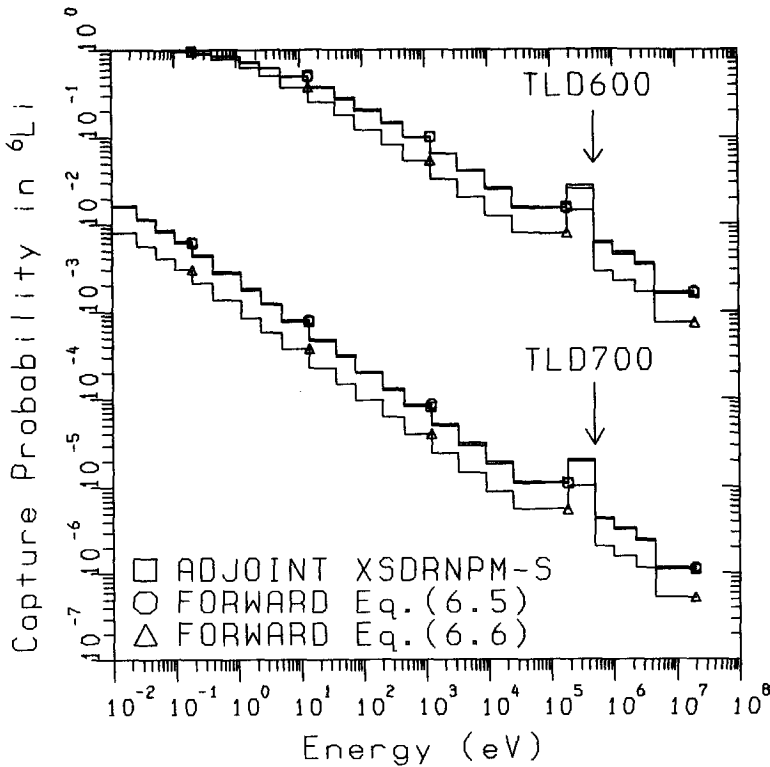


Figure 6.4: Capture probabilities for TLD600 and TLD700 samples, calculated by XSDRNPM-S and from Eqs. (6.5) and (6.6).

shielding in the sample. The ratio between the TLD600 and TLD700 responses is the factor β again, which is seen to be energy dependent due to this self shielding effect. The values of β calculated by XSDRNPM-S, range from about 60 for low energies to 1400 for high energies. This latter value is equal to the ratio of the ${}^6\text{Li}$ nuclide concentrations in the TLD600 and TLD700 samples. The values of β averaged with the calculated fluxes in the ducts (see Section 7.1) as a weighting factor, range from 96 to 113 for the energy sensitivity according to Eq. (6.5) and from 194 to 215 for the energy sensitivity according to Eq. (6.6). The differences between the β values of the two methods, is due to the fact that the energy sensitivity of TLD700 in the latter case is smaller over the whole energy range by a factor of two, approximately.

Which energy sensitivity curve of Fig. 6.4 is correct depends on the angular flux distribution in the ducts during the irradiation, which is unknown. The TLD700 measurements are only used to correct the TLD600 count yield for the gamma ray contribution and this correction is only slightly dependent on β . This means that only the TLD600 energy sensitivity curve is used for the comparison of the calculations and measurements. Because the calculated and measured results are compared in a relative way (the response of a TLD sample in the duct is normalised to the response of the TLD sample at the duct entrance), the differences between the three methods turned out to be negligible, compared with the measurement errors. The values of β measured at the neutron calibration (185 to 249) were used to calculate the measured TLD600 neutron count yield (C_{6n} in Eq. (6.2)).

It is noted that the interpretation of the gamma ray count yield of the TLD samples is quite different from the interpretation of the neutron count yield. Gamma rays only interact with the electrons in the TL material, and the number of electron-hole pairs created in the TL material will be proportional to the energy deposited in the TLD sample. The gamma ray count yield is thus proportional to the gamma dose in the TLD sample.

The neutron count yield will be a measure of the number of (n,α) reactions in the TLD sample during the irradiation. If the cross section for the (n,α) reaction would have a $1/v$ dependence over the whole energy range, the neutron count yield would be a measure for the neutron density during the irradiation. This is the case for TLD700 over a large energy range (see Fig. 6.4), but not for TLD600 because of selfshielding in the sample. The interpretation of the TLD600 count yield is therefore not so easily understood.

6.3 Multiple Foil Activation Measurements

Neutron flux spectra at different measurement positions were determined by multiple foil activation measurements. Foils were irradiated in the ducts and the activities of the foils were measured. From these activities, the saturation activity per target nucleus of the foils were calculated, which were used in the SANDBP neutron spectrum adjustment code [Zso82]. The input spectra were calculated beforehand by discrete ordinates and Monte Carlo shielding codes described in Section 7.1.

The activity of a foil after an irradiation time T_r writes:

$$A(T_r) = \lambda N(T_r) = N_0(1 - \exp(-\lambda T_r)) \int_0^{\infty} \phi(E)\sigma(E)dE \quad (6.7)$$

where λ is the decay constant of the nuclide under consideration, N_0 is the initial number of target nuclei before the irradiation, and σ is the neutron reaction cross section of the nuclide. The integral on the RHS of Eq. (6.7) is the saturation activity per target nucleus, which is to be determined from the measurements.

After the irradiation with duration T_r and a cooling period with duration T_c , the activities of the irradiated foils were measured during a time interval T_m , which varied from several minutes to several hours, dependent on the half-life of the nuclide. The measurements were done by two HPGe (High Purity Germanium) detectors. The pulse heights of these detectors were recorded by 4096 channels pulse height analysers. From the spectra thus obtained (number of detected gamma rays versus gamma ray energy), the measured saturation activity per target nucleus can be obtained. If the nuclide decays via several decay modes, the saturation activity per target nucleus calculated from peak i in the measured gamma spectrum becomes:

$$A_i^m = \frac{P_i k}{T_m \eta_i \gamma_i} \frac{\exp(\lambda T_c)}{N_0(1 - \exp(-\lambda T_r))} \quad (6.8)$$

where P_i is the number of counts of peak i (also called the peak area), k is the dead time correction factor, η_i is the efficiency of the detector and γ_i is the gamma yield of the nuclide. The change of the nuclide activity during the measurements was automatically accounted for, but generally this correction was negligible. If the nuclide decays via several decay modes, a weighted mean saturation activity per target nucleus of the nuclide is calculated:

$$A^m = \frac{\sum_i A_i^m / \sigma_i^2}{\sum_i 1 / \sigma_i^2} \quad (6.9)$$

where σ_i is the standard deviation of the activity of peak i , which is in practice mainly determined by the variance of the peak area and to a lesser extent by the variance of the detector efficiency.

One well-type detector and one detector with adjustable foil-detector distance were used. The first one was mainly used for low activity foils, while the latter one was used for high activity foils. Foil-detector distances of 10, 50 or 150 mm were used, in such a way that the dead time correction could be done automatically by the live-time option of the measurement system. This correction was generally less than 5% for all foils. The efficiency of the detector with adjustable foil-detector distance was determined at 150 mm by 11 calibration sources. A power series on double logarithmic coordinates was used to fit the detector efficiency as a function of energy:

$$\ln \eta(E) = \sum_n a_n (\ln E)^n \quad (6.10)$$

where a_n are the fit parameters. Two different fits were made for the low and high energy regions, respectively, and the joining point around 100 keV was found by trial and error, such that the sum of squared deviations between measured and known activities was minimized. In this fit, n ranged from 0 to 3 for the low energy region and from 0 to 4 for the high energy region. The detector efficiencies corresponding with other foil-detector distances and with the well-type detector, were determined by measuring the same foils at both detectors and at all distances of interest.

After the saturation activity per target nucleus of each foil was calculated, spectrum adjustment calculations could be done by SANDBP using cross sections from refs. [Koc90, Cul85, Zij84]. The 640 groups cross sections of these libraries were collapsed to 50 groups ranging from 10^{-10} to 20 MeV, by use of a typical neutron spectrum measured in the irradiation tunnel beforehand. This 50 groups structure has a fine enough structure to give adequate spectrum information, while more energy groups would have made the adjustment procedure more difficult because of the increase of the number of freedoms. Input spectra for the unfolding procedure were provided in a 25 groups structure by calculations described in Section 7.1. The fluxes of these calculations were converted to point energy spectra by dividing each group flux by the energy width of the group and using the logarithmic mean energy as the characteristic energy of that group. Using a log-log interpolation scheme, and the extrapolation routines from the SANDBP program, these point energy spectra were converted to the 50 groups structure used for the adjustment procedure. The low end of these spectra were extrapolated by a Maxwellian spectrum with neutron temperature of 306 K, and the $1/E$ -Maxwellian joining point at

0.185 eV. The high end of these spectra were extrapolated by a Watt fission spectrum.

At each iteration step, these group spectra are normalised to obtain reaction rates, which fit best with the measured data. If the activities of different foils are uncorrelated, the sum of squared deviations of the relative differences between measured and calculated activities writes:

$$\epsilon^2 = \sum_{n=1}^N \frac{(A_n^m - f_k \cdot A_n^k)^2}{(A_n^k)^2} \quad (6.11)$$

where A_n^m are the measured activities of nuclide n , and A_n^k are the calculated activities based on the neutron spectrum of the k^{th} iteration. Before the first iteration ($k = 0$), the calculated input spectrum is used. Minimizing ϵ^2 with respect to f_k leads to the expression for the normalization factor f_k [Zij83]:

$$f_k = \frac{1}{N} \sum_{n=1}^N \frac{A_n^m}{A_n^k} \quad (6.12)$$

At each iteration, the group fluxes are adjusted exponentially:

$$\phi_g^{k+1} = \phi_g^k \exp(C_g^k) \quad (6.13)$$

with C_g^k equal to:

$$C_g^k = \frac{\sum_{n=1}^N W_{n,g}^k \ln(A_n^m/A_n^k)}{\sum_{n=1}^N W_{n,g}^k} \quad (6.14)$$

where $W_{n,g}^k$ is a weight factor for nuclide n and group g , which was chosen equal to:

$$W_{n,g}^k = \frac{A_{n,g}^k}{A_n^k} \left(\frac{1}{\frac{\sigma_n}{A_n^m}} \right)^2 \quad (6.15)$$

with σ_n the standard deviation of the measured activity A_n^m . The adjustment procedure is stopped if the standard deviation of the measured to calculated activity ratios $(A_n^m - A_n^k)/A_n^k$ is less than a value determined beforehand, or if the maximum number of iterations defined in the input is reached.

Table 6.1: Foils used for the measurements of the fast neutron spectra. The energy response intervals given in the table account for 90% of the nuclide activities. All foils are infinitely diluted. The thicknesses of the foils are about 0.1 to 0.25 mm.

Reaction	Cadm. Cover	Energy (MeV)	Positions				
$^{56}\text{Fe}(n,p)^{56}\text{Mn}$	No	5.5-12.5	00.1	00.3	00.4	00.5	30.2
			60.2	60.3	90.2	90.3	
$^{54}\text{Fe}(n,p)^{54}\text{Mn}$	No	2.3-10.0	00.1	30.2	60.2	90.2	
$^{58}\text{Ni}(n,p)^{58}\text{Co}$	No	2.3-10.0	00.1	00.4	30.1	60.3	90.1
$^{115}\text{In}(n,n')^{115m}\text{In}$	No	1.0-6.7	00.1	00.2	00.3	00.4	00.5
			30.1	30.3	30.4	30.5	
			60.1	60.2	60.3	60.4	60.5
			90.1	90.2	90.3	90.4	

Tables 6.1 and 6.2 give listings of the foils used, together with the irradiation positions (00.1 means the first position in the straight duct, 30.3 the third position in the 30 degrees duct, etc.). Both bare and cadmium covered foils were used. The measured activities of the cadmium covered foils are much less than those of the bare foils and the energy response intervals of the cadmium covered foils are shifted to higher energies, because of the absorption of almost all thermal neutrons ($E \leq 0.4$ eV) in the 1 mm thick cadmium cover. The cadmium covered cross sections are accounted for in the SANDBP program by use of effective cross sections, which include the absorption of thermal neutrons in the cadmium cover by exponential attenuation. All the foils used were infinitely diluted, except the $^{45}\text{Sc}(n,\gamma)$ foils, for which self shielding in the foil is accounted for by use of Eq. (6.6). It is noted that the energy response intervals given in the tables, depend on the neutron spectrum and thus on the position in the ducts. As can be deduced from Tables 6.1 and 6.2, at many positions in the ducts, only a small number of activation foils could be evaluated, which was not enough to do meaningful spectrum adjustment calculations. Therefore, measured and calculated activation rates should be compared with each other. It can also be seen that no detector responses for the energy range from 1.0 keV to 1.0 MeV were present. Generally, it is

Table 6.2: Foils used for the measurements of the thermal and resonance parts of the neutron spectra. The energy response intervals given in the table account for 90% of the nuclide activities. All foils are infinitely diluted except the $^{45}\text{Sc}(n,\gamma)$ foils. The thicknesses of the foils are less than 0.1 mm.

Reaction	Cadm. Cover	Energy (eV)	Positions
$^{55}\text{Mn}(n,\gamma)^{56}\text{Mn}$	No	0.001-0.255	00.1 00.4
			30.1 30.2 30.3 30.4 30.5
			60.1 60.2 60.3 60.4 60.5
			90.1 90.2 90.3 90.4 90.5
$^{55}\text{Mn}(n,\gamma)^{56}\text{Mn}$	Yes	0.55-1600.0	00.1 00.2 00.3
			30.1 30.2 30.3
			60.1 60.2 60.3 60.4
			90.1 90.2 90.3 90.4
$^{197}\text{Au}(n,\gamma)^{198}\text{Au}$	No	0.001-6.3	00.1 00.3 00.4 00.5
			30.1 30.3 30.4 30.5
			60.1 60.3 60.4 60.5
			90.1 90.3 90.4 90.5
$^{197}\text{Au}(n,\gamma)^{198}\text{Au}$	Yes	2.8-6.3	00.1 00.3 00.4 00.5
			30.3 30.4 60.1 60.3
			90.1 90.3 90.4
$^{45}\text{Sc}(n,\gamma)^{46}\text{Sc}$	No	0.001-0.115	00.1 00.3 00.5
			30.3 30.4 30.5
			60.3 60.4 60.5
			90.3 90.4 90.5
$^{45}\text{Sc}(n,\gamma)^{46}\text{Sc}$	Yes	0.255-1600.0	00.1 00.3 00.4 00.5
$^{186}\text{W}(n,\gamma)^{187}\text{W}$	No	0.028-30.0	00.2
$^{186}\text{W}(n,\gamma)^{187}\text{W}$	Yes	13.5-30.0	00.1
$^{139}\text{La}(n,\gamma)^{140}\text{La}$	No	0.001-135.0	00.3 00.4 00.5 30.4
$^{139}\text{La}(n,\gamma)^{140}\text{La}$	Yes	0.55-1600.0	00.1 00.2

difficult to cover this energy range with activation detectors, because it is too high for resonance detectors and too low for threshold detectors. Detectors suitable for this energy range (e.g. $^{237}\text{Np}(n,f)$ and $^{93}\text{Nb}(n,n')$ reactions) gave no adequate responses in the ducts.

To compare measured and calculated reaction rates, cross sections are retrieved from the JEF1.1 data file [JEF85] and processed by the NJOY89 code [Mac87], to obtain infinitely diluted cross sections. The activation rates of cadmium covered foils are obtained by use of effective cross sections, which account for the shielding in the cadmium cover. This shielding factor is calculated for each group according to Eq. (6.6). Reaction rates are then obtained by multiplying the cross sections of a particular group with the corresponding calculated group flux and summing over all groups. The differences between the Au and Mn reaction rates thus obtained, and those from the SANDBP output before the first iteration, is about 10–15%. This is generally within one standard deviation of the calculated reaction rates. For the $^{56}\text{Fe}(n,p)^{56}\text{Mn}$ reaction this difference is about 35–40% (3 to 4 standard deviations). Because the differences are systematic (they have the same sign and same magnitude for each particular reaction) they are likely to be caused by the coarse energy group structure in the calculations, which can lead to errors due to different cross section treatment and spectrum conversion. Calculating the reaction rates in 25 broad energy groups cannot be very accurate of course, because the cross sections are weighted with a Maxwellian- $1/E$ -fission spectrum. On the other hand, converting the calculated spectrum from 25 broad energy groups via a continuous spectrum to 50 fine energy groups, as is done in the SANDBP code, also introduces errors. This may also explain the large discrepancies for the $^{56}\text{Fe}(n,p)^{56}\text{Mn}$ reaction. The cross section of this threshold reaction is only non-zero above 5 MeV. Because the flux in this energy region is calculated by MORSE-SGC/S in only one energy group (4.5–19.6 MeV), and the logarithmic mean energy of this group is rather high (9.39 MeV), the actual flux level of the fission spectrum in SANDBP before the first iteration, is overestimated. If 8.5 MeV is used for the characteristic energy of the first group, a nice agreement is found between the calculated reaction rates of ^{56}Fe and those from the SANDBP output before the first iteration. The influence of this modification on the adjusted spectrum turned out to be only a few percent. To avoid discrepancies due to spectrum conversions like this, more fast groups in the shielding calculations are required. For the $^{58}\text{Ni}(n,p)^{58}\text{Co}$

reaction, which is sensitive to lower energies ($E \geq 2$ MeV), the discrepancy is only a few percent.

Because no uncertainty was assigned to the reaction rates from the SANDBP output, the values obtained in the way described above (by use of the infinitely diluted cross sections from the JEF1.1 data file) were used to compare measured and calculated reaction rates in Section 7.2, without presuming that these values are better than the ones from the SANDBP output before the first iteration. For the $^{115}\text{In}(n,n')^{115m}\text{In}$ reaction the SANDBP output is used because no correct cross sections were available from the JEF1.1 data file. It must be emphasized that the uncertainties in the reaction rates thus obtained, are only due to the standard deviations of the calculated group fluxes. The errors due to the cross sections and their treatment are not included.

6.4 Measurement Procedures

The measurements were performed in January 1991, after the reactor was shut down for 3 weeks. By means of a few test irradiations, the necessary irradiation times for the TLD samples at all positions were determined. Because the TLD responses at the first and second detector positions differed already by a factor of 50, these two detector positions were measured separately from the second till the fifth ones. The TLD samples at the first and second detector positions were irradiated for 5 minutes and at a reactor power of 10 W, while the ones at the second till the fifth positions of the straight duct were irradiated for 30 minutes with the same power, and in the bent ducts for 30 minutes with a power of 50 W.

The foil activation measurements were performed at the maximum power of 100 kW for 10, 11, 12 and 15 hours for the 0, 30, 60 and 90 degrees bent ducts, respectively. For the straight duct, two irradiations were performed to avoid difficulties of measuring too many foils with short half-life. After the irradiations, the concrete blocks were kept in the irradiation tunnel for a cooling period of 1.5 hours. Despite this cooling period, the exposure rate at the front side of the concrete blocks was about $25 \text{ R}\cdot\text{hr}^{-1}$, due to activation of nuclides in the concrete and in the painting of the concrete blocks. Directly after this cooling period, the activities of the foils were measured in the way described in Section 6.3. The integrated reactor power was monitored with aid of Au activation detectors.

Chapter 7

Calculations and Comparison with Measurements

7.1 Calculations

Calculations are performed by different computer codes. First the cross sections of the core and shield layers are generated by the SCALE-3 system [Gre81, Wes81b, Gre83], by collapsing cross sections from 172 fine groups to 25 broad groups. These collapsed cross sections are used for the shielding calculations. The neutron angular fluxes at the tunnel entrance are calculated by a two-dimensional discrete ordinates code. These angular fluxes are subsequently used to calculate the source for the duct shielding calculations, which are performed by a three-dimensional Monte Carlo code.

Cross sections are collapsed from a 172 groups library, which is based on the JEF1.1 data library [JEF85] and prepared by the NJOY87 code [Mac87]. Unresolved resonance treatment according to the Bondarenko method is done by the BONAMI-S code [Gre81] for ^{235}U and ^{238}U . Resolved resonance treatment for these two nuclides and iron is done according to the Nordheim method by the NITAWL-S code [Wes81b].

To generate core cross sections in 25 groups, a microscopic cell calculation was done by XSDRNPM-S [Gre83] in cylindrical geometry. The cell contained fuel, cladding, moderator and aluminium with radii of 0.35, 0.50, 0.989 and 1.016 cm, respectively. The aluminium was included in the cell to account for the aluminium wall of the fuel assemblies. Also the water layer is slightly enlarged to account for the water between adjacent assemblies. The height of the cell was decreased to 23.4 cm to increase the leakage in vertical direction to meet the criticality condition. The energy boundaries and lethargy increments are given in Table 7.1.

The cross sections of the reflector and shield layers are obtained by a macroscopic cell calculation in plane geometry. The cell consisted of a core zone of 18 cm with a reflective boundary at the one side and reflector and

Table 7.1: Energy group boundaries and the lethargy increment per group for the 25 group structure used for the streaming calculations.

Group	Energy	Δu	Group	Energy	Δu
1	19.60 MeV	1.47	14	75.7 eV	0.71
2	4.49	0.70	15	37.3	1.00
3	2.23	0.80	16	13.7	1.00
4	1.00	0.70	17	5.04	0.76
5	497.9 keV	1.00	18	2.36	0.75
6	183.2	1.00	19	1.12	1.03
7	67.4	1.00	20	0.40	0.74
8	24.8	1.00	21	0.19	0.64
9	9.12	1.00	22	0.10	0.69
10	3.35	1.00	23	0.05	0.69
11	1.23	1.00	24	0.025	0.92
12	454.0 eV	0.80	25	0.010	4.51
13	204.0	1.00		0.00011	

shield zones at the other side. These latter zones contained water, carbon, water, aluminium, iron and concrete with thicknesses of 7.2, 7.2, 9.0, 2.1, 0.45 and 10.0 cm, respectively (see Fig. 6.1). The last two zones represent the iron liner and the concrete of the blocks. Only one cross section set for each shield material is obtained. For deep penetration calculations, it is widely accepted, that different cross sections should be used for different parts of the shield, despite the fact that the shield is of homogeneous composition. To keep the cross section data set as small as possible to avoid "supergrouping" in the MORSE-SGC/S Monte Carlo code [Wes81a], which would make it impossible to calculate the point values in a forward Monte Carlo run (see Section 8.2), only one cross section set for each shield material is used. The introduced error is difficult to estimate. For duct streaming calculations, the first shield layer around the duct, which is the most important one with respect to scattering in the duct, is irradiated to a first approximation by the line-of-sight flux, which can hardly be calculated by a one-dimensional code.

The collapsed libraries from both the microscopic and macroscopic cell calculations do not include upscattering, because the library produced by

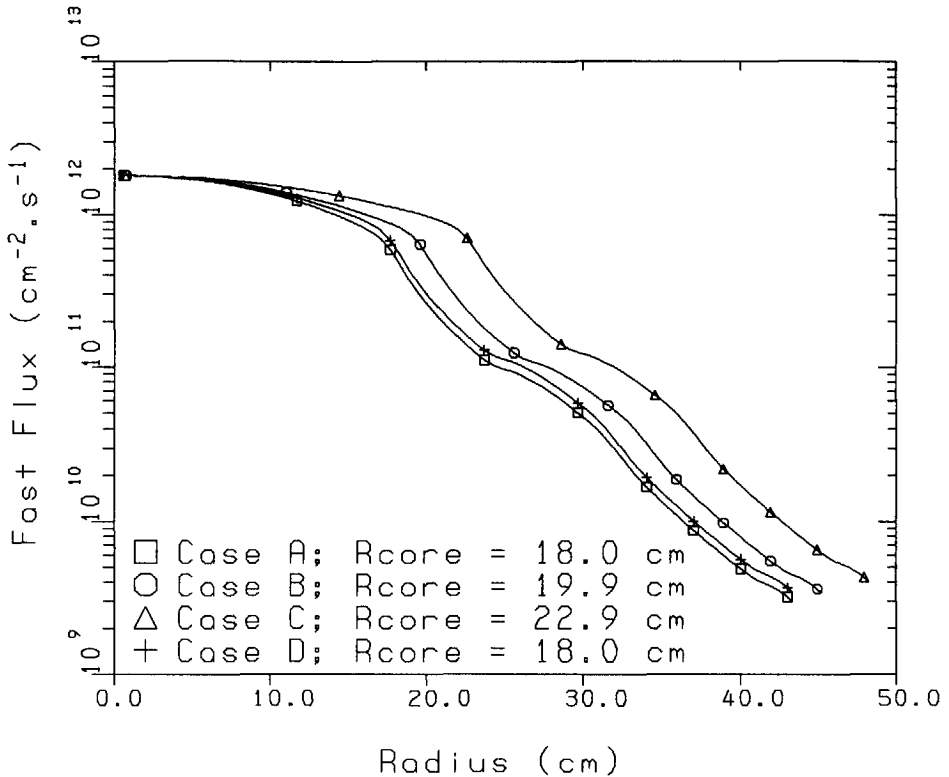


Figure 7.1: Fast fluxes in the core and shield up to the tunnel entrance for several core radii. The last point of each curve is at the tunnel entrance. The fluxes are normalised to the measured fast flux in the core centre obtained from [Zso91].

XSDRNPM-S is a so-called ANISN library, which differs slightly from the format used by DOT3.5 [Rho73] if upscattering is included. In the DOT3.5 format, the total upscattering cross section is present, which is absent in the ANISN format, but which is calculated by ANISN from all partial upscatter cross sections and which is then placed at the end of the library.

Two-dimensional discrete ordinates calculations are carried out by DOT3.5 in P_3S_{48} mode to calculate the angular fluxes at the tunnel entrance. DOT3.5 is suited to this kind of problems, because it makes use of cross section libraries produced by XSDRNPM-S (the microscopic cell calculation for the core cross

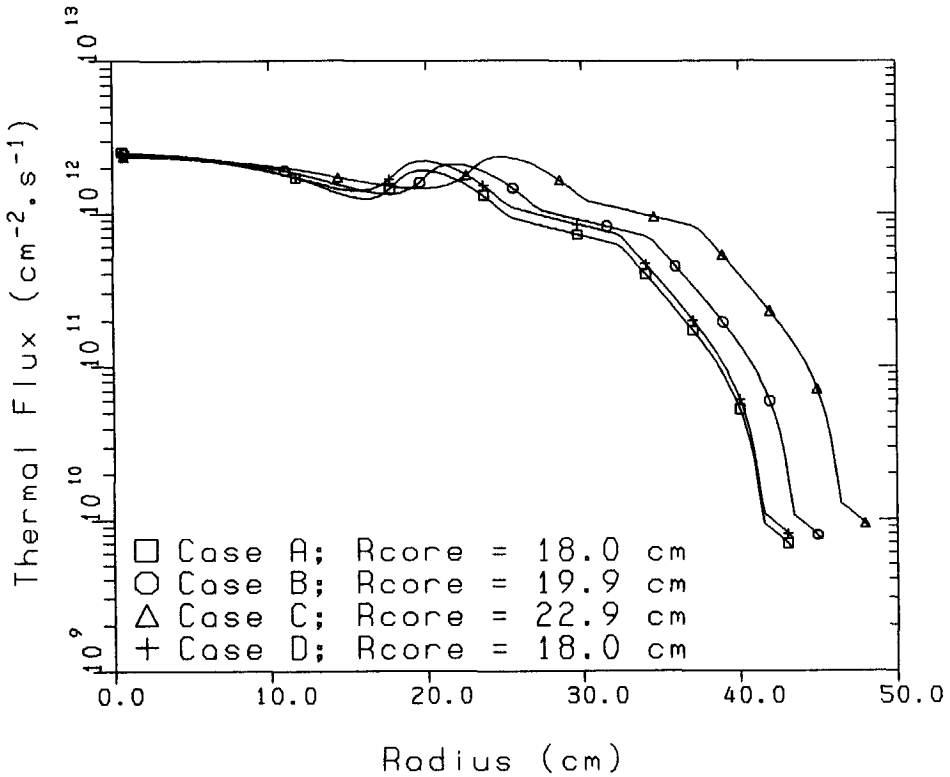


Figure 7.2: Thermal fluxes in the core and shield up to the tunnel entrance for several core radii. The last point of each curve is at the tunnel entrance. The fluxes are normalised to the measured fast flux in the core centre obtained from [Zso91].

sections, the macroscopic cell calculation for the cross sections of the shield layers) and because the calculated angular flux distribution at the tunnel entrance can be converted to a boundary source for the Monte Carlo shielding calculations.

The XY geometry given in Fig. 6.1, is converted to the RZ geometry of Fig. 5.2, to be able to get spatially distributed angular fluxes at the tunnel entrance. The normalisation factor in the DOT3.5 calculations corresponded with a reactor power of 100 kW as in the experiments (see Section 6.4). There are several possibilities to choose the radius of the core: (A) radius equal to

Table 7.2: Calculated and measured fluxes ($\text{cm}^{-2}.\text{s}^{-1}$) at the core centre and tunnel entrance, and the k_{eff} . The differences between the calculations are explained in the text. Both the calculated and measured fluxes are for a reactor power of 100 kW. Measured fluxes from [Zso91].

	R (cm)	Core Centre		Tunnel Entrance		k_{eff}
		ϕ_{fast}	$\phi_{thermal}$	ϕ_{fast}	$\phi_{thermal}$	
Case A	18.0	$1.6 \cdot 10^{12}$	$2.3 \cdot 10^{12}$	$2.7 \cdot 10^9$	$5.8 \cdot 10^9$	1.103
Case B	19.9	$1.5 \cdot 10^{12}$	$2.0 \cdot 10^{12}$	$2.8 \cdot 10^9$	$6.0 \cdot 10^9$	1.047
Case C	22.9	$1.3 \cdot 10^{12}$	$1.7 \cdot 10^{12}$	$2.8 \cdot 10^9$	$6.1 \cdot 10^9$	0.957
Case D	18.0	$1.7 \cdot 10^{12}$	$2.3 \cdot 10^{12}$	$3.3 \cdot 10^9$	$7.1 \cdot 10^9$	1.006
Case E	19.9	$1.3 \cdot 10^{12}$	$1.5 \cdot 10^{12}$	$3.3 \cdot 10^9$	$7.1 \cdot 10^9$	1.001
XY		$1.3 \cdot 10^{12}$	$1.9 \cdot 10^{12}$	$4.3 \cdot 10^9$	$1.1 \cdot 10^{10}$	1.166
Measured		$1.8 \cdot 10^{12}$	$2.7 \cdot 10^{12}$	$4.4 \cdot 10^9$	$1.2 \cdot 10^{10}$	1.000

half width of the core ($R = 18.0$ cm) to get the distance from core centre to the tunnel entrance correct, (B) radius such that the cross sectional area of the core is conserved ($R = 19.9$ cm) to conserve the nuclide densities in the core, and (C) radius such that the perimeter of the core is conserved ($R = 22.9$ cm) to get the leakage area correct. The nuclide densities in case B are equal to the actual ones, while those in cases A and C are higher and lower, respectively, to conserve the total amount of fissionable material in the core. A calculation is also done for case A with nuclide densities equal to those in XY geometry. This case will be denoted by D. All calculations in RZ geometry have an active half core height of 25 cm, and 20 cm of water as a reflector above the core. The bottom boundary condition was reflective to simulate a core with active height of 50 cm.

Several other possibilities to choose the radius of the core could have been used. One is to conserve the buckling to get the leakage correct, which gives a radius of 19.5 cm for unreflected cores. Another possibility would be to conserve the power produced per unit core height. Again for unreflected cores,

this gives according to one-group diffusion theory [Dud76]:

$$\int_{-L/2}^{L/2} \int_{-L/2}^{L/2} \cos\left(\frac{\pi x}{L}\right) \cdot \cos\left(\frac{\pi y}{L}\right) dx dy = \int_0^R J_0\left(\frac{\nu_0 r}{R}\right) 2\pi r dr \quad (7.1)$$

where J_0 is the Bessel function of the first order, and ν_0 is the first zero of this function. This method gives a radius of 19.7 cm. Both radii are almost similar to case B.

Results for the fast ($E \geq 1.0$ MeV) and thermal ($E \leq 0.4$ eV) fluxes are given in Figs. 7.1 and 7.2, respectively, for cases A, B, C and D. The calculated fluxes are normalised to the measured fast flux at the core centre: $\phi_{fast} \approx 1.8 \cdot 10^{12} \text{ cm}^{-2} \cdot \text{s}^{-1}$ obtained from [Zso91]. From these figures it is seen that a larger core seems to lead to higher fluxes at the tunnel entrance. The difference between cases A and D is due to the fact that the optical thickness of the core in case A is higher, which leads to a more peaked power distribution and thus to lower fluxes at the core boundary and the tunnel entrance. Unnormalised fast and thermal fluxes at the core centre and tunnel entrance are given in Table 7.2, together with measured values obtained before [Zso91]. Here it is seen that the fluxes at the tunnel entrance do not change that much as was suggested by Figs. 7.1 and 7.2. From this table, it is also seen that the calculated fluxes do not correspond with the measured values. A calculation in XY geometry was performed, therefore, and the results are also given in Table 7.2. It must be emphasized that this calculation is for a slice of 1 cm core height without leakage in vertical direction. One way to incorporate this leakage would be to enlarge the absorption cross sections by a DB^2 term, where D is the diffusion coefficient and B^2 the buckling in vertical direction, but this is rather unpractical and still approximate because of the introduction of a diffusion coefficient in a discrete ordinates calculation. It is likely that the actual fluxes of the XY calculation at the core centre are slightly higher if the reactor power remains fixed due to a cosine shaped axial flux distribution.

To include the effect of control rods to make the core critical, a new calculation in RZ geometry was done with ^{10}B added to the central core region. Furthermore, some small geometrical changes were made, which had no large effect on the fluxes at the tunnel entrance (some water in the shield was replaced by aluminium, and some carbon by water). The inclusion of ^{10}B lead

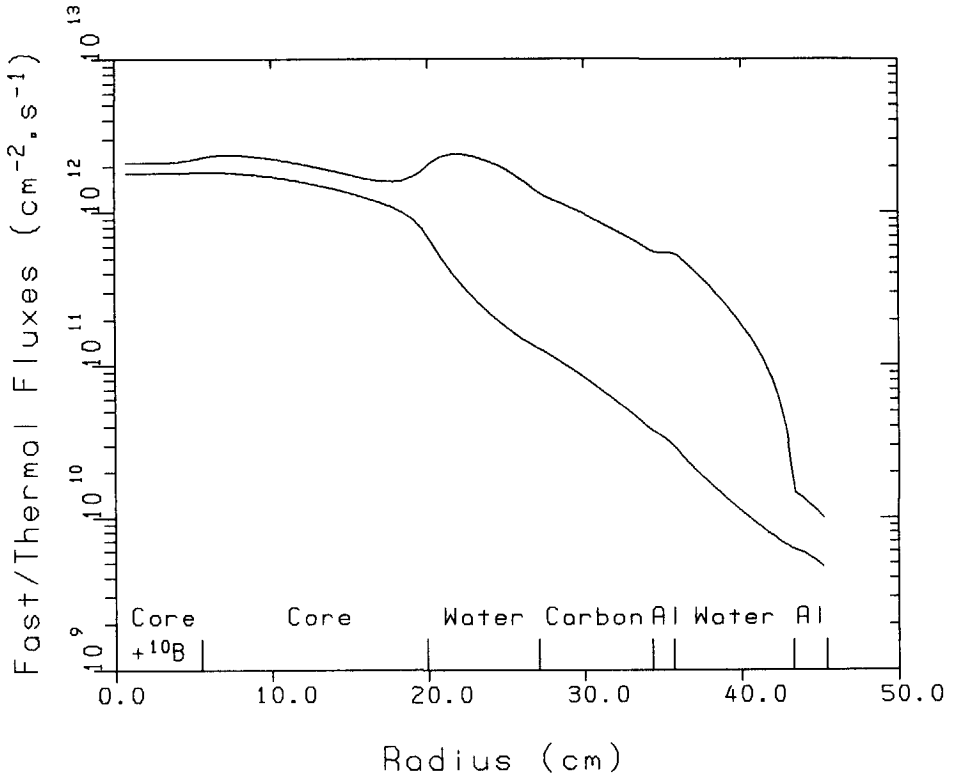


Figure 7.3: Fast flux (lower curve) and thermal flux (upper curve) in the core and shield up to the tunnel entrance, for a calculation with ^{10}B added to the central core region. Both curves are normalised to the measured fast flux in the core centre obtained from [Zso91].

to a flatter flux profile in the core and thus to higher fluxes at the core boundary and tunnel entrance, while the geometrical changes also lead to slightly higher fluxes at the tunnel entrance. The results are again given in Table 7.2 (case E). The fast and thermal fluxes in the core and shield of this calculation are shown in Fig. 7.3, both normalised to the measured fast flux at the core centre. Although the actual flux level is not in correspondence with the measurements, each RZ calculation from Table 7.2 can be used to calculate the source for the Monte Carlo calculations, because the spectra of the RZ calculations at the tunnel entrance are almost equal to each other (the ratio of fast and thermal fluxes at the tunnel entrance, for example, varies only from 0.459 to 0.470 for calculations A till E). The results of calculation E without any normalisation, were used to calculate the boundary source for the Monte Carlo duct streaming calculations.

The total leakages in the XY calculation and in the radial direction of the RZ calculation (case E), are $9.8 \cdot 10^{13} \text{ s}^{-1}$ and $1.17 \cdot 10^{14} \text{ s}^{-1}$, respectively. If it is taken into account that the leakage in case E also includes some leakage from the 20 cm reflector layer above the core (see Fig. 5.2), these two numbers may be rather close to each other.

The angular fluxes for outgoing directions at the tunnel entrance are written to a binary file and converted to a boundary source for the MORSE-SGC/S Monte Carlo code by the DOMINO code [Emm73]. Because both the DOT3.5 and MORSE-SGC/S calculations can be run in forward or adjoint mode, the DOMINO output file can be used as a source or scoring function, dependent on which calculation is in forward mode, and which one in adjoint mode. Here, both DOT3.5 and MORSE-SGC/S are used in forward mode, and the DOMINO output file is used as a source in the Monte Carlo calculations. Because of symmetry reasons, only one half of the core was described by the DOT3.5 calculations. Therefore, a mirror image of the angular flux file was added to the flux file for the bottom half of the core. The angular flux file then obtained is converted to cumulative density functions (CDF), which are used by the MORSE-SGC/S code to sample the source particles. Four CDFs are made by DOMINO: one to sample the energy group, one to sample the spatial interval for a given energy group, one to sample the polar angle for a given spatial interval and energy group, and one to sample the azimuthal angle for a given polar angle, spatial interval and energy group. The final source coordinates are uniformly sampled within the spatial interval, and the

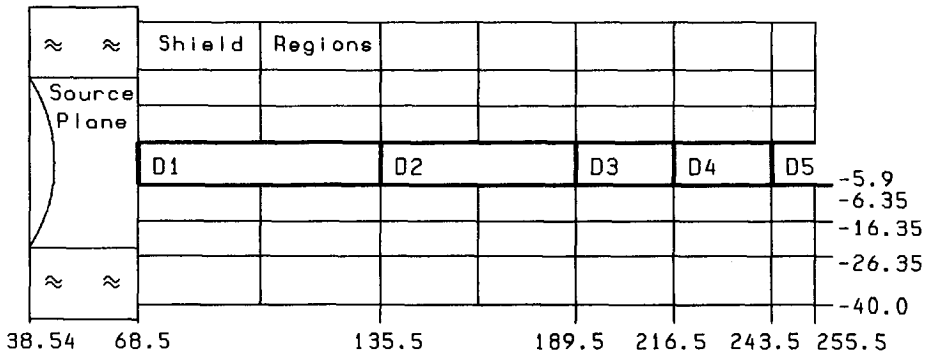


Figure 7.4: Horizontal cross section of the straight duct geometry. The small layer around the duct is steel, the other three layers are concrete, and the waves denote water. Each shield layer is divided in axial direction in regions. D1 to D5 are boundary crossing detectors (in bold). Distances are in cm.

final direction cosines are uniformly sampled within the angular interval. The normalization factor is the total leakage. To make the DOMINO routines, which are used by MORSE, compatible with the newest version of MORSE used here (MORSE-SGC/S), considerable changes to these routines had to be made.

The duct streaming calculations are done by the MORSE-SGC/S Monte Carlo code to get the neutron spectrum at the five detector positions in each duct in Fig. 6.3. A horizontal cross section view of the straight duct geometry is given in Fig. 7.4. Boundary crossing detectors are modelled in the duct on positions D1 to D5. The duct itself is surrounded by a steel liner with thickness of 0.45 cm, and three layers of concrete. The concrete block is rectangular shaped with size (length x width x height) of 187 x 80 x 101 cm³. The second leg of the 30, 60 and 90 degrees bent ducts, is upwardly directed in Fig. 7.4, and starts at the position of the third detector, approximately. The shield around the duct is divided into regions as shown in the figure (a region is a collection of geometrical zones with one set of biasing parameters; a zone is a part of the geometry with homogeneous composition).

The water layer around the tunnel entrance had only an effect on the first detector position. The collided fast flux at this position increased by 10%, while the collided thermal flux increased by a factor of 3, approximately. The

effect of the water on the other detector positions turned out to be negligible.

Although the smallest transversal dimension of the shield (≈ 34 cm) is only 5 mfp for very fast neutrons ($E \geq 4.5$ MeV), this is supposed to be sufficient, because the source neutrons are injected to the shield in axial direction. The system cannot be chosen much larger, anyhow, because of CPU time considerations. Although a Monte Carlo code can principally be used to model three-dimensional geometries accurately, it was found that in fact CPU time considerations limit this possibility. The more different geometrical zones are modelled, the worse the performance of the code. In fact, restrictions on the size of the shield regions are imposed here by this phenomenon.

Several methods to increase the efficiency of the calculations were used to get statistically acceptable results. The efficiency is usually measured by the "Figure of Merit" F :

$$F = \frac{1}{\sigma^2 \cdot T_{cpu}} \quad (7.2)$$

where σ^2 is the variance of the calculation and T_{cpu} the CPU time. From this equation it is seen that not only a variance reduction, but also a CPU time reduction leads to a more efficient calculation. In fact, several methods lead to an increase of the variance per history, but also to a reduction of the CPU time per history. If this latter effect is large enough, the efficiency of the calculation is still increased. The mostly used combination of methods to increase the efficiency of the calculation is survival biasing, Russian roulette and splitting.

The simplest of these methods is survival biasing, which implies that the particle is not allowed to terminate by absorption. Therefore, the weight of the particle is reduced by the non-absorption probability each time it collides. This method is usually default in Monte Carlo codes, because it is easily applied and it can hardly be abused.

To avoid that too much CPU time is spent on particles with negligible weight (and thus negligible detector contribution), Russian roulette can be played. Each time a particle collides with a weight below a value set beforehand (WTLO), a random number is drawn and dependent on that number, the particle survives with a weight set beforehand (WTAV), or it is killed. The survival probability P_{surv} of the particle depends on the weight before collision (WTBC), and the WTAV value of the geometrical region and energy

group the particle is in:

$$P_{surv} = \frac{WTBC}{WTAV} \quad (7.3)$$

Except for statistical deviations, the total weight is conserved in this process. The parameters WTLO and WTAV can be set such that only a small fraction of the particles survive in uninteresting regions of phase space, which can lead to a considerable decrease of the CPU time per source particle, and thus to an increase of the efficiency of the calculation.

A variance reduction device commonly used, is splitting. If the particle collides with a weight above a value set beforehand (WTHI), it is split into two particles with each one half of the initial weight. This may happen for instance if the particle collides in an important region of phase space. Because these two progenies may also be split if their weights are still above WTHI, a large number of progenies may be created from one source particle. This is to be avoided because of the considerable increase of CPU time. Furthermore, the particles scoring in the detector may be correlated, which can lead to a wrong interpretation of the variance.

Another biasing scheme frequently used is exponential transform. The total cross section of the shield is artificially reduced to $\Sigma_t^* = (1 - C)\Sigma_t$, ($0 \leq C < 1$), and the intercollision distance, as sampled from the transport kernel (see Section 1.3), is increased. The parameter C is usually directional dependent in such a way that particles are directed to important geometrical regions, which can be favourable if more particles give a detector contribution. To keep the outcome unbiased, a correction is applied to the weight of the particle, equal to the ratio of the unbiased and biased transport kernels:

$$W_{i+1} = W_i \frac{T(x)}{T^*(x)} = W_i \frac{\Sigma_t \exp(-\Sigma_t x)}{\Sigma_t^* \exp(-\Sigma_t^* x)} = \frac{W_i}{(1 - C)} \exp(-C \Sigma_t x) \quad (7.4)$$

where W_i and W_{i+1} are the original and adapted weights of the particle emerging from collision i , Σ_t is the total cross section of the shield and x is the intercollision distance sampled from the biased transport kernel T^* .

For reasons explained later, boundary crossing estimators were used to calculate the fluxes in the ducts. This made it possible to slightly reduce the variance when exponential biasing was used, by making use of the conditional probability that a particle crossed the detector [Spa69]. The variance of an estimator is composed of two parts: the variance due to the number of particles reaching the detector, and the variance due to the weight of the particles.

In an analog run, no biasing at all is used and the weight of the particles is always unity. If the exponential transform is used, the number of particles reaching the detector is enlarged, which tend to decrease the variance due to the first component. However, the weights of the particles become randomly distributed, which can give rise to an increase of the variance due to the second component. If a particle scores in a boundary crossing detector, the exact intercollision distance is not important, but only the fact that the particle reached the detector. Therefore, it may be profitable to score the expected contribution of a particle crossing the detector, instead of the actual contribution. Instead of scoring W_{i+1} of Eq. (7.4), each time a particle crosses the detector it may be better to score:

$$W'_{i+1} = W_i \exp(-C \Sigma_t D) \quad (7.5)$$

where D is the distance between either the collision or the source and the detector surface. The exponential in Eq. (7.5) is just the ratio of the unbiased and biased probabilities for crossing the detector surface. Both W_{i+1} and W'_{i+1} are unbiased estimators for the particle weight crossing the boundary:

$$\int_D^\infty W_{i+1} \Sigma_t^* \exp(-\Sigma_t^* x) dx = \int_D^\infty W'_{i+1} \Sigma_t^* \exp(-\Sigma_t^* x) dx = W_i \exp(-\Sigma_t D) \quad (7.6)$$

The estimator of Eq. (7.5) was programmed in the MORSE-SGC/S code and used for all calculations. No improvement was found with this estimator for the collided flux contribution, which is to be expected because the weights of the particles in the shield are already very dissimilar, and the distance between the collision and the detector is different for each collision. But the variance of the uncollided contribution decreased by 25%, approximately, which is due to the facts that the distance between the source plane and the detector is more or less constant, and the source particles of a specific energy group have equal weights.

Two variance reduction methods almost similar to each other, are source energy biasing (SEB) and energy biasing at collision sites (EBC). The first method changes the PDF of choosing the energy group of source particles, while the second one changes the PDF of choosing the energy group of particles at collision sites. For SEB, the relative importance of each energy group of the

source region must be given, and the biased source distribution then writes:

$$S_g^* = \frac{S_g I_g}{\sum_{g=1}^G S_g I_g} \quad (7.7)$$

where S_g is the natural source distribution, and I_g is the relative importance of energy group g of the source region. The summation in the nominator is over all energy groups. For EBC, the relative importance of each group and each shield region must be given beforehand, and the biased PDF of choosing an energy group at collision sites is similar to Eq. (7.7) for a particular shield region. The weight correction for both SEB and EBC is equal to the ratio of the original probability and the biased one.

Parameters for Russian roulette, splitting and exponential transform were manually set for the 30, 60 and 90 degrees bent ducts. For the straight duct, use was also made of an automatic biasing procedure, described in Sections 8.2 and 8.3. In all cases, Russian roulette was used to kill particles in uninteresting regions close to the source, while splitting was used to enlarge the number of particles close to detector 5 (see Fig. 7.4). The parameter C of Eq. (7.5) was chosen such that the exponential transform favoured particles travelling along the duct axis in direction of detector 5. The automatic biasing procedure easily allowed the use of SEB and EBC, which favoured fast neutrons above thermal ones.

Despite all these variance reduction devices, it was still cumbersome to calculate the fast neutron flux in the second leg of the 30, 60 and 90 degrees bent ducts. Therefore, calculations with thermal cutoff were performed, which increased the efficiency of the calculations with a factor of two. The variance of the thermal neutron flux in the second leg of the 60 and 90 degrees bent ducts, was rather low, because of many contributions of backscattered neutrons in the ceiling of the tunnel.

It turned out that point detectors, as available in the MORSE-SGC/S code, are not very efficient in large and complicated geometries, because at each collision point an estimate of the detector contribution is made. Collisions far away from the detector require much CPU time while the expected detector contribution is negligible. This can drastically worsen the efficiency of the run. To avoid this, next-event estimation probabilities [Tan88] can be used or other estimators. Here, boundary crossing estimators were used for all

detectors, and each time a particle crossed the detector surface, a score equal to the particle weight according to Eq. (7.5), divided by the absolute value of the cosine of the angle between the particle direction and the normal to the detector surface, was scored. Because the CPU time per source particle is much smaller for boundary crossing detectors than for point detectors, much more particles are tracked and the detector response consists mainly of uncorrelated contributions, which is favourable of course. Finally, the detector response is divided by the cross sectional area of the duct. Because the TLD samples and the foils were not irradiated on the axis of the duct, but 2.5 or 5.0 cm from the duct centreline (see Section 6.1), it is assumed that the calculated responses are comparable with the measured ones.

7.2 Comparison with Measurements

The measured and calculated spectra at position 00.1 are compared with each other in Fig. 7.5, in the 25 groups structure used for the Monte Carlo calculations (see Table 7.1). The fluxes in the 50 groups structure of the SANDBP program were collapsed to these 25 groups, by assuming a constant differential energy flux in each group of the SANDBP group structure. First, it can be observed that the calculated integral flux is lower than the measured one by 30%, approximately. This is not surprising of course, because the flux at the tunnel entrance calculated by DOT3.5 showed already large discrepancies. In Table 7.2, it was already seen that the calculated fast flux at the tunnel entrance (case E) is lower than the measured one by 25%. The size of the discrepancy suggests that the fluxes calculated by DOT3.5 in XY geometry (see Table 7.2) are better than the ones calculated in RZ geometry.

Apart from this discrepancy, it can be seen that the calculated and measured spectra in Fig. 7.5 are similar. As will be shown further in Table 7.4, the calculated ratio of the fast and thermal fluxes ($E \geq 1.0$ MeV and $E \leq 0.4$ eV, respectively) at this position is in agreement with the measured ratio ($\phi_{fast}/\phi_{th} \approx 0.21$). In the fast energy region, the calculated spectrum seems slightly harder than the measured one. It is not clear whether this is significant, and what the reason might be. The calculated spectra at the tunnel entrance in RZ geometry (cases B and E) and XY geometry in Table 7.2, are quite similar for the fast energy region. Because the average energy decrement per elastic scattering for ^{12}C and ^{16}O is only 10 to 15% of the incident neutron

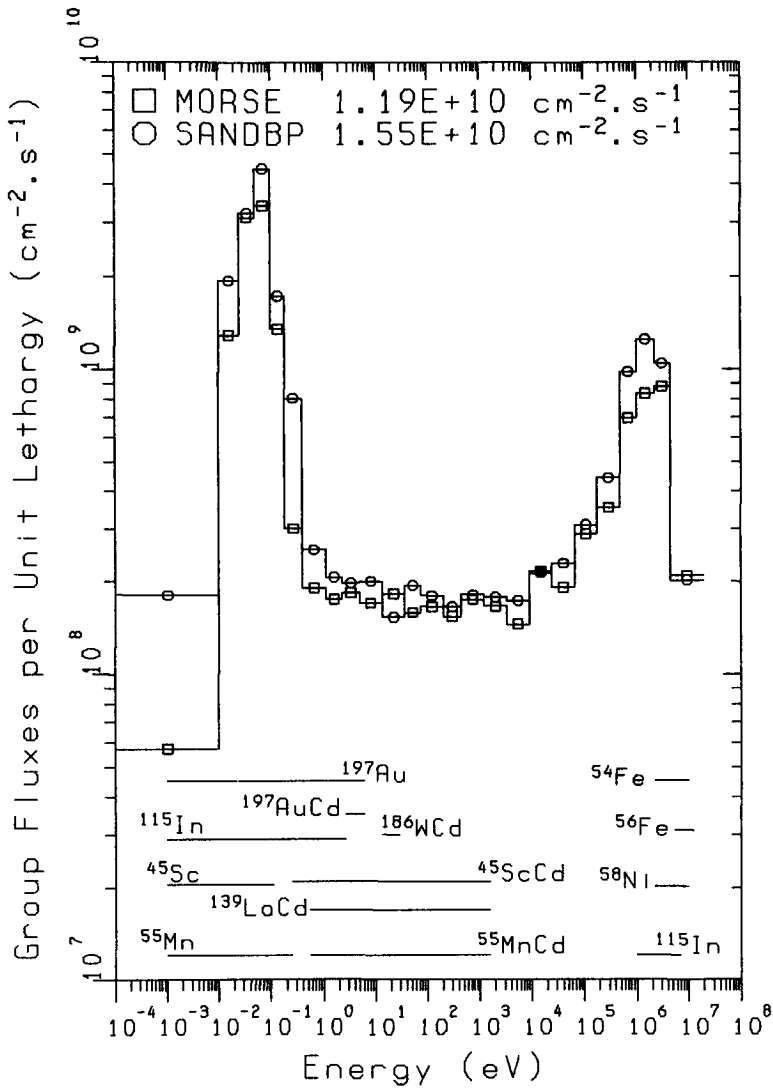


Figure 7.5: Comparison of measured (SANDBP) and calculated (MORSE) spectra at the duct entrance (position 00.1). The bars give the energy response intervals accounting for 90% of the activation. The numbers after MORSE and SANDBP give the integral fluxes.

Table 7.3: Fractional contribution of the uncollided flux for both fast and thermal fluxes obtained from the MORSE calculations. The numbers between parenthesis give the percentage standard deviations (see Appendix B). The calculation marked with an asterisk contains water around the tunnel entrance, the others not.

Position	$\frac{\phi_{th}^{unc}}{\phi_{th}}$	$\frac{\phi_{fast}^{unc}}{\phi_{fast}}$
00.1*	0.32 (3)	0.71 (2)
00.1	0.57 (1)	0.76 (1)
00.2	0.29 (5)	0.48 (5)
00.3	0.60 (6)	0.78 (5)
00.4	0.67 (7)	0.88 (4)
00.5	0.81 (4)	0.90 (4)

energy, and the width of the first energy group is much larger, it was checked whether the selfscatter cross section of the first group is overestimated. One-dimensional calculations with 172 and 25 groups revealed no large differences in flux values, however. Although the calculated flux of the first energy group is relatively too high, its influence on the total fast flux is only modest, because the fluxes of the other fast groups are much higher. From Fig. 7.5 it can be seen that the epithermal flux ($\approx 1-500$ eV) is underestimated by 15%, while the thermal flux is underestimated by 30%, approximately. These discrepancies are most likely to be due to the underestimation of the source strength by the DOT3.5 calculations.

In Fig. 7.6 the calculated and measured spectra at position 00.4 are shown. Comparing these spectra with the ones of Fig. 7.5, it can be seen that the spectrum deep in the duct is considerably hardened. This is mainly due to the fact that the fast flux at the duct entrance is highly forwardly peaked into the duct, while the thermal flux is nearly isotropic (see Fig. 5.3). In Table 7.3 the fractional contribution of the uncollided flux in the straight duct is given. The determination of the error of this fraction is shortly outlined in Appendix B. The value of this fraction is seen to increase in the straight duct. At position 00.4, the uncollided component of the thermal neutron flux contributes for 67%, and of the fast flux even for 88%. Because the fast flux is

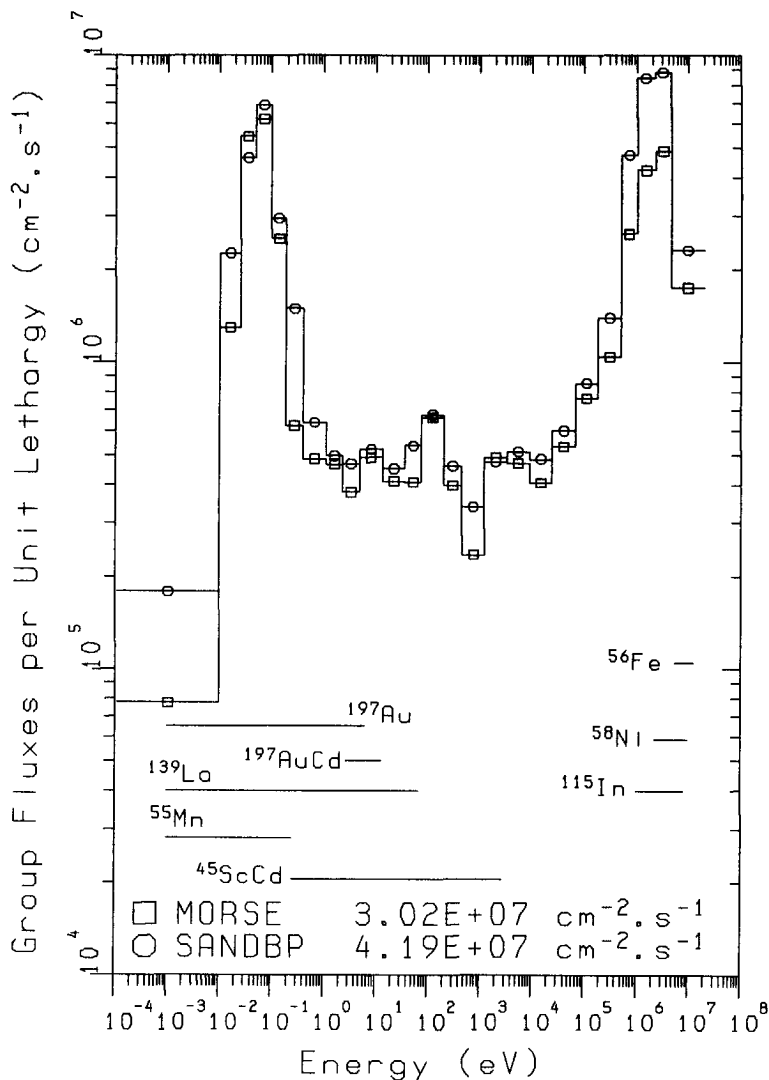


Figure 7.6: Comparison of measured (SANDBP) and calculated (MORSE) spectra deep in the straight duct (position 00.4). The bars give the energy response intervals accounting for 90% of the activation. The numbers after MORSE and SANDBP give the integral fluxes.

more forwardly peaked into the duct than the thermal and epithermal fluxes, the spectrum becomes harder deep in the duct.

Although the calculated integral flux in Fig. 7.6 is again lower by 30%, approximately, the discrepancy at the high energy tail is much larger than for thermal and epithermal energies. Apparently, the fast flux in the duct is underestimated. This can also be deduced from Table 7.4, where the ratios of fast and thermal fluxes in the ducts are given. The determination of the error of the values in this table calculated by MORSE is outlined in Appendix B. For the measurements (SANDBP), values are only given at positions where at least two foils in the fast energy region are used (of which one must be ^{115}In because this foil is sensitive for energies just above 1.0 MeV), and two foils in the thermal energy region. It can be seen that this ratio increases in the straight duct and in the first leg of the bent ducts, for both the calculations (MORSE) and the measurements (SANDBP). The calculated and measured values at the duct entrance agree very well with each other (0.23 and 0.21, respectively), but disagree by 25 to 35% at positions 00.3, 00.4 and 00.5. This is caused by the fact that the angular flow rate distribution at the tunnel entrance, which served as a boundary source in the Monte Carlo calculations, is not correctly represented. It was calculated in a discrete structure of 20 outwardly directed angles, and the initial directions of source particles were uniformly sampled within each angular bin. This can lead to an underestimation of the uncollided flux if the flow rate at the tunnel entrance is in reality highly forwardly peaked. This could have been avoided by using more angles in the DOT3.5 calculations for the source, or by non-uniform sampling of source particles within each angular bin. Unfortunately, the first solution is not very practical because of the increase of CPU time, while the second solution is only possible if more knowledge about the angular distribution is available beforehand.

The calculated and measured reaction rates for the $^{115}\text{In}(n,n')^{115m}\text{In}$ reaction in the straight duct, are shown in Fig. 7.7, together with the C/E values. It can be seen that the C/E value decreases from 0.77 at the duct entrance to 0.54 at the duct exit. A similar decrease of the C/E values in the straight duct is found for the $^{56}\text{Fe}(n,p)^{56}\text{Mn}$ and $^{58}\text{Ni}(n,p)^{58}\text{Co}$ reactions. The C/E values of $^{115}\text{In}(n,n')^{115m}\text{In}$ at the fourth position of the bent ducts (in the second leg) also ranges from 0.5–0.7.

Because the calculated fast flux is attenuated too much in the ducts, the calculated epithermal and thermal fluxes are expected to be overestimated.

Table 7.4: The fraction of the thermal flux due to thermal source neutrons (F_{th}) and the ratio of fast and thermal fluxes in the ducts for both the measurements (SANDBP) and the calculations (MORSE-SGC/S and IRIDUCT). The numbers between parenthesis give the percentage standard deviations (see Appendix B). The calculations marked with an asterisk contain water around the tunnel entrance, the others not.

Position	F_{th} MORSE	ϕ_{fast}/ϕ_{th}					
		SANDBP	MORSE	IRIDUCT			
00.1*	0.83 (1)	0.21	0.23 (3)	0.78			
00.1	0.94 (1)		0.54 (3)				
00.2	0.57 (3)						
00.3	0.81 (3)				1.10	0.75 (6)	0.93
00.4	0.90 (2)				1.18	0.80 (8)	0.97
00.5	0.94 (1)				1.23	0.93 (10)	1.00
30.1*	0.83 (1)	0.22		0.23 (3)	0.78		
30.1	0.94 (1)		0.50 (6)				
30.2	0.53 (4)						
30.3	0.83 (3)			0.70 (8)		0.95	
30.4	0.61 (7)			0.32 (14)		0.72	
30.5	0.40 (14)			0.87 (26)		0.78	
60.1*	0.83 (1)			0.21		0.23 (3)	0.78
60.1	0.94 (1)	0.55 (3)					
60.2	0.53 (4)						
60.3	0.85 (2)		1.02		0.66 (8)	0.95	
60.4	0.36 (15)		0.14 (13)		0.53		
60.5	0.26 (19)		0.15 (18)		0.61		
90.1*	0.83 (1)		0.22		0.23 (3)	0.78	
90.1	0.94 (1)			0.52 (5)			
90.2	0.54 (4)						
90.3	0.85 (2)	1.02			0.55 (10)		0.95
90.4	0.43 (11)	0.10 (15)			0.32		
90.5	0.17 (19)	0.09 (15)			0.27		

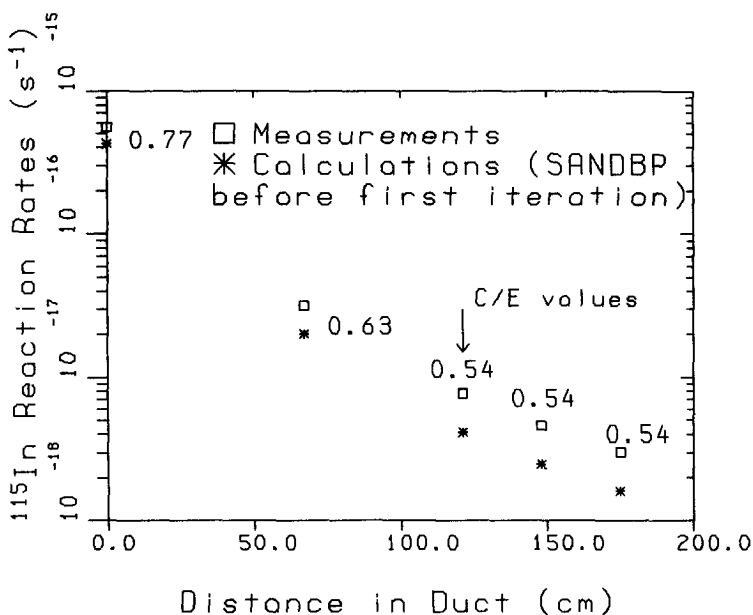


Figure 7.7: Reaction rates for $^{115}\text{In}(n,n')^{115m}\text{In}$ in the straight duct. No uncertainty was assigned to the SANDBP output. The standard deviations of the measurements are about 5%. The inner diameter of the duct is 11.8 cm.

This can be seen in Fig. 7.8, where the $^{55}\text{Mn}(n,\gamma)^{56}\text{Mn}$ reaction rates for both bare and cadmium covered foils in the 30 degrees bent duct are given. Especially the increase of the calculated reaction rates at the second detector position is considerable. From Table 7.3 second column, it is seen that the thermal flux at position 00.2 is due to collided neutrons for 71%. This is much higher than for any other position in the straight duct. Because the contribution of fast neutrons, which thermalize in the concrete of the shielding block before entering the duct (the so-called wall penetrating component), is expected to be largest somewhere between the first and second detector, and because the fast flux in the duct is attenuated too much, which leads to extra thermalized neutrons in the duct, this effect is very significant. In Table 7.4, the fraction of the thermal flux due to thermal source neutrons is given, and it can indeed be seen that this fraction is relatively small at the second detector position of each duct, which confirms that the calculated thermal flux due to downscattered neutrons at these positions is rather large.

The influence of the water layer around the tunnel entrance on the thermal

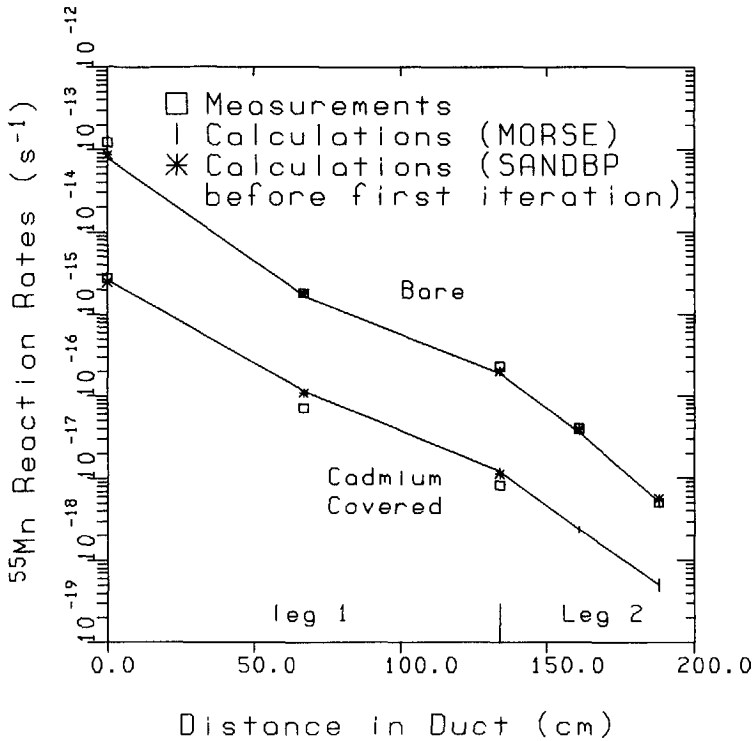


Figure 7.8: Measured and calculated reaction rates for $^{55}\text{Mn}(n,\gamma)$ in the 30 degrees duct. The standard deviation of the measurements is 8%. The vertical bar at each calculation point denotes one standard deviation due to the Monte Carlo process only.

neutron flux at the first detector position, can be seen in Tables 7.3 and 7.4 as well. The contribution of the uncollided flux decreases from 57 to 32% (Table 7.3, second column), while the contribution of downscattered neutrons increases from 6 to 17% (1-0.94 and 1-0.83 in the second column of Table 7.4). From these numbers it is seen that the total thermal flux increases by a factor of 2, approximately, due to the water.

The relative neutron responses of the TLD samples for all geometries are given in Fig. 7.9. The responses are normalised to the response of the first detector of each geometry. The calculated responses were obtained by using the energy sensitivity from the adjoint one-dimensional discrete-ordinates calculation by XSDRNPM-S (see Section 6.2). Again, it can be seen that the

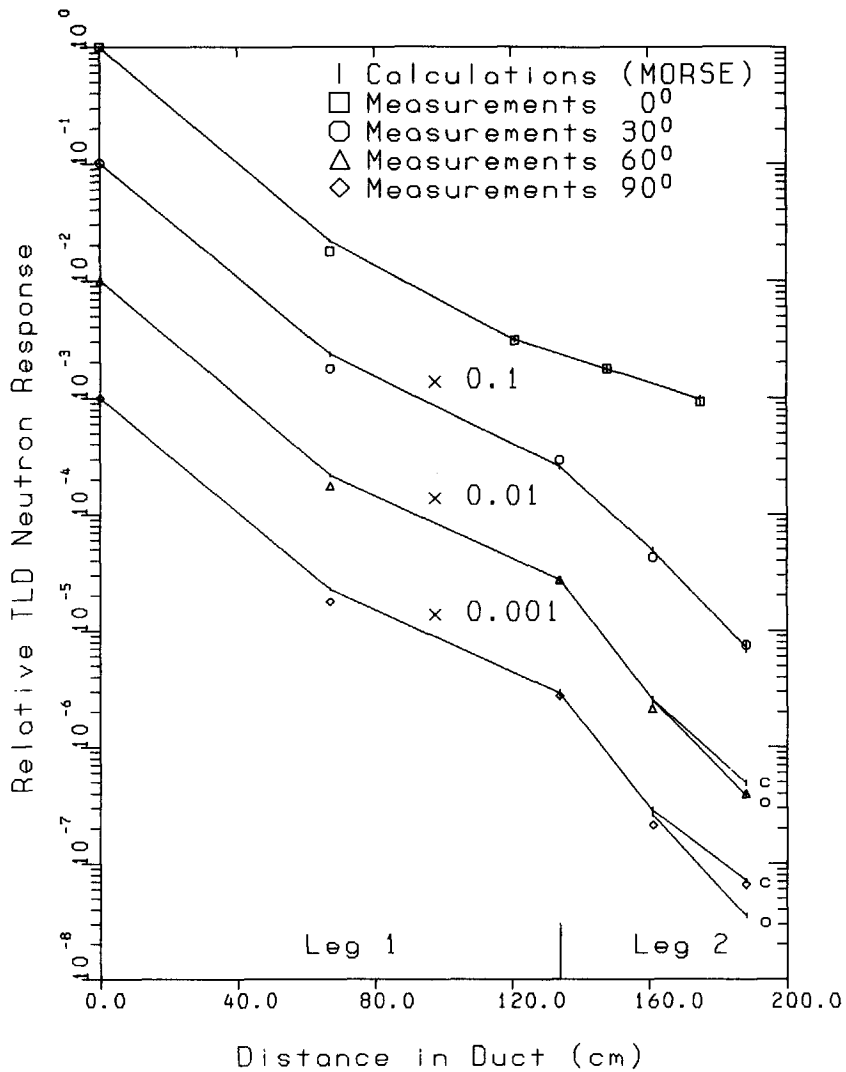


Figure 7.9: Relative TLD neutron responses in the ducts. The standard deviations of the measurements are about 12%. The vertical bar at each calculation point denotes one standard deviation due to the Monte Carlo process only. The two curves for the 60 and 90 degrees ducts are for closed (upper curve) and open (lower curve) ducts.

calculations overestimate the measurements at the second detector positions. For the 60 and 90 degrees ducts, the calculated responses are given for both open and closed ducts. In the second leg of the 60 degrees duct, it is seen that the calculated response in the open duct correspond better with the measured value, while for the 90 degrees duct, the calculated response in the closed duct correspond better with the measured value. This behaviour in the 90 degrees duct seems in contradiction with the results of the $^{45}\text{Sc}(n,\gamma)$, $^{197}\text{Au}(n,\gamma)$ and $^{55}\text{Mn}(n,\gamma)$ reaction rates, which show better agreement with the calculated reaction rates in the open 90 degrees duct. This is shown in Fig. 7.10, which shows the measured and calculated reaction rates for Au and Mn. The fact that the calculated reaction rates in the closed ducts of 90 degrees ducts, overestimate the measured ones, is probably due to an overestimation of the backscattering in the ceiling of the tunnel. The reason for this is not quite clear. Maybe the gap between the shielding blocks and the tunnel ceiling was underestimated (2 cm was used in the calculations), or maybe the hydrogen contents of the concrete was overestimated.

The ratios of calculated fast and thermal fluxes for the bent ducts in Table 7.4 (MORSE), exhibit an interesting behaviour. From positions 00.3, 30.3, 60.3 and 90.3, it is seen that this ratio decreases as the angle of the duct increases. This is due to a higher thermal flux at the end of the first leg if backscattering becomes more important there. More interesting is the behaviour of this ratio in the second leg of the ducts. In the 30 degrees duct, it has still a value of 0.32 and it increases again to 0.87. For the 60 and 90 degrees bent ducts, this ratio is between 0.10 and 0.15 and it does not increase anymore. Although these values are for closed ducts, the same trends can be seen for open ducts. Apparently the fast flux at position 30.3 is more forwardly peaked into the second leg than the thermal flux, which gives an increase of the ratio of fast and thermal fluxes again. In the 60 and 90 degrees bent ducts, the angular distribution of the fast and thermal fluxes at the entrance of the second legs are similar and the ratio of fast and thermal fluxes in the second leg of these ducts hardly changes. There seems to be a critical value for the angle of the bend, below which the fast flux is strongly forwardly peaked into the second leg, while the fast flux is almost isotropically distributed for ducts with angle above this value.

This is what was tried to model in the IRIDUCT program, by use of a single scattering albedo (see Section 5.3). Although the angular flow rate

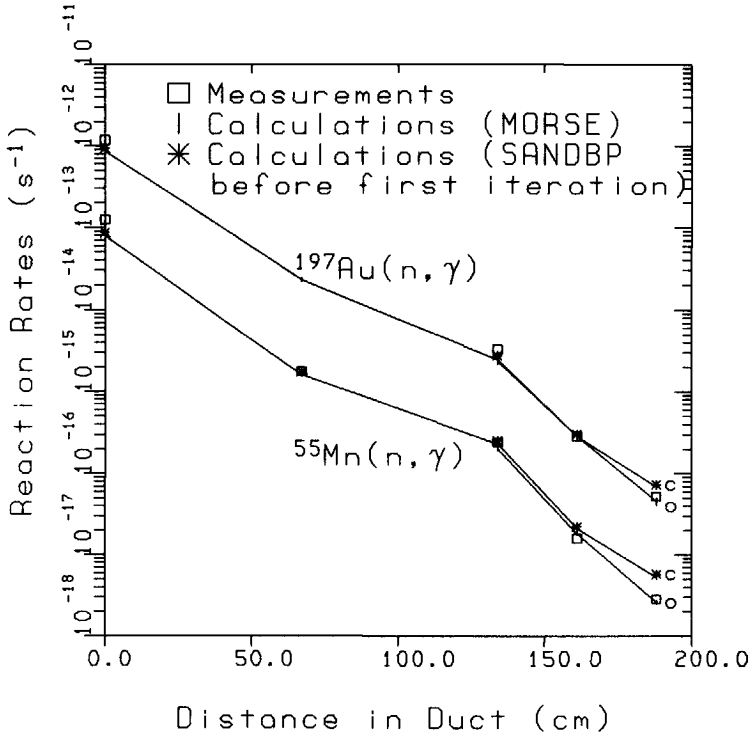


Figure 7.10: Measured and calculated reaction rates for $^{197}\text{Au}(n,\gamma)$ and $^{55}\text{Mn}(n,\gamma)$ in the 90 degrees duct. The two curves for each reaction are for closed (upper curve) and open (lower curve) ducts. The standard deviations of the measurements are 8 and 3% for the Mn and Au, respectively. The vertical bar at each calculation point denotes one standard deviation due to the Monte Carlo process only.

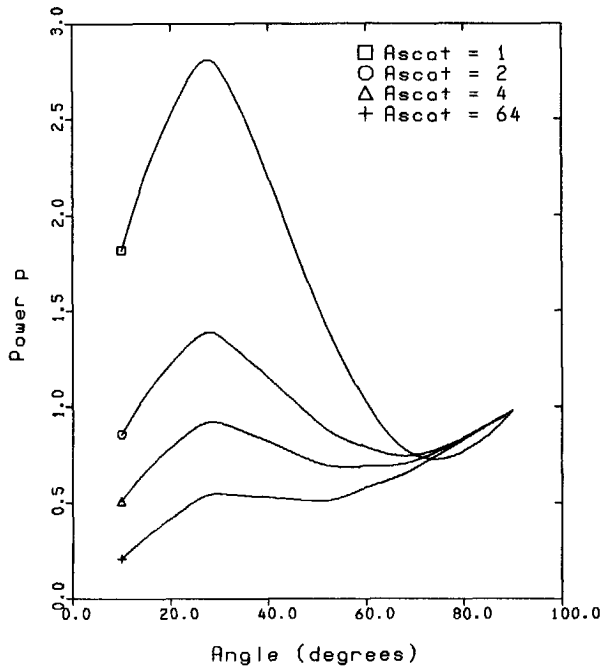


Figure 7.11: The value of p of the angular distribution of the flow rate at the entrance of the second leg of the bent ducts calculated in IRIDUCT, as function of the angle of the duct and the atomic mass of the scatterer.

distribution at the entrance of the second leg is not dependent on energy in IRIDUCT, it is strongly dependent on the angle of the bend. Fig. 7.11 gives the p value of the angular flow rate (see Section 5.3) as a function of the angle and atomic mass of the scatterer. Because the flow rate at the entrance of the second leg is divided into two bins, p first increases because the fraction of the flow rate in the forwardly directed bin ($0.879 \leq \mu \leq 1.0$, with μ being the cosine with respect to the axis of the second leg) increases. After 30 degrees approximately (corresponding with $\mu = 0.879$), p decreases, until the cosine albedo becomes dominant and p increases again to unity. If the atomic mass of the scatterer increases, elastic scattering becomes much less forwardly peaked, which leads to a more isotropic flux. The flow rate with respect to the normal to the reflecting wall becomes cosine shaped in that case, which leads to $p < 1$ for ducts not perpendicular to the wall, because a smaller fraction of the flow rate is directed into the forwardly directed bin in such a case.

The ratios of fast and thermal fluxes calculated by IRIDUCT are also given in Table 7.4. For the straight duct, the values are in agreement with the measurements. In fact they are closer to the measured values than the MORSE ones, which is probably due to the fact that the line-of-sight flux in IRIDUCT is more forwardly peaked, because of the continuous representation of the angular flow rate distribution at the duct entrance (the p values of Fig. 5.3 are used). The values at the fourth and fifth detector positions in the 60 and 90 degrees bent ducts are quite different from the MORSE ones, which is especially due to the fact that the thermal flux in the second leg of these ducts is seriously underestimated by IRIDUCT. Fig. 7.12 gives the dose-equivalent rate in the ducts without backscattering at the end of the second legs, calculated by IRIDUCT and MORSE-SGC/S. It can be seen that the dose-equivalent rate is underestimated by IRIDUCT at the second detector position, which may be due to neglect of the wall penetrating flux and other contributions. In general the agreement is quite satisfactory, which is due to the fact that the fast fluxes are fairly well represented by IRIDUCT, and that the dose-equivalent rate is mainly determined by the fast fluxes.

7.3 Conclusions

To calculate spatially distributed fluxes at the tunnel entrance, two-dimensional discrete ordinates calculations were performed in RZ geometry. It turned out that the conversion from XY to RZ geometry is not straightforward and that considerable errors can be introduced. Criteria usually applied to microscopic cell calculations (fuel cell homogenization) are not applicable to shielding calculations and attention must be put to other functionals, like the flux or flow rate distribution at the outer side of the shield.

The number of angles in the discrete ordinates calculation must be chosen with further use of the calculated flow rate distribution in mind. The flow rate was used here to calculate the streaming through a long duct and an underestimation of the strongly forwardly peaked fast flux in the duct was observed, which made clear that more forwardly directed angles would have been preferable in this case. Because of CPU time considerations, this is not always possible.

The source strength at the tunnel entrance, as calculated by DOT3.5, is too low by 25%, approximately (see Table 7.2). Aside from this underestimation,

the calculated fluxes are in good agreement with the measured ones. Some discrepancies could be accounted for by the angular description of the source in only 20 outwardly directed angles, which lead to an underestimation of the fast flux in the ducts and subsequently to an overestimation of the thermal flux in the ducts. The ceiling of the tunnel at the end of the 60 and 90 degrees bent ducts had quite a large influence on the thermal flux in the second leg of these ducts. Backscattering from the tunnel ceiling was overestimated in the Monte Carlo calculations. The reason for this is not quite clear at the moment.

The results of the IRIDUCT program are in satisfying agreement with the MORSE-SGC/S calculations. It turned out that the use of a single scattering albedo reasonably well reproduces dose-equivalent rates in the second leg of bent ducts.

The results of the TLD measurements are generally in agreement with the foil measurements. The use of TLD samples for thermal neutron flux measurements may be advantageous because the analysis of the TLD samples can be done several weeks after the irradiation (if fading effects are small), and irradiated TLD samples are not radioactive, which facilitates transportation and package. A disadvantage is the sensitivity of the samples to gamma rays, which requires corrections to the measured results. Also the extensive calibration procedure is quite cumbersome, although it has the advantage that each TLD sample can be used several times without a cooling period, which is necessary for some foils. Activation foils can be very advantageous because of their insensitivity to gamma rays and because multiple foils can be used to get more spectral information.

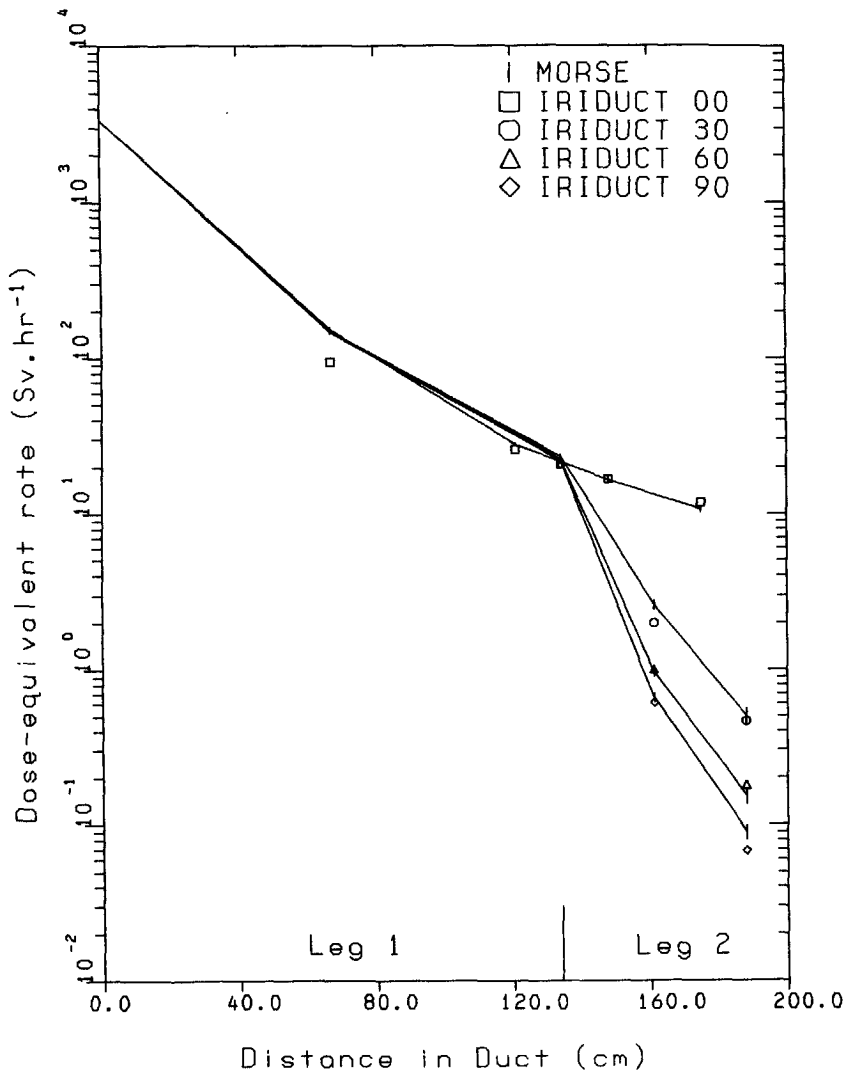


Figure 7.12: Calculated dose-equivalent rates in the open ducts. The vertical bar at each calculation point denotes one standard deviation due to the Monte Carlo process only. The atomic mass of the scatterer is 1.

Chapter 8

Importance Iteration in Monte Carlo Calculations

8.1 Introduction

To enhance the efficiency of Monte Carlo calculations, biasing schemes are used to modify probability density functions (PDF) in Monte Carlo codes, such that important parts of the geometry and energy range are more often sampled, while other parts are scarcely sampled. A biasing scheme which makes use of importance functions is generally called importance sampling or importance biasing. It is well known that properly chosen importance functions can lead to zero variance schemes for last event estimators [Cov67] and collision estimators if the particle is not allowed to terminate [Hoo79]. Although such zero variance schemes are highly theoretical because knowledge of the final solution is required in advance of the Monte Carlo calculation, approximations to the optimum importance functions are likely to reduce the variance in Monte Carlo calculations.

Optimum importance sampling requires knowledge of both the event value, the expected detector response of a particle entering a collision, and the point value, the expected detector response of a particle emerging from a collision or the source. Calculating these value functions exactly and performing a Monte Carlo calculation with biased PDFs is generally less efficient than an unbiased Monte Carlo calculation only. An often employed calculation scheme, therefore, is to calculate point values by use of a one- or two-dimensional discrete ordinates code in an approximate geometry or by use of an approximate calculational method in an exact geometry. If the proper source function is used (see Section 1.3), the point value is equal to the "adjoint flux" in the output of such a code, and this point value can be used to calculate input biasing parameters for the subsequent Monte Carlo calculation. For source energy biasing and energy biasing at collision sites, the optimum importance function is equal to the point value and this function can directly be given in the input of

the Monte Carlo code. For selection of the collision site by use of exponential transform, the event value is the proper importance function, and the point value serves only as an approximation to this function. An extension of this method, therefore, is to calculate the event value by a discrete ordinates code as well, although this function is not part of the standard output of such a code [Tan77].

For some geometries, the above mentioned method to get insight into the value functions of the problem under consideration, fails because of geometrical difficulties like voids and ducts. In case of complex three-dimensional geometries, one- or two-dimensional discrete ordinates codes cannot even be used to get approximate answers to the value functions and other approximate methods or physical insight must be used to bias Monte Carlo calculations properly. One method is to estimate volume averaged value functions in the forward Monte Carlo run itself. These point values can then be used as a biasing function in the next Monte Carlo run to enhance the efficiency of that run. Booth defined the point value in the MCNP Monte Carlo code as the ratio of the total score due to particles and their progenies leaving a cell, and the total weight leaving the cell [Boo82] (or the same definition with particles entering a cell [Boo83]). Section 8.2 describes a method to calculate volume averaged point values and event values in a forward Monte Carlo run. The way to calculate biasing parameters from point values is given in literature [Tan88] and is shortly outlined in Section 8.3. Finally, an example and practical problems and possibilities are described in Section 8.4.

8.2 Calculation of Point Values

The aim of this section is to derive an expression for the point value of a specific geometrical zone and energy group, which can be used in a subsequent Monte Carlo run to set the weight window for that zone and group. The weight window is defined by an upper limit (WTHI) and a lower limit (WTLO) for the particle weight. If the weight of a particle emerging from a collision is larger than WTHI, the particle will be split into two particles with each one half of the original weight. If the particle weight is lower than WTLO, Russian roulette will be invoked, and the particle is killed or it survives with weight WTAV (see Section 7.1). Both WTHI, WTLO and WTAV must be determined beforehand in the input of a Monte Carlo code for each zone and

energy group. If the point value is known for the whole geometry and energy range, the weight window limits of a zone and energy group can be set in correspondence with the point value of that zone and group.

A particle entering a specific zone and group will be killed or split if its weight is outside the weight window. It is likely that this happens only the first time the particle emerges from a collision in that zone and group, because the weight of the particle during all further collisions is only reduced by the non-absorption probability, which is a number fairly close to 1.0 (for concrete the non-absorption probability is larger than 0.93 for all energies ranging from thermal to fast). As the first collision in a specific zone and group is the most important one with respect to Russian roulette and splitting, it makes sense to calculate point values averaged over a zone and group, which are weighted by the firstly emitted particle density. This is the density of particles in a zone and group emitted either from the source or from collisions while their previous collision was in another zone and group.

Point of departure to derive such point values will be the integral transport equations for the emergent particle density $\chi(\mathbf{P})$ and the point value $\chi^*(\mathbf{P})$ (see Section 1.3):

$$\chi(\mathbf{P}) = S(\mathbf{P}) + \int_{\Gamma} \chi(\mathbf{P}')L(\mathbf{P}' \rightarrow \mathbf{P})d\mathbf{P}' \quad (8.1)$$

$$\chi^*(\mathbf{P}) = h(\mathbf{P}) + \int_{\Gamma} \chi^*(\mathbf{P}')L(\mathbf{P} \rightarrow \mathbf{P}')d\mathbf{P}' \quad (8.2)$$

where S is the particle source and h is the detector response function for the emergent particle density. The integration of both equations extends over the whole phase space Γ , which is supposed to consist of two mutually exclusive subspaces Γ_s and Γ_p such that $\Gamma_s + \Gamma_p = \Gamma$. Multiplying each term of Eq. (8.2) by $\chi(\mathbf{P})$ and integrating over Γ_s (the meaning of this subspace will be explained later) yields:

$$\int_{\Gamma_s} \chi(\mathbf{P})\chi^*(\mathbf{P})d\mathbf{P} = \int_{\Gamma_s} \chi(\mathbf{P})h(\mathbf{P})d\mathbf{P} + \int_{\Gamma} \left[\int_{\Gamma_s} \chi(\mathbf{P})L(\mathbf{P} \rightarrow \mathbf{P}')d\mathbf{P} \right] \chi^*(\mathbf{P}')d\mathbf{P}' \quad (8.3)$$

where the integration order of \mathbf{P} and \mathbf{P}' has been reversed in the second term on the RHS. The term between the square brackets on the RHS of Eq. (8.3) is the number of particles emerging from a collision at \mathbf{P}' per unit phase space, which were emitted previously in Γ_s . A shorthand notation for this number will be:

$$\int_{\Gamma_s} \chi(\mathbf{P})L(\mathbf{P} \rightarrow \mathbf{P}')d\mathbf{P} = [\chi(\mathbf{P}')]_{\Gamma_s} \quad (8.4)$$

The second term on the RHS of Eq. (8.3) is now split into two parts:

$$\int_{\Gamma} [\chi(\mathbf{P}')]_{\Gamma_s} \chi^*(\mathbf{P}')d\mathbf{P}' = \int_{\Gamma_s} [\chi(\mathbf{P}')]_{\Gamma_s} \chi^*(\mathbf{P}')d\mathbf{P}' + \int_{\Gamma_p} [\chi(\mathbf{P}')]_{\Gamma_s} \chi^*(\mathbf{P}')d\mathbf{P}' \quad (8.5)$$

Eq. (8.5) is substituted in Eq. (8.3) and the first part of the RHS of Eq. (8.5) is transported to the LHS of Eq. (8.3). One then obtains:

$$\int_{\Gamma_s} (\chi(\mathbf{P}) - [\chi(\mathbf{P})]_{\Gamma_s}) \chi^*(\mathbf{P})d\mathbf{P} = \int_{\Gamma_s} \chi(\mathbf{P})h(\mathbf{P})d\mathbf{P} + \int_{\Gamma_p} [\chi(\mathbf{P})]_{\Gamma_s} \chi^*(\mathbf{P})d\mathbf{P} \quad (8.6)$$

We will now specify the subspace Γ_s as the volume of a geometrical zone Z , the energy span of group G and the whole angular space 4π . To define an average point value for zone Z and group G , Eq. (8.6) is written as:

$$\chi_{Z,G}^* \int_{\Gamma_s} (\chi(\mathbf{P}) - [\chi(\mathbf{P})]_{\Gamma_s}) d\mathbf{P} = \int_{\Gamma_s} \chi(\mathbf{P})h(\mathbf{P})d\mathbf{P} + \int_{\Gamma_p} [\chi(\mathbf{P})]_{\Gamma_s} \chi^*(\mathbf{P})d\mathbf{P} \quad (8.7)$$

or:

$$\chi_{Z,G}^* = \frac{\int_{\Gamma_s} (\chi(\mathbf{P}) - [\chi(\mathbf{P})]_{\Gamma_s}) \chi^*(\mathbf{P})d\mathbf{P}}{\int_{\Gamma_s} (\chi(\mathbf{P}) - [\chi(\mathbf{P})]_{\Gamma_s}) d\mathbf{P}} \quad (8.8)$$

Each term of Eq. (8.7) has a plain physical meaning. $\chi_{Z,G}^*$ is the point value of zone Z and group G , the integral on the LHS is the firstly emitted particle density (the total weight of particles emitted in zone Z and group G , minus the weight of particles emitted previously in zone Z and group G), the first term on the RHS is the expected present detector response of particles emitted in zone Z and group G , and the second term on the RHS is the expected future

detector response of particles emitted in zone Z and group G . From Eq. (8.8) it is seen that $\chi_{Z,G}^*$ is properly weighted by the firstly emitted particle density. Note that the point values thus obtained, are not only averaged over the volume of zone Z and the energy span of group G , but also over the whole angular space 4π . The meaning of these point values is, therefore, very much like the detector response of an isotropic point source with unit strength, as can be deduced from Eq. (1.34). Practically spoken, Eqs. (8.7) and (8.8) read:

$$\chi_{Z,G}^* = \frac{\text{Total detector score of firstly emitted particles in } (Z,G)}{\text{Total weight of firstly emitted particles in } (Z,G)} \quad (8.9)$$

where the score of a progeny of a particle must be added to the score of the parent particle itself. Note that this definition of a zone averaged point value is similar to the ones defined by Booth (see Section 8.1). The same derivation as above can be given for the event value and one obtains:

$$\psi_{Z,G}^* \int_{\Gamma_s} (\psi(\mathbf{P}) - [\psi(\mathbf{P})]_{\Gamma_s}) dP = \int_{\Gamma_s} \psi(\mathbf{P})g(\mathbf{P})dP + \int_{\Gamma_p} [\psi(\mathbf{P})]_{\Gamma_s} \psi^*(\mathbf{P})dP \quad (8.10)$$

where g is the detector response function for the collision density (see Section 1.3) and $\psi_{Z,G}^*$ is the event value of zone Z and group G . The integral on the LHS of Eq. (8.10) is now the firstly collided particle density (the total weight of particles entering a collision in zone Z and group G , minus the weight of particles collided previously in zone Z and group G). The RHS of Eq. (8.10) is again the sum of the expected present and the expected future detector responses of the particles collided in zone Z and group G .

For the calculation of χ^* , the weight of particles emerging from a collision is used as a weighting factor, while for ψ^* the weight of particles entering a collision is used. Because the non-absorption probability is close to one (at least for concrete), the zone averaged point value and event value for a specific energy group will not differ very much. The relation between the event value and the point value outside the detector phase volume in multigroup notation reads [Tan77]:

$$\psi_G^*(\mathbf{r}, \Omega) = \sum_{G'} \int_{4\pi} \frac{\Sigma_s^G(\mathbf{r}) \Sigma_s^{G \rightarrow G'}(\mathbf{r}, \Omega \rightarrow \Omega')}{\Sigma_t^G(\mathbf{r}) \Sigma_s^G(\mathbf{r})} \chi_{G'}^*(\mathbf{r}, \Omega') d\Omega' \quad (8.11)$$

The relation between the angular integrated value functions for a simple one speed problem outside the detector phase volume then reads:

$$\begin{aligned} \psi^*(\mathbf{r}) &= \int_{4\pi} \psi^*(\mathbf{r}, \Omega) d\Omega = \\ &= \int_{4\pi} \int_{4\pi} \frac{\Sigma_s(\mathbf{r})}{\Sigma_t(\mathbf{r})} \frac{\Sigma_s(\mathbf{r}, \Omega \rightarrow \Omega')}{\Sigma_s(\mathbf{r})} \chi^*(\mathbf{r}, \Omega') d\Omega' d\Omega = \frac{\Sigma_s(\mathbf{r})}{\Sigma_t(\mathbf{r})} \chi^*(\mathbf{r}) \end{aligned} \quad (8.12)$$

and the two value functions differ only by the non-absorption probability. When the value functions are calculated by a Monte Carlo code in the way described above, the statistical uncertainties are expected to be much larger than the differences between the two value functions. For practical purposes, therefore, it is sufficient to calculate only one of the two value functions, and to set the event value and point value equal to each other for each zone and group.

The fact that the event value and point value for a specific zone and group are similar, is quite different from the situation described in literature [Tan77], where the angular event value and angular point value along a neutron path differ by one or two orders of magnitude. This is because a neutron entering a collision has a value of $\psi_G^*(\mathbf{r}, \Omega)$, which is related to the point value of the neutron leaving the collision in the same group G and same direction Ω by:

$$\psi_G^*(\mathbf{r}, \Omega) = \frac{\Sigma_s^G(\mathbf{r}) \Sigma_s^{G \rightarrow G}(\mathbf{r}, \Omega \rightarrow \Omega)}{\Sigma_t^G(\mathbf{r}) \Sigma_s^G(\mathbf{r})} \chi_G^*(\mathbf{r}, \Omega) \quad (8.13)$$

The angular event value is thus seen to be much smaller than the angular point value along the same trajectory because of the non-absorption probability and the scattering kernel.

The above mentioned method can easily be implemented in a Monte Carlo code, although this method imposes some restrictions on the number of progenies of a particle and the number of energy groups and zones. For this purpose, the MORSE-SGC/S Monte Carlo code [Wes81a] is used, because of its multigroup energy structure (although no use can be made in this case of the supergrouping facility because of bookkeeping difficulties, so older versions of the MORSE code can be used as well). The weight of each firstly emitted particle is added to a WEIGHT array, which contains the sum of the weights of such particles per zone and group. Note that a particle which emerges from

the source or a collision in zone Z and group G , enters another zone and/or group, scatters to zone Z and group G again and emerges from a collision there, is counted twice. In that case, however, the detector contribution of that particle must be counted twice, too. Therefore, a NUMBER array is bookkept, which contains the number of times a particle contributes this way. Each time a particle or one of its progenies scores in the detector, its score is multiplied by the NUMBER array and added to a SCORE array, which contains the sum of all scores of each zone and group. At the end of the Monte Carlo calculation, the WEIGHT and SCORE arrays are written to a file, which can be read again when the Monte Carlo calculation is restarted. Dividing the elements of the SCORE array by the corresponding elements of the WEIGHT array gives the estimate of the point value of each zone and group, which can be used to bias the PDFs and to calculate the weight window and the exponential transform parameter for each zone and group.

8.3 Calculation of Importance Functions

If the point value is known for each geometrical zone and energy group, the importance functions for biasing Monte Carlo calculations can be calculated [Tan88]. The calculated point values of the source zone can directly be used to bias the PDF for selection of the energy group of the source particles (source energy biasing, see Section 7.1). The point values of each zone of the shield can be used to bias the PDF for selection of the energy group of the particles at collision sites (energy biasing at collision sites, see Section 7.1). Furthermore, the average particle weight for each zone and group (called WTAV $_{Z,G}$) is taken inversely proportional to the point value of that zone and group, which implies that all contributing particles have similar weights. This is likely to reduce the variance of the non-zero contributing particles. This leads to:

$$\text{WTAV}_{Z,G} = \frac{S_G}{S_G^*} \frac{\chi_{S,G}^*}{\chi_{Z,G}^*} \quad (8.14)$$

where S_G and S_G^* are the original and biased PDFs for source energy group selection and $\chi_{S,G}^*$ and $\chi_{Z,G}^*$ are the point values for the source zone S and shield zone Z , respectively. Note that, if no source energy biasing is used, the average weight is just equal to the ratio of the point values of the source region and the shield zone. The weight limits below which Russian roulette will be

invoked (called WTLO) and above which splitting will occur (called WTHI), can be set as a function of the WTAV value in that zone and energy group (e.g. WTLO = 0.1· WTAV and WTHI = 10· WTAV), or as function of the WTAV value of neighbouring zones.

It is shown [Tan88] that the input parameter for exponential biasing can be calculated by fitting an exponential function through the event values as function of the optical thickness from the source region to the detector. For the reason explained earlier, the point value is used here instead of the event value, which does not abuse the method principally. Along the line from source to detector, one obtains for the fitted point value of zone Z and group G :

$$\chi_{Z,G}^* = A \exp \left(C \int_0^D \Sigma_t^G(s) ds \right) \quad (8.15)$$

where D is the distance from the source to the centre of zone Z . For each zone and group, the total cross section and the point value is known, so the fitting parameters A and C can be obtained. This is done by a linear least squares method. Taking the logarithm of Eq. (8.15) and writing $\eta_{Z,G}$ for the optical thickness from the source zone S to shield zone Z , and B for $\ln(A)$, one gets for the sum of squared deviations:

$$\epsilon^2 = \sum_Z \left(\ln(\chi_{Z,G}^*) - B - C \eta_{Z,G} \right)^2 \quad (8.16)$$

where the summation is over each zone along the line from source to detector. Differentiating this equation with respect to B and C , leads to two expressions for these two fitting parameters. C can directly be used as an input parameter for the MORSE-SGC/S code, to bias the transport kernel by exponential biasing (this parameter is called PATH).

As stated before, the point values calculated this way, are likely to suffer from large statistical variations. If it is seen that the point values fluctuate considerably from one energy group to another, they can be smoothed somewhat by collapsing energy groups together. This is done by taking the sum of the SCORE array for these groups and the sum of the WEIGHT array, and using the ratio of these two sums as the average point value for the energy groups collapsed together. In fact, this is the same as taking a weighted average of the point values of these energy groups. If groups G' to G'' are collapsed

together, one obtains for the average point value:

$$\chi_{Z,G}^* = \sum_{IG=G'}^{G''} \left(\frac{W(Z,IG) S(Z,IG)}{\sum_{JG=G'}^{G''} W(Z,JG) W(Z,IG)} \right) = \frac{\sum_{IG=G'}^{G''} S(Z,IG)}{\sum_{IG=G'}^{G''} W(Z,IG)} \quad (8.17)$$

where W and S are shorthand notations for the values of the WEIGHT and SCORE arrays, respectively. The $\chi_{Z,G}^*$ value thus obtained is the same for each energy group ranging from G' to G'' . The validity of this procedure can easily be seen from Eq. (8.7). As the subspace Γ_s can be chosen arbitrarily, it can contain the energy range of several energy groups together instead of only one.

If the point values fluctuate from one zone to another, they can be smoothed by using point values calculated from the fitting parameters A and C in Eq. (8.15). It must be emphasized that the original and smoothed values should be compared carefully, because wrong value functions will only worsen the efficiency of the Monte Carlo calculation instead of improving it.

8.4 Example

The method can best be illustrated by an example. In Fig. 8.1, the geometry of a straight duct in concrete with a 1 cm thick steel liner is shown. A plane source calculated by the DOT3.5 code in 25 energy groups, and converted to MORSE-SGC/S format by the DOMINO code (see Section 7.1), irradiates the duct with length of 100 cm and radius of 5 cm. A boundary crossing detector is positioned at the end of the duct. The importance regions (a region is a collection of geometrical zones with one set of biasing parameters) are concentric around the duct axis and numbered from 1 to 40 (regions 1 to 10 are steel, 11 to 40 concrete).

The first calculation is done by manual setting of biasing parameters (WTAV, WTLO, WTHI and PATH). Neither source energy biasing, nor energy biasing at collision sites are used in this calculation, because of the lack of knowledge of point values. If source energy biasing would have been used, however, the weight windows for all zones and energy groups should have been set in accordance with the weights of the source particles. It is rather cumbersome, however, to give all these parameters in the input. Now, all the biasing

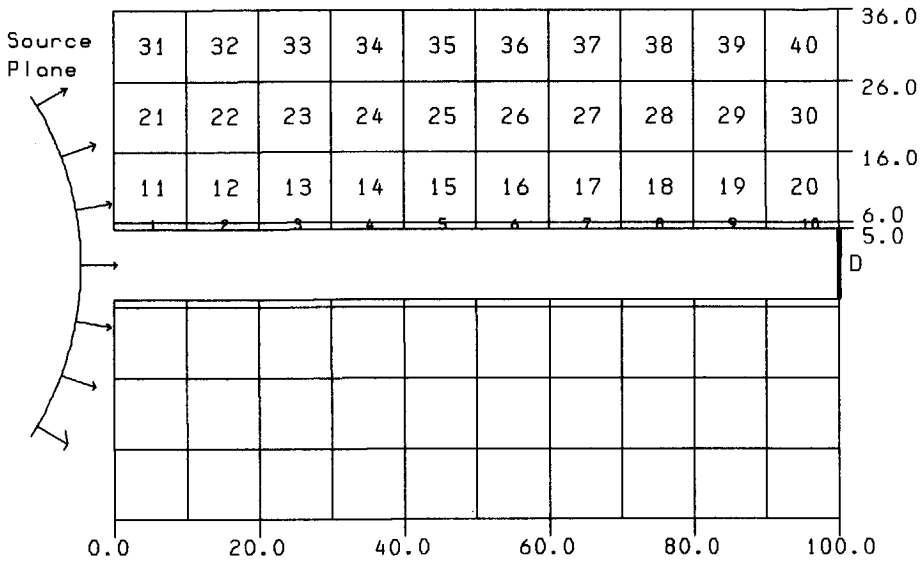


Figure 8.1: Horizontal cross section of a straight duct in concrete with a 1 cm thick steel liner. The regions 1 to 10 are steel, 11 to 40 concrete. The boundary crossing detector is in bold (D), distances in cm.

parameters are the same for each energy group. The WTAV of region 1 is 1.0, and is divided by 2 for each region along the axial direction (thus regions 2, 3 and 4 have WTAV values of 0.5, 0.25 and 0.125, respectively), and multiplied by 2 along the radial direction (thus regions 11, 21, 31 have WTAV values of 2.0, 4.0 and 8.0, respectively). In the first calculation, PATH is 0.5 in axial direction towards the detector for all groups and all zones (note that these values of PATH, and the choices to divide and multiply the WTAV values in axial and radial directions by 2, are quite arbitrary). The second calculation is equal to the first one except for the CPU time, which is about 6 times as large. The third calculation is also equal to the the first one, except that no exponential transform was applied.

The point values from the first calculation were averaged over fast ($E \geq 1.0$ MeV), intermediate ($0.4 \text{ eV} \leq E \leq 1.0$ MeV) and thermal groups ($E \leq 0.4 \text{ eV}$), according to Eq. (8.17), and an exponential fit according to Eq. (8.15) was used to smoothen the spatial behaviour of the point values. The point values for energy groups 3 (1.0–2.23 MeV) and 23 (0.025–0.05 eV) for

the 3 concrete layers are shown in Figs. 8.2 and 8.3, respectively, together with point values obtained from an adjoint one-dimensional discrete ordinates calculation with XSDRNPM-S [Gre83]. For the latter calculation, a 100 cm thick infinite concrete slab without a duct was modelled, with a boundary source at the right boundary. The spectrum and angular distribution of this source correspond with the response of the boundary crossing detector in the forward Monte Carlo calculation, i.e. the inwardly directed adjoint boundary flux at the right hand side of the concrete block in Fig. 8.1 $\phi^*(\Omega)$, given in the input of XSDRNPM-S, was taken proportional to $(\Omega \cdot \mathbf{n})^{-1}$ for each group. The normalization of the source was such that the angular integrated point value calculated this way (the "adjoint flux" in the output of the code) is comparable with the point value calculated in a forward Monte Carlo run $\chi_{Z,G}^*$ (apart from differences due to averaging).

From Figs. 8.2 and 8.3, it is seen that the point values obtained from the XSDRNPM-S calculation are much larger than the MORSE-SGC/S ones. This is due to the fact that the slab and the adjoint source in the XSDRNPM-S calculation are infinitely large, while the radii of the shield and detector in the MORSE-SGC/S calculation are only 36 and 5 cm, respectively. The probability to score in the detector of the one-dimensional system is therefore much larger. It is also seen that the range of the XSDRNPM-S point values is larger than that of the MORSE-SGC/S ones. This is probably due to the presence of the duct in the MORSE-SGC/S calculations.

The plateaus in the point value curves, which seem to appear in concrete layers 1 and 2 (in Fig. 8.2 at 6 mfp, and in Fig. 8.3 at 20 mfp), are due to the spatial and angular characteristics of the source, and to the weighting of the point value with the firstly emitted particle density. They disappear when the source is changed to a point source with the same angular distribution, or when the source is changed to an isotropic boundary source, or when the duct is filled with concrete. A tentative explanation for this phenomenon will be given. The shield is irradiated with a boundary source calculated by DOT3.5, with an angular representation of 8 polar angles and a variable number of azimuthal angles per polar angle (20 solid angle intervals in total). The initial particle direction is uniformly sampled within the solid angle interval determined by the polar and azimuthal angles. The number of source particles can change considerably from one solid angle to the other. It may happen, therefore, that a region is irradiated by particles in a solid angle, which stream for a large part

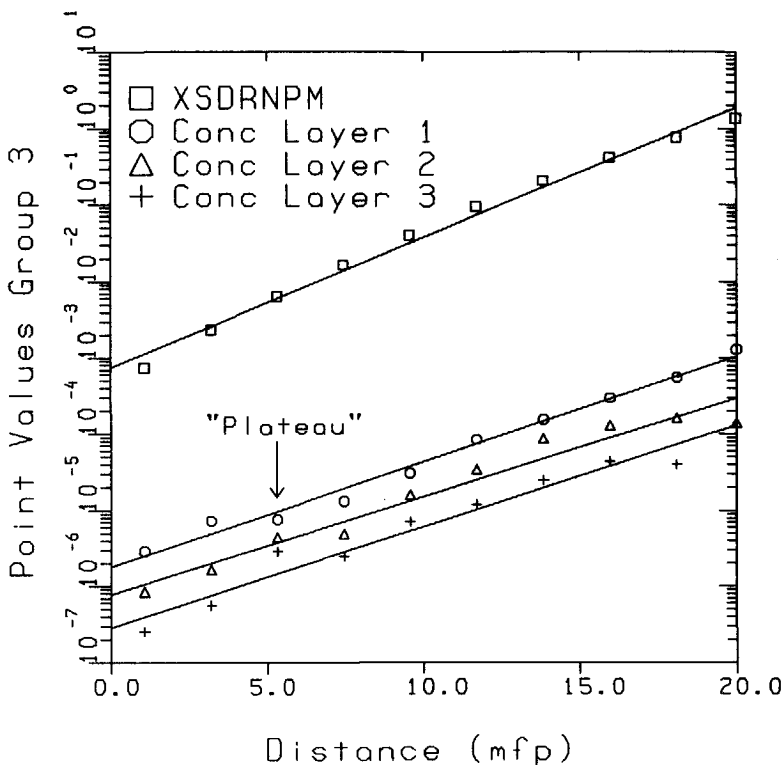


Figure 8.2: Point values for group 3 (1.0–2.23 MeV) as function of the optical shield thickness for both MORSE-SGC/S and XSDRNPM-S calculations, and the linear least squares fit.

through the empty duct. This can lead to a high point value of that region if the beam irradiates mainly the most important part of that region (important with respect to the detector). The region adjacent in axial direction, may be fully irradiated by the beam, which gives a relatively low point value because of self shielding in that region. By means of this ray effect, plateaus in the point value curves can appear.

The point values of the first calculation thus obtained, were used to set the parameters for the weight window, exponential transform, source energy biasing and energy biasing at collision sites of calculations 4 to 9. Because the point values were averaged over fast, intermediate and thermal groups, only

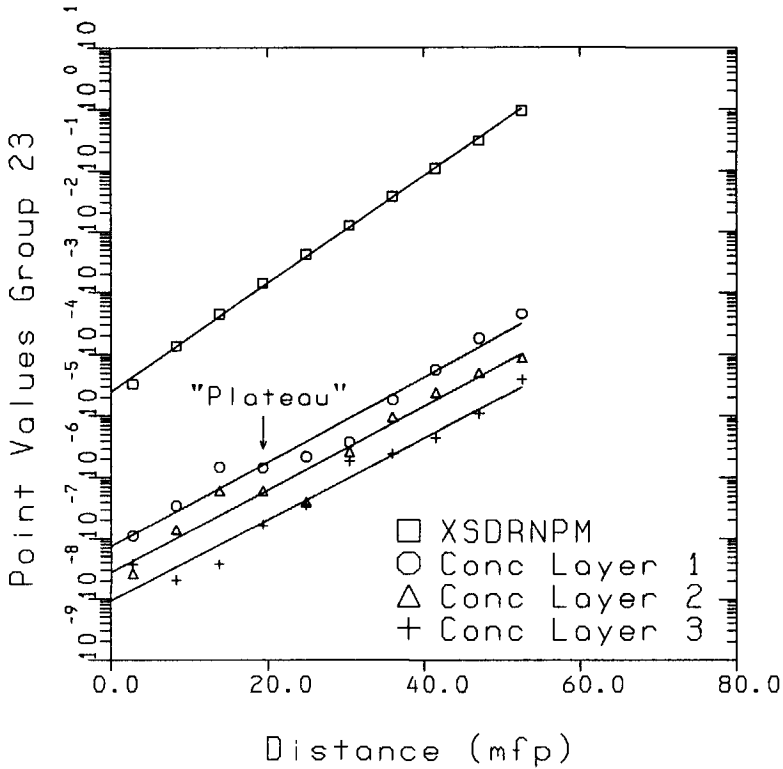


Figure 8.3: Point values for group 23 (0.025–0.05 eV) as function of the optical shield thickness for both MORSE-SGC/S and XSDRNPM-S calculations, and the linear least squares fit.

crude energy biasing could be performed. The values of A in Eq. (8.15) of the point values in the steel liner, were used for the point values of the source particles.

A short overview of all calculations performed, is given in Table 8.1, while the collided fluxes of the calculations are given in Table 8.2. The collided thermal flux due to downscattered fast and intermediate neutrons is given separately in the one but last column of Table 8.2.

From Table 8.2, it is seen that the fast fluxes are calculated much more efficiently in calculations 4, 5 and 6, than in calculation 1 and 3. This is mainly due to source energy biasing and energy biasing at collision sites, which favours

Table 8.1: Biasing parameters for the calculations. The point values for calculations 4 to 9 are obtained from the first calculation and are averaged over fast, intermediate and thermal groups. SEB means source energy biasing, EBC energy biasing at collision sites. Calculations 1 and 2 differ only in CPU time.

Calc	WTAV	WTHI	WTLO	PATH	SEB	EBC
1	input	10	0.1	0.5	no	no
2	input	10	0.1	0.5	no	no
3	input	10	0.1	no	no	no
4	autom.	2	0.5	autom.	autom.	autom.
5	autom.	5	0.2	autom.	autom.	autom.
6	autom.	10	0.1	autom.	autom.	autom.
7	autom.	2	0.5	no	autom.	autom.
8	autom.	5	0.2	no	autom.	autom.
9	autom.	10	0.1	no	autom.	autom.

fast neutrons above others. This leads to undersampling of thermal neutrons, which can be seen from the erratic thermal flux behaviour of calculations 4, 5 and 6. This behaviour is due to thermal source neutrons, which stream through the duct without collisions until they hit the steel liner deep in the duct. Because of the very high weight of thermal source neutrons (≈ 10), and the very low WTAV of the steel liner deep in the duct ($\approx 2 \cdot 10^{-3}$ to $5 \cdot 10^{-3}$ for the thermal groups), an avalanche of highly correlated progenies is created (max. 1024 per source particle), which gives a large contribution to the thermal neutron flux at the end of the duct. Apparently, this streaming path in phase space has a low probability with a high detector contribution, which is not effectively accounted for in the automatic biasing procedure.

It can furthermore be seen that calculations 7, 8 and 9 are even more efficient, although no exponential transform is used. Similar results for spent fuel casks can be found in literature [Cra86], where it is stated that the exponential transform is not effective if the weight window is automatically set from point values calculated beforehand. Maybe this is due to the fact that the weights of particles with stretched path lengths are reduced and a fraction of such particles is killed by Russian roulette in important regions, while the weights

Table 8.2: Collided fast, intermediate, thermal and total fluxes per unit source strength in units of $10^{-7} \text{ cm}^{-2} \cdot \text{s}^{-1}$. The numbers between parenthesis are the percentage standard deviation. The CPU time for each calculation is given in minutes on a VAX3100 M76 workstation. The one but last column gives the thermal flux due to downscattered neutrons only.

Calc	CPU Time	Fast Flux	Interm. Flux	Thermal Flux	Thermal Downsc	Total Flux
1	200	3.6 (30)	4.4 (17)	2.2 (26)	.90 (11)	10.3 (13)
2	1200	2.6 (12)	5.0 (8)	2.5 (10)		10.2 (6)
3	200	2.9 (35)	4.3 (17)	2.3 (26)		9.50 (15)
4	200	2.4 (14)	5.1 (12)	5.8 (73)	.96 (22)	13.3 (32)
5	200	2.1 (17)	4.8 (17)	7.0 (64)	.88 (18)	13.9 (34)
6	200	2.3 (15)	5.3 (14)	1.7 (19)	.77 (14)	9.25 (10)
7	200	1.8 (13)	4.1 (8)	1.4 (21)	.90 (12)	7.37 (7)
8	200	2.3 (14)	4.8 (11)	2.1 (22)	1.2 (25)	9.15 (8)
9	200	2.1 (14)	5.7 (16)	3.4 (30)	1.6 (43)	11.2 (13)

of particles with shrunk path lengths are enlarged and a fraction of these particles is split in less important regions. Another reason might be that the weights of the particles crossing the detector are more randomly distributed when exponential transform is applied (see Section 7.1).

It is not quite clear from Table 8.2, which weight window performs best, as the variances of the calculations are estimates too, which suffer from statistical variations as well. According to literature [Dub86], estimates of percentage standard deviations of 25% and higher might be wrong by as much as 100%. However, there seems to be a tendency that calculations with smaller weight windows (calculations 4 and 7) are slightly more efficient than their counterparts with larger weight windows (calculations 5, 6 and 8, 9)

8.5 Conclusions

To improve the efficiency of Monte Carlo calculations, knowledge of the important parts of the shield and energy range is necessary, to bias the Monte

Carlo calculations properly. The point values per zone and energy group can be estimated from a forward Monte Carlo run, and it is shown that the efficiency of a Monte Carlo run can be improved if these point values are used in subsequent runs. It is also shown, however, that some channels in phase space may be undersampled, which can lead to an erratic behaviour of the variance. Each time a particle is sampled in these scarcely sampled phase space channels, it will give a large detector contribution and the mean detector contribution and the variance of the calculation will increase significantly. If the calculation is stopped before any particles are sampled in these phase space channels, the detector response may be underestimated and the variance may be artificial low. To avoid this, care must be taken to ensure that such phase space channels are sampled frequently enough.

To smoothen the point values estimated in a first Monte Carlo run, over energy and space, considerable programming is necessary, which depends on the problem under consideration, and which requires a thorough knowledge of the code used. A considerable portion of this programming can be avoided by using only energy averaged point values. Care must be taken in this case to ensure that the point values are non-zero for each region.

A general applicable, fully automatized biasing procedure, is difficult to establish because of the above mentioned problems. It is also questionable whether the lower CPU times compensate for the extra input preparation time in view of the relative cheap CPU time nowadays. If a long sequence of Monte Carlo runs is to be done, however, with only slight input differences, it may be profitable to use point values from the first run(s) to enhance the efficiency of the following ones.

Bibliography

- [Alc86] R.E. Alcouffe and R.D. O'Dell
Transport Calculations for Nuclear Reactors.
CRC Handbook of Nuclear Reactors Calculations, Volume I.
CRC Press, Inc, Boca Raton, Florida, USA, 1986
- [Bar88] P. Barbucci, G. Mariotti, N. Cerullo, P. Riscossa, A. Cesana, M. Ter-rani and G. Sandrelli
Neutron Spectral Analysis of the Caorso Boiling Water Reactor Cavity and Sacrificial Shield Penetrations and Comparisons with the Irradiation Experiment Results.
Nucl. Sci. Eng. **100**, 467-478 (1988)
- [Bar91] D.A. Barnett
Benchmark Measurements and Calculations of a Three-Dimensional Neu-tron Streaming Experiment.
Proc. Advances in Mathematics, Computations and Reactor Physics
Pittsburg, USA, April 28 - May 2, 1991
- [Blu82] P. Blum, R. Cagnon and J.C. Nimal
Expérience de Référence (Benchmark) pour la Qualification des Méthodes de Calcul du Blindage Gamma des Emballages pour Combustible Irradié en Provenance des Centrales Nucleaires a Eau Légère.
Report EUR 8017 FR, 1982
- [Bol87] V.V. Bolyatko, M.Yu. Vyrskii, A.I. Ilyushkin, G.N. Manturov, V.P. Mashkovich, M.N. Nikolaev, V.K. Sakharov and A.P. Suvorov
Error Estimation in Reactor Shielding Calculations.
American Institute of Physics, New York, 1987
- [Boo82] T.E. Booth
Automatic Importance Estimation in Forward Monte Carlo Calculations.
Trans. Am. Nucl. Soc. **41**, 309-310 (1982)

- [Boo83] T.E. Booth
A Weight Window/Importance Generator for Monte Carlo Streaming Problems.
Proc. of Sixth International Conference on Radiation Shielding, Tokyo, Japan, May 16-20, 1983
- [Bos92] A.J.J. Bos and T.M. Pijters
Success and Failure of the Randall-Wilkins model for Thermoluminescence in LiF (TLD).
Proc. of Tenth Solid State Dosimetry Conference, Washington, U.S.A., July 13-17, 1992, to be published in Rad. Protec. Dosim.
- [Cai77] V.R. Cain
QAD-CG, the Combinatorial Geometry Version of the QAD-P5A Point Kernel Shielding Code.
Bechtel Computer Code NE007, July 1977
- [Chi88] R.L. Childs, W.A. Rhoades and L.R. Williams
Three-Dimensional Calculations of Neutron Streaming in the Beam Tubes of the ORNL HFIR Reactor.
Proc. of Seventh International Conference on Radiation Shielding, Bournemouth, U.K., September 12-16, 1988
- [Chi80] A.B. Chilton, C.M. Eisenhauer and G.L. Simmons
Photon Point Source Buildup Factors for Air, Water and Iron.
Nucl. Sci. Eng. **73**, 97 (1980)
- [Chi84] A.B. Chilton, J.K. Shultis and R.E. Faw
Principles of Radiation Shielding.
Prentice-Hall inc., Englewood Cliffs, New Jersey 1984
- [Cov67] R.R. Coveyou, V.R. Cain and K.J. Yost
Adjoint and Importance in Monte Carlo Application.
Nucl. Sci. Eng. **27**, 219-234 (1967)
- [Cra86] S.N. Cramer, J. Gonnord and J.S. Hendricks
Monte Carlo Techniques for Analyzing Deep Penetration Problems.
Nucl. Sci. Eng. **92**, 280-288 (1986)

- [Cuc87] E. Cuccoli, G.C. Panini and F. Siciliano
A 219 Neutron Group Set from JEF-1 in the AMPX Master Library Interface Format.
Centro-di-Calcolo del ENEA, Bologna, Italy, May 1987
- [Cul85] D.E. Cullen and P.K. McLaughlin
The International Reactor Dosimetry File (IRDF-85).
Report IAEA-NDS-41, Rev. 1, April 1985
- [Dev74] C. Devillers and C. Dupont
MERCURE-IV, un Programme de Monte Carlo a Trois Dimensions pour l'Integration de Noyaux Ponctuels d'Attenuation en Ligne Droite.
Note CEA-N-1726, April 1974
- [Dio89] C.M. Diop, J.C. Nimal, P. Blum and R. Cagnon
TN12 Shipping Cask Computational Benchmark.
Report NEACRP-A-961, January 1989
- [Dub79] A. Dubi
On the Analysis of the Variance in Monte Carlo Calculations.
Nucl. Sci. Eng. **72**, 108-110 (1979)
- [Dub86] A. Dubi
Monte Carlo Calculations for Nuclear Reactors.
CRC Handbook of Nuclear Reactors Calculations, Volume II.
CRC Press, Inc, Boca Raton, Florida, USA, 1986
- [Dud76] J.J. Duderstadt and L.J. Hamilton
Nuclear Reactor Analysis.
John Wiley&Sons, 1976
- [Eng66] R.L. Engel, J. Greenborg and M.M. Hendrickson
ISOSHL, a Computer Code for General Purpose Isotope Shielding Analysis.
Report NBWL-236, June 1966
- [Emm73] M.B. Emmet, C.E. Burgart and T.J. Hoffman
DOMINO, a General Purpose Code for Coupling Discrete Ordinates and Monte Carlo Radiation Transport Calculations.

Oak Ridge National Laboratory, Oak Ridge, Tennessee, USA
Report ORNL-4853, July 1973

- [Gol54] H. Goldstein and J.E. Wilkins
Calculations of the Penetrations of Gamma Rays.
United States Atomic Energy Commission, Report NYO-3075, 1954
- [Gre81] N.M. Greene
BONAMI-S: Resonance Self-Shielding by the Bondarenko Method.
Oak Ridge National Laboratory, Oak Ridge, Tennessee, USA
Report NUREG/CR-0200, Volume 2, Section F1, October 1981
- [Gre83] N.M. Greene and L.M. Petrie
XSDRNPM-S, A One-Dimensional Discrete Ordinates Code for Transport
Analysis.
Oak Ridge National Laboratory, Oak Ridge, Tennessee, USA
Report NUREG/CR-0200, Volume 2, Section F3, June 1983
- [Her84] O.W. Hermann and R.M. Westfall
ORIGEN-S, Scale System to Calculate Fuel Depletion, Actinide Trans-
mutation, Fission Product Buildup and Decay, and Associated Radiation
Source Terms.
Oak Ridge National Laboratory, Oak Ridge, Tennessee, USA
Report NUREG/CR-0200, Volume 2, Section F7, December 1984
- [Hoo79] J.E. Hoogenboom
Optimum Biasing of Integral Equations in Monte Carlo Calculations.
Nucl. Sci. Eng. **70**, 210-212 (1979)
- [JEF85] Index to the JEF-1 Nuclear Data Library.
Report JEF-1, NEA Data Bank, September 1985
- [Klo88] J.L. Kloosterman
MARMER, a Flexible Point-Kernel Shielding Code.
Proc. of Seventh International Conference on Radiation Shielding,
Bournemouth, U.K., September 12-16, 1988
- [Klo89a] J.L. Kloosterman
Introductory Analysis of Neutron and Gamma Ray Streaming through

Ducts and Gaps in Shields of Nuclear Reactors.
Report IRI-131-89-04, September 1989

- [Klo89b] J.L. Kloosterman
Gamma Benchmark Calculations on the TN12 Spent Fuel Shipping Cask.
Report IRI-131-89-11, November 1989
- [Klo90a] J.L. Kloosterman
MARMER, a Flexible Point-Kernel Shielding Code.
Report IRI-131-89-03/2, June 1990
- [Klo90b] J.L. Kloosterman and J.E. Hoogenboom
Gamma Benchmark Calculations on the TN12 Spent Fuel Shipping Cask
by the Point-Kernel Shielding Code MARMER.
Proc. of European Nuclear Conference '90, Lyon, France, September 23-28,
1990
- [Klo90c] J.L. Kloosterman and J.E. Hoogenboom
MARMER, A Flexible Point-Kernel Shielding Code.
RAMTRANS, Vol. 1, pp 117-125 (1990)
- [Klo92] J.L. Kloosterman
Gamma Ray Buildup Factor Calculations for Iron by the one-dimensional
Discrete Ordinates Code XSDRNPM-S.
Ann. Nucl. Energy, Vol. 19, No 2, pp 105-114, 1992
- [Kni78] J.R. Knight and R.M. Westfall
DOSE: AMPX Module for Producing Neutron and Gamma Ray Dose Fac-
tors.
Oak Ridge National Laboratory, Oak Ridge, Tennessee, USA
Report ORNL-TM-3706, December 1978
- [Koc90] N.P. Kocherv and P.K. McLaughlin
The International Reactor Dosimetry File (IRDF-90).
Report IAEA-NDS-141, Rev. 0, August 1990
- [LeD59] J.C. LeDoux and A.B. Chilton
Gamma Ray Streaming through Two-Legged Rectangular Ducts.
Nucl. Sci. Eng. 11, 362-368 (1959)

- [Mac87] R.E. MacFarlane, D.W. Muir and R.M. Boicourt
NJOY87, A Code System for Producing Pointwise and Multigroup Neutron
and Photon Cross Sections from ENDF/B Evaluated Nuclear Data.
Los Alamos National Laboratory, Los Alamos, New Mexico, USA
Report PSR-171, 1987
- [Mik77] W.J. Mikols and J.K. Shultis
Selection of Angular Quadrature for Anisotropic Transport Computations.
Nucl. Sci. Eng. **63**, 91-109 (1977)
- [Mil83] P.C. Miller
RANKERN, a Point Kernel Integration Code for Complicated Geometry
Problems.
Proc. of Sixth International Conference on Radiation Shielding, Tokyo,
Japan, May 16-20, 1983
- [Miu81] T. Miura, T. Fuse and N. Yamano
Experiments on Neutron Transport through Annular Duct of Large Radius.
J. Nucl. Sci. Techn. **18** [5], 369-386 (May 1981)
- [Miu83] T. Miura and N. Sasamoto
Experimental Study of Neutron Streaming through Steel Walled Annular
Ducts in Reactor Shields.
Nucl. Sci. Eng. **83**, 333-349 (1983)
- [Miu89] T. Miura
Empirical Formulas of Neutron Flux Distributions in Cylindrical Ducts in
Water or Concrete Shields.
Nucl. Sci. Eng. **102**, 191-209 (1989)
- [Num88] S. Numata, A. Yamaji and T. Saito
Shielding Experiment for Gamma Ray Streaming through Two-Legged
Concrete Duct and Analysis by Single Scattering Method.
J. Nucl. Sci. Techn. **25** [1], 19-31 (January 1988)
- [Oka86] Y. Oka, C. Tsukishima, H. Hashikura, M. Akiyama and S. Kondo
Neutron Streaming through Narrow and Long Annulus.
J. Nucl. Sci. Techn. **23** [5], 387-394 (May 1986)

- [Pon74] C. Ponti and R. van Heusden
SABINE-3, an Improved Version of the Shielding Code SABINE.
European Shielding Information Service, 1974
- [Pri57] B.T. Price, C.C. Horton and K.T. Spinney
Radiation Shielding.
Pergamon Press, 1957
- [Rho73] F.R. Mynatt, W.W. Engle jr., M.L. Gritzner, W.A. Rhoades and R.J. Rodgers
The DOT III Two-Dimensional Discrete Ordinates Transport Code.
Oak Ridge National Laboratory, Oak Ridge, Tennessee, USA
Report ORNL-TM-4280, September 1973
- [Roc56] T. Rockwell III
Reactor Shielding Design Manual.
D. van Nostrand Company Inc, 1956
- [Rou79] R.W. Roussin, C.R. Weisbin, J.E. White, N.M. Greene, R.Q. Wright and J.B. Wright
VITAMIN-C, the CTR Processed Multigroup Cross Section Library for Neutronics Studies.
Oak Ridge National Laboratory, Oak Ridge, Tennessee, USA
Report ORNL/RSIC-37, July 1979
- [Sch73] N.M. Schaeffer
Reactor Shielding for Nuclear Engineers.
U.S. Atomic Energy Commission, Office of Information Service, 1973
- [Shi82] K. Shin, R. Murakami, H. Taniuchi and T. Hyodo
Measurements of Neutron and Gamma Ray Streaming in a Cavity Duct System and Analysis by an Albedo Monte Carlo Method.
Nucl. Sci. Eng. **81**, 161-171 (1982)
- [Shi84] K. Shin and T. Hyodo
Applicability of Albedo Concept to Neutron Streaming through Small Ducts and Slits.
Proc. of Sixth International Conference on Radiation Shielding, Tokyo, Japan, May 16-20, 1983

- [Shi89] K. Shin
Evaluation Formula for Radiation Duct Streaming.
J. Nucl. Sci. Techn. **26** [12], 1067-1080 (December 1989)
- [Shu79] K. Shure
Gamma Ray Dose Rate Conversion and Buildup Factors.
Nucl. Sci. Eng. **69**, 432 (1979)
- [Sim56] A. Simon and C.E. Clifford
The Attenuation of Neutrons by Air Ducts in Shields.
Nucl. Sci. Eng. **1**, 156-166 (1956)
- [Spa69] J. Spanier and E.M. Gelbard
Monte Carlo Principles and Neutron Transport Problems.
Addison-Wesley Publishing Company, 1969
- [Su83] S. Su and B.A. Engholm
PATH, a Flexible Gamma Shielding Design Tool.
Proc. of Sixth International Conference on Radiation Shielding, Tokyo,
Japan, May 16-20, 1983
- [Tak85] K. Takeuchi and S. Tanaka
Point Isotropic Buildup Factors of Gamma Rays, Including Brems-
strahlung and Annihilation Radiation for Water, Concrete, Iron and Lead.
Nucl. Sci. Eng. **90**, 158 (1985)
- [Tan77] J.S. Tang, T.J. Hoffman and P.N. Stevens
Monte Carlo Shielding Calculations Using Event Value Path Length Bias-
ing.
Nucl. Sci. Eng. **62**, 617-626 (1977)
- [Tan88] J.S. Tang and T.J. Hoffman
Monte Carlo Shielding Analysis Using an Automated Biasing Procedure.
Nucl. Sci. Eng. **99**, 329-342 (1988)
- [Tra78] Radiation Streaming in Power Reactors.
Trans. Am. Nucl. Soc. **30**, 233-239 and 610-617 (1978)
- [Tru88] D.K. Trubey
New Gamma Ray Buildup Factor Data for Point Kernel Calculations:

ANS-6.4.3 Standard Reference Data.

Oak Ridge National Laboratory, Oak Ridge, Tennessee, USA
Report ORNL/R SIC-49, September 1988

[Vog84] H.G. Vogt

Intercomparison of Monte Carlo Calculations and Measurements of the Neutron and Gamma Ray Streaming in Multibend Ducts.
Proc. of Sixth International Conference on Radiation Shielding, Tokyo, Japan, May 16-20, 1983

[Wes81a] J.T. West, T.J. Hoffman and M.B. Emmet

MORSE-SGC/S for the SCALE System.
Oak Ridge National Laboratory, Oak Ridge, Tennessee, USA
Report NUREG/CR-0200, Volume 2, Section F9, October 1981

[Wes84] J.T. West and M.B. Emmet

MARS: A Multiple Array System using Combinatorial Geometry.
Oak Ridge National Laboratory, Oak Ridge, Tennessee, USA
Report NUREG/CR-0200, Volume 3, Section M9, December 1984

[Wes81b] R.M. Westfall, L.M. Petrie, N.M. Greene and J.L. Lucius

NITAWL-S: SCALE System Module for Performing Resonance Shielding and Working Library Production.
Oak Ridge National Laboratory, Oak Ridge, Tennessee, USA
Report NUREG/CR-0200, Volume 2, Section F2, October 1981

[Yam88] A. Yamaji

Design Method of Compensational Shield for Shield Irregularities of Re-processing Plant.
Proc. of Seventh International Conference on Radiation Shielding, Bournemouth, U.K., September 12-16, 1988

[Zij83] W.L. Zijp, É.M. Zsolnay, H.J. Nolthenius E.J. Szondi G.C.H.M. Verhaag, D.E. Cullen and C. Ertek

Final Report on the REAL-80 Exercise.
Report ECN-128, February 1983

[Zij84] W.L. Zijp, H.J. Nolthenius and G.C.H.M. Verhaag

Cross Section Library DOSCROSS84
Report ECN-160, October 1984

[Zso82] É.M. Zsolnay and E.J. Szondi
Neutron Spectrum Determination by Multiple Foil Activation Method.
Periodica Polytechnica, Vol. 26, Nos 1-2, Budapest, 1982

[Zso91] É.M. Zsolnay
Private Communication, 1991

Appendix A

Calculational Method of XSDRNP-M-S

The one-dimensional transport equation in spherical geometry writes [Gre83, Alc86]:

$$\frac{\mu}{r^2} \frac{\partial(r^2 \phi_g)}{\partial r} + \frac{1}{r} \frac{\partial((1 - \mu^2) \phi_g)}{\partial \mu} + \Sigma_t^g \phi_g(r, \mu) = S_g(r, \mu) \quad (\text{A.1})$$

where μ is the cosine of the angle with respect to the radius r , ϕ_g is the group integrated flux and Σ_t^g is the group averaged total cross section for group g . In the absence of fission, the source S_g consists of a scattering term and a fixed source term:

$$S_g(r, \mu) = 2\pi \sum_{g'=1}^G \int_{4\pi} \Sigma_s^{g' \rightarrow g}(r, \Omega' \rightarrow \Omega) \phi_{g'}(r, \Omega') d\Omega' + S_{f,g}(r, \mu) \quad (\text{A.2})$$

The scattering cross section of the first term on the RHS of Eq. (A.2) can be expanded into a Legendre series, leading to:

$$\begin{aligned} & 2\pi \sum_{g'=1}^G \int_{4\pi} \Sigma_s^{g' \rightarrow g}(r, \Omega' \rightarrow \Omega) \phi_{g'}(r, \Omega') d\Omega' = \\ & = \sum_{g'=1}^G \int_{-1}^1 \sum_{\ell=0}^L \frac{2\ell+1}{2} \Sigma_{s\ell}^{g' \rightarrow g}(r) P_\ell(\mu) P_\ell(\mu') \phi_{g'\ell}(r, \mu') d\mu' = \\ & = \sum_{g'=1}^G \sum_{\ell=0}^L \frac{2\ell+1}{2} \Sigma_{s\ell}^{g' \rightarrow g}(r) P_\ell(\mu) \phi_{g'\ell}(r) \end{aligned} \quad (\text{A.3})$$

where $\Sigma_{s\ell}^{g' \rightarrow g}$ are the Legendre expansion coefficients, and P_ℓ is a Legendre function of order ℓ . Note that this equation also requires the Legendre moments of the flux, $\phi_{g'\ell}$, being calculated. In fact, Eq. (A.3) could also have been derived by expanding the flux in Eq. (A.2) into a Legendre series, of which only one term gives a non-zero contribution due to the orthogonality property of Legendre functions.

An angular quadrature is chosen with M angles μ_m and weights w_m to perform the angular integration. Furthermore, a geometrical quadrature is chosen with I intervals. The angular loss term due to the curvilinear geometry (the second term in Eq. (A.1)) is accounted for by angular redistribution, which serves to change the direction of the particle as it moves from one radial position to another. Angular redistribution is imposed by several restrictions. First, there can be no net gain or loss of particles if the angular redistribution term is integrated over all directions. Secondly, the cosine value of the direction of a particle can only increase up to the value $\mu = 1$. Finally, particles with direction cosine $\mu = 1$ or $\mu = -1$ need not to be angular redistributed.

The discrete ordinates expression in spherical geometry then becomes:

$$\begin{aligned}
 & w_m \mu_m (A_{i+1} \phi_{g,i+1,m} - A_i \phi_{g,i,m}) + \\
 & + \alpha_{i+1/2,m+1/2} \phi_{g,i+1/2,m+1/2} - \alpha_{i+1/2,m-1/2} \phi_{g,i+1/2,m-1/2} + \\
 & + w_m \sum_{l,i+1/2}^g V_i \phi_{g,i+1/2,m} = w_m V_i S_{g,i+1/2,m}
 \end{aligned} \tag{A.4}$$

where i and m are the indices for the spatial and angular meshes, respectively, A and V are the area and the volume of the mesh intervals, respectively, and α is an angular redistribution coefficient. The source term becomes:

$$\begin{aligned}
 & S_{g,i+1/2,m} = S_{f,g,i+1/2,m} + \\
 & + \sum_{g'=1}^G \sum_{\ell=0}^L \frac{2\ell+1}{2} \Sigma_{s\ell}^{g' \rightarrow g} P_\ell(\mu_m) \sum_{m'=1}^M P_\ell(\mu_{m'}) \phi_{g',i+1/2,m'} w_{m'}
 \end{aligned} \tag{A.5}$$

The cell averaged fluxes are related to the cell edge values by a weighted diamond difference model, which ensures positivity of all fluxes.

The solution of the transport equation is obtained by sweeping over the spatial and angular meshes (inner iterations) for each energy group and subsequently sweeping over all energy groups (outer iterations).

Appendix B

Correlated Sampling

Correlated sampling is a collective noun for techniques which make use of correlation between statistical variables. It is especially useful to calculate differential effects or ratios of statistical variables by Monte Carlo codes [Spa69]. Usually the method consists of using the same particle trajectories for both the original and perturbed problem, or starting each particle trajectory by the same random number in both the original and perturbed problem.

If the ratio of two statistical variables is to be calculated, it may be advantageous to calculate both nominator and denominator in the same Monte Carlo run. Because the same particle trajectories are used to calculate both nominator and denominator of the fraction, these two numbers may be positively correlated, which leads to a reduced variance of the requested fraction. Suppose the ratio p is defined as:

$$p = \frac{x}{z} = \frac{x}{x + y} \quad (\text{B.1})$$

where x and y are statistical variables with standard deviations σ_x and σ_y , respectively, then holds for the variance of p approximately:

$$\sigma_p^2 \approx \left(\frac{1}{z}\right)^2 \sigma_x^2 + \left(\frac{x}{z^2}\right)^2 \sigma_z^2 - 2 \frac{x}{z^3} \text{cov}(x, z) \quad (\text{B.2})$$

Because $z = x + y$, the covariance of x and z can be written as $\text{cov}(x, z) = \sigma_x^2 + \text{cov}(x, y)$, and the variance of z as $\sigma_z^2 = \sigma_x^2 + \sigma_y^2 + 2 \text{cov}(x, y)$. For the squared fractional standard deviation of p then holds:

$$\begin{aligned} \left(\frac{\sigma_p}{p}\right)^2 &= \left(\frac{y}{z}\right)^2 \left[\left(\frac{\sigma_x}{x}\right)^2 + \left(\frac{\sigma_y}{y}\right)^2 - 2 \frac{\text{cov}(x, y)}{xy} \right] = \\ &= \left(\frac{y}{z}\right)^2 \left[\left(\frac{\sigma_x}{x}\right)^2 + \left(\frac{\sigma_y}{y}\right)^2 - 2 r_{x,y} \left(\frac{\sigma_x}{x}\right) \left(\frac{\sigma_y}{y}\right) \right] \end{aligned} \quad (\text{B.3})$$

where $r_{x,y}$ is the correlation coefficient between x and y .

If x and y are uncorrelated, this simplifies to:

$$\left(\frac{\sigma_p}{p}\right)^2 = \left(\frac{y}{z}\right)^2 \left[\left(\frac{\sigma_x}{x}\right)^2 + \left(\frac{\sigma_y}{y}\right)^2 \right] < \left(\frac{\sigma_x}{x}\right)^2 + \left(\frac{\sigma_z}{z}\right)^2 \quad (\text{B.4})$$

The term on the RHS of Eq. (B.4) after the $<$ sign, is the squared fractional standard deviation of p if x and z would have been uncorrelated, The $<$ sign is valid if x and y are both positive, which implies $y < z$. From Eq. (B.4), it is seen that the standard deviation is reduced if x and z are positively correlated.

To derive Eq. (B.4), it was assumed that x and y are uncorrelated. Generally, this will not be the case, and it depends on the sign and magnitude of the correlation coefficient how large the squared fractional standard deviation of p will be. For the worst case, x and y are fully anticorrelated ($r_{x,y} = -1$), which leads to:

$$\left(\frac{\sigma_p}{p}\right)^2 = \left(\frac{y}{z}\right)^2 \left(\frac{\sigma_x}{x} + \frac{\sigma_y}{y}\right)^2 \quad (\text{B.5})$$

In Table 7.3, the fractional contribution of the uncollided flux was calculated as:

$$p = \frac{\phi^{unc}}{\phi} = \frac{\phi^{unc}}{\phi^{unc} + \phi^{col}} \quad (\text{B.6})$$

Because both ϕ^{unc} and ϕ^{col} are positive, and the nominator and denominator of fraction p are positively correlated, Eq. (B.4) is valid. Unfortunately, the uncollided and collided fluxes are likely to be correlated. If the uncollided flux in the duct is underestimated because the angular description of the source is too coarse, as is the case in Section 7.2, more neutrons are scattered in the wall of the duct, and the collided flux is expected to be overestimated. Due to this process, the correlation coefficient $r_{x,y}$ is expected to be negative, and Eq. (B.4) gives a lower bound for the fractional standard deviation. Therefore, Eq. (B.5) was used to calculate the fractional standard deviation of this fraction, which gives an upper bound for the error.

In Table 7.4, the fraction of the thermal flux, only due to thermal source neutrons is given. This fraction writes:

$$p = \frac{\phi_{th}^t}{\phi_{th}} = \frac{\phi_{th}^t}{\phi_{th}^t + \phi_{th}^d} \quad (\text{B.7})$$

where ϕ_{th}^t and ϕ_{th}^d are the thermal fluxes due to thermal source neutrons and downscattered neutrons, respectively. In reality, these two fluxes are also likely

to be correlated, but it is again quite difficult to estimate the sign and magnitude of the correlation. As the source spectrum is normalized to unity, an increase of the thermal source implies a decrease of the non-thermal source, thus leading to a negative correlation between ϕ_{th}^t and ϕ_{th}^d . But the correlation due to the transport process from source to detector can be negative or positive, and other effects may lead to a correlation between ϕ_{th}^t and ϕ_{th}^d as well. The sign and magnitude of the correlation is therefore difficult to estimate, and Eq. (B.5) was used to calculate the fractional standard deviation of this fraction as well.

The standard deviation of the fractions given above, calculated in only one Monte Carlo run was usually still too large. More runs were necessary, and the mean value of the fractions had to be calculated. It can be shown that the standard deviation of the mean value of p is minimized, if the inverse variance is used as a weighting factor. Thus:

$$\bar{p} = \frac{1}{n} \sum_{i=1}^n \frac{p_i}{\sigma_i^2} \quad (\text{B.8})$$

and:

$$\sigma_{\bar{p}}^2 = \frac{1}{\sum_{i=1}^n \frac{1}{\sigma_i^2}} \quad (\text{B.9})$$

The values of \bar{p} and $\sigma_{\bar{p}}/\bar{p}$ are the ones given in Tables 7.3 and 7.4.

Summary

To modernize shielding software, the gamma ray point-kernel shielding code MARMER has been developed, which combines several useful options not available in other codes. Furthermore, the geometry package and data libraries have been renewed. The code is validated with an experimental benchmark on a TN12 shipping cask. The results of the code are generally in agreement with the measurements, and the discrepancies found could be accounted for. It turned out that the code is very suitable to these kind of shielding problems, but other options make the code usable for a much larger class of gamma ray shielding problems as well.

Gamma ray buildup factor calculations were performed for iron, with a one-dimensional discrete ordinates code. Large discrepancies with literature occurred, when libraries with too broad energy groups were used. Customized libraries performed better, but the increase of CPU time due to more energy groups and higher Legendre orders, was considerable. It turned out to be very hard to calculate buildup factors accurately up to 40 mean free paths in the shield for source energies above 5 MeV, because of the strongly forwardly peaked flux. The problems arising when performing deep penetration gamma ray calculations are described.

Neutron streaming through bent ducts is often difficult to calculate. An introduction to this problem is given, together with simple methods to calculate the angular distribution of the source at the duct entrance, and at the entrance of the second leg of bent ducts. These methods are applied in the IRIDUCT program, which calculates in a fairly fast and simple way, the fluxes in empty multibent ducts, making only use of total albedo values of the duct wall.

Experiments were performed in cooperation with the reactor physics group of the Institute of Nuclear Technics of the Technical University of Budapest. Concrete blocks containing a straight duct and two-legged ducts with bends of 30, 60 and 90 degrees, were placed in an irradiation tunnel at a distance of about 50 cm from the outer side of the reactor core. The maximum power of the reactor was 100 kW. The neutron spectra at different positions in the ducts were measured by multiple foil activation and thermoluminescence measurements.

Rigorous calculations with two-dimensional discrete ordinates and three-dimensional Monte Carlo calculations are described, and the results are compared with the measurements. The performance of such codes in complex three-dimensional geometries turned out to be good, although large CPU times are required. It was found that reducing three-dimensional geometries to two-dimensional ones can introduce rather large errors. Also the discrete representation of the angular flux distribution may cause errors, if the flux is in reality strongly forwardly peaked, as is often the case in empty ducts. In view of the much lower CPU time used by IRIDUCT, the results of this program are quite satisfactory.

A method to enhance the efficiency of Monte Carlo codes is described. Point values are calculated in a forward Monte Carlo run, and subsequently used to set the biasing parameters of the following runs. The method worked well, but considerable problem dependent programming was necessary, which makes a complete automatic biasing procedure not straightforward.

Samenvatting

Om programmatuur voor afschermingsdoeleinden te modernizeren is de gamma-afschermingscode MARMER ontwikkeld. In deze code zijn verschillende invoeropties gecombineerd, die niet beschikbaar zijn in andere codes. Ook zijn het geometriepakket en de databibliotheken vernieuwd. MARMER is gevalideerd door dosistempo's rondom een TN12-transportvat te berekenen, en deze te vergelijken met de metingen die in de literatuur zijn beschreven. Over het algemeen zijn de resultaten goed en de verschillen die aanwezig waren konden worden verklaard. MARMER bleek erg geschikt voor dit soort problemen, maar de code kan voor vele andere soorten afschermingsberekeningen worden gebruikt.

Gamma-opbouwfactoren zijn berekend voor ijzer met een één-dimensionale discrete ordinaten code. Grote afwijkingen met literatuurwaarden traden op, wanneer databibliotheken met te brede energiegroepen werden gebruikt. Zelf-berekende gammadatabibliotheken met meer energiegroepen en een hogere Legendre orde ontwikkeling, gaven betere resultaten, maar de benodigde reken-tijd nam aanzienlijk toe. De berekening van opbouwfactoren voor afscher-mingsdikten van 40 gemiddeld vrije weglengten en energieën boven 5 MeV, bleek moeilijk door de sterk voorwaarts gerichte gammaflux. De problemen die optreden met gamma-afschermingsberekeningen voor dikke afschermingslagen zijn beschreven.

Een introductie tot stromingsverschijnselen van neutronen door doorvoer-ingen is gegeven, met simpele oplossingen om de hoekverdeling van de bron aan de ingang van de doorvoering en aan het begin van het tweede been van geknikte doorvoeringen te berekenen. Deze methoden zijn toegepast in het IRIDUCT programma, dat op een snelle en eenvoudige manier de neutron-en gammafluxen in lege, geknikte doorvoeringen kan berekenen, met gebruik-making van alleen de totale albedo waarden van de wand van de doorvoering.

Experimenten zijn beschreven, die zijn verricht in samenwerking met de reactorfysicagroep van het Institute of Nuclear Technics van de Technische Universiteit van Boedapest. Betonblokken met een rechte doorvoering en geknikte doorvoeringen met hoeken van 30, 60 en 90 graden, zijn op een afs-tand van 50 cm van de reactorkern geplaatst, in een speciaal daartoe ingerichte bestralingstunnel. Het maximum vermogen van de reactor was 100 kW. De

neutronspectra op diverse posities in de doorvoeringen zijn gemeten met folie-activeringsmetingen en thermoluminescentiemetingen.

Transportberekeningen met twee-dimensionale discrete ordinaten en drie-dimensionale Monte Carlo codes zijn uitgevoerd en de resultaten zijn vergeleken met de metingen. De resultaten zijn goed, maar de benodigde rekestijden waren aanzienlijk. Een gesimplificeerd twee-dimensionaal model van de drie-dimensionale kern en reflector is een belangrijke bron van afwijkingen. De discrete representatie van de hoekverdeling van de neutronflux aan het begin van de bestralingstunnel leidt ook tot afwijkingen, die zich vooral uiten als de flux in werkelijkheid sterk voorwaarts gepiekt is, zoals dikwijls het geval is in doorvoeringen. Gelet op de veel kortere rekestijd voor het IRIDUCT programma, zijn de resultaten van dit programma redelijk goed.

Een methode om Monte Carlo berekeningen te versnellen, is beschreven. Hiertoe is de gemiddelde detectorbijdrage van deeltjes die in een bepaalde zone en energiegroep uit een botsing komen, berekend in een voorwaartse Monte Carlo berekening. Deze gemiddelde detectorbijdragen zijn vervolgens gebruikt om kansdichtheden, die in Monte Carlo codes worden gebruikt om deeltjes door het systeem te volgen, te veranderen zodanig dat de variantie en/of de rekestijd van volgende berekeningen afneemt. De volgende berekeningen kunnen dan efficiënter worden uitgevoerd. De efficiency van dit "importantie iteratie" schema hangt in sterke mate af van de benodigde tijd om dit iteratie schema te programmeren. Problemen afhankelijke zaken maken het moeilijk om dit importantie iteratie schema te automatiseren.

Acknowledgements

This thesis would not have been possible without the help of several people, to whom I would like to express my gratitude.

I would like to thank prof. dr. ir. H. van Dam for the opportunity of performing this study at the reactor physics department of the Interfaculty Reactor Institute, and dr. ir. J.E. Hoogenboom for his daily help and valuable advices and for the management of this PhD research. I am also thankful to the Ministry of Economic Affairs, who enabled me to perform a project on shielding, which constitute the first two years of this PhD work, and to dr. K.G. Bueno de Mesquita and dr. J.B.M. de Haas of NUCON and ECN, respectively, for their help during this shielding project.

I am very thankful to ir. P.F.A. de Leege, for his help with data libraries and computer codes, and for the introduction to reactor physics calculations in general. His solutions to many practical problems in terms of computer code names and schemes connecting these codes, constitute a large part of this work.

I also wish to express my gratitude to dr. É.M. Zsolnay and to mrs. Pekári Éva Sipos, for the cooperation with the neutron spectrum measurements at the Institute of Nuclear Technics of the Technical University of Budapest. The many hours (also during nights and weekends) they spent on counting foil activities contribute for a great deal to this work. Thanks are also due to the operators and dosimetry group of the NTI for their cooperation, and to dr. S. Fehér and his family, who made me understand a little bit the Hungarian way of life.

I would like to thank dr. A.J.J. Bos for his help at the TLD measurements described in this thesis, and all the other members of the reactor physics department for their help and suggestions and for the friendly atmosphere at the IRI.

Last but not least, I would like to thank Helmieke. Her help and her ability to put things in perspective were indispensable to me.

Jan Leen Kloosterman

Curriculum Vitae

De auteur van dit proefschrift is op 21 juni 1964 geboren te Biezelinge (gemeente Kapelle). Hij behaalde het VWO diploma in 1982 aan het Christelijk Lyceum voor Zeeland te Goes. Vervolgens studeerde hij Technische Natuurkunde aan de Technische Universiteit te Delft, waar hij in 1987 afstudeerde in de vakgroep reactorfysica van het Interfacultair Reactor Instituut. Vanaf juni 1987 was hij gedurende twee jaar aan dat instituut verbonden als toegevoegd onderzoeker, en werkzaam op het gebied van stralingsafscherming. Aansluitend is een vervolgonderzoek uitgevoerd op het gebied van stromingsverschijnselen van neutronen in doorvoeringen. Het werk verricht vanaf juni 1987 is beschreven in dit proefschrift. Vanaf 1 mei 1992 is de auteur werkzaam bij het Energieonderzoek Centrum Nederland te Petten.